Chapter 3
Interactions of Ionizing Radiation with Matter and Direct Energy Conversion

Abstract Ionizing radiation is a broad term which refers to the fact that different types of radiation will create ion pairs in matter. Ionizing radiation includes ions (e.g., fission fragments and alpha particles), beta particles, gamma rays, x-rays, and neutrons. Radioisotopes emit ionizing radiation and are viewed as the primary power source for nuclear batteries. This chapter will explore various radioisotope sources and their properties. The transducers which can be used in concert with radioisotope sources will be discussed.

Keywords Radiation interactions · Range · Transducers

3.1 Ionizing Radiation Types and Ranges

Each type of ionizing radiation source has a characteristic range. Consider a material in the solid phase, for example. Swift heavy ions such as fission fragments and alpha particles will deposit their energy within a solid over a distance of micrometers. Electrons deposit their energy over a range of millimeters. Particles which possess high energy and either no rest mass or no net charge, such as gamma rays and neutrons, deposit their energy over a range of meters.

3.1.1 Fission Fragments

The shortest transport scale lengths are for ions, and the most massive ions are the fragments produced by fission. Fission commonly occurs through spontaneous decay of a heavy atom like californium-252, which releases fast neutron energy and fission fragments. The neutron energy and fission yield spectra are shown in Figs. 3.1 and 3.2 respectively. Products of a spontaneous fission event are shown in Eq. (3.1) where ff_l is the light fission fragment, ff_h is the heavy fission fragment, v is the statistical average number of prompt fission neutrons, n_{fast}, released during

Fig. 3.1 Energy spectrum of
neutrons produced by the
spontaneous fission of Cf-252
[1]

$$N \sim e^{-0.88E} \, SINH[2.0E]^{1/2}$$

- TIME OF FLIGHT DATA

- PLATE DATA
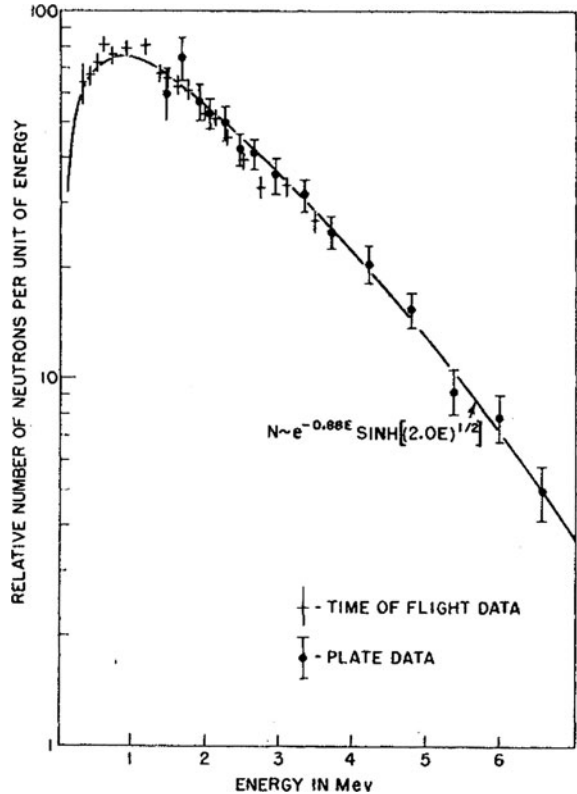
Fig. 3.2 Spontaneous fission
yields of Cf-252 [3]
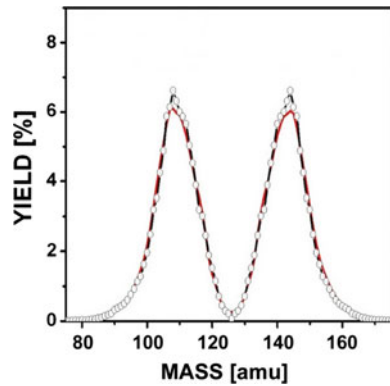
fission and are emitted with a typical fast neutron distribution [1, 2]. Fission can also
be stimulated by neutron capture, whereby a nucleus absorbs an incident neutron,
becomes unstable, and breaks apart. An example of fission initiated through the
interaction of thermal neutrons with a fissile material, such as uranium-235, is shown

in Eq. (3.2); where *n*th is a thermal neutron with energy on the order of 25 MeV. Thermal fission also releases fast neutrons and fission fragments; the neutron energy distribution and bimodal fission yield distribution of U-235 are shown in Figs. 3.3 and 3.4, respectively. The average energy produced by particles released in the

Fig. 3.3 Neutrons energy spectrum produced by the thermal fission of U-235 [4]
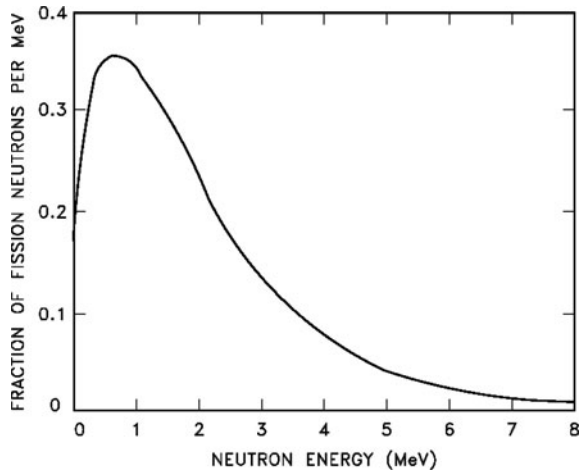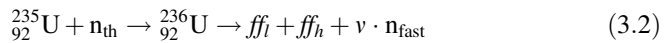

Fig. 3.4 U-235 fission yields for high- and low-energy (thermal) incident neutrons [4]
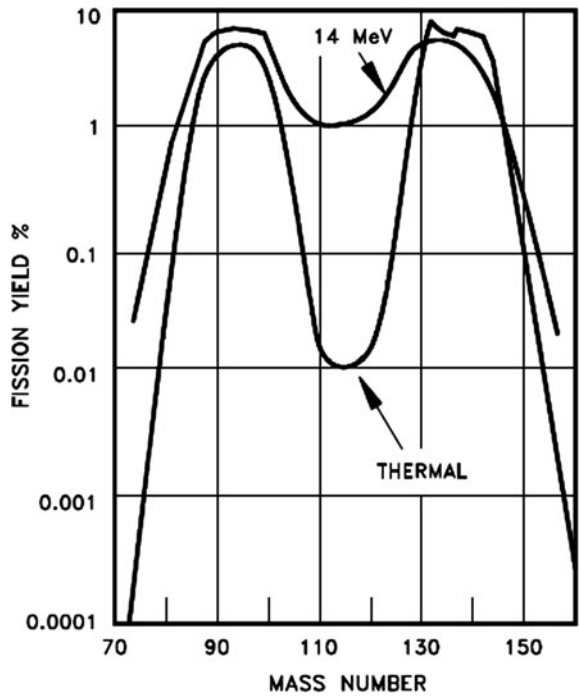
Table 3.1 Statistical distribution of energy released in the fission of U-235 [4]

Radiation	Energy in MeV
Kinetic energy of fission fragments	167
Fission neutrons	5
Prompt gamma rays	5
Delayed gamma rays from fission fragments	6
Capture gamma ray energy	10
Beta particles from fission fragments	7
Neutrinos	10
Total energy	210

fission of U-235, including neutrons, gamma rays, beta particles and neutrinos, is shown in Table 3.1.

$$\begin{array}{}_{98}^{252}\text{Cf} \rightarrow ff_l + ff_h + v \cdot \text{n}_{\text{fast}}\end{array} \tag{3.1}$$

$$\begin{array}{}_{92}^{235}\text{U} + \text{n}_{\text{th}} \rightarrow \begin{array}{}_{92}^{236}\end{array}\text{U} \rightarrow ff_l + ff_h + v \cdot \text{n}_{\text{fast}}\end{array} \tag{3.2}$$
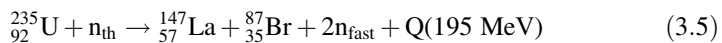
Kinetic energy for each fission fragments depends on the mass of the fragments as shown in Eqs. (3.3) and (3.4), where KE_{ff_l} is the kinetic energy of the light fission fragment, KE_{ff_h} is the kinetic energy of the heavy fission fragment, KE_{ff} is the total kinetic energy of both fission fragments, m_h is the mass of the heavy fission fragment and m_l is the mass of the light fission fragment. The linear energy transfer of fission fragments and other swift heavy ions can be calculated using the Bethe-Bloch formula.

$$KE_{ff_l} = \frac{m_h}{m_h + m_l} KE_{ff} \tag{3.3}$$

$$KE_{ff_h} = \frac{m_l}{m_h + m_l} KE_{ff} \tag{3.4}$$

For example, consider the specific fission reaction of U-235 shown in Eq. (3.5) that produces La-147 and Br-87. The kinetic energies of the fission fragments are calculated in Eqs. (3.6) and (3.7), respectively, and the energy from the fission reaction products are shown in Table 3.2. As stated earlier, the ranges of fission fragments in matter are very short due to their mass and charge. Ranges for the two fission fragments used in this example are pictured in Figs. 3.5 and 3.6. The bromine-87 atom has a range of 6.29 μm in uranium metal. The spatial energy distributions of both fission fragments within the material are shown in Figs. 3.7 and 3.8, respectively.

$$\begin{array}{}_{92}^{235}\text{U} + \text{n}_{\text{th}} \rightarrow \begin{array}{}_{57}^{147}\end{array}\text{La} + \begin{array}{}_{35}^{87}\end{array}\text{Br} + 2\text{n}_{\text{fast}} + Q(195 \text{ MeV})\end{array} \tag{3.5}$$

Table 3.2 Distribution of energy released during the fission of U-235 which yields the specific fission fragments La-147 and Br-87 [5]

Radiation	Energy in MeV
Kinetic energy of fission fragments	162
Fission neutrons	6
Prompt gamma rays	6
Delayed gamma rays from fission fragments	5
Beta particles from fission fragments	5
Neutrinos	11
Total energy	195

Table 3.1 is an overall statistical yield for fission while this table is specific to a single fission reaction
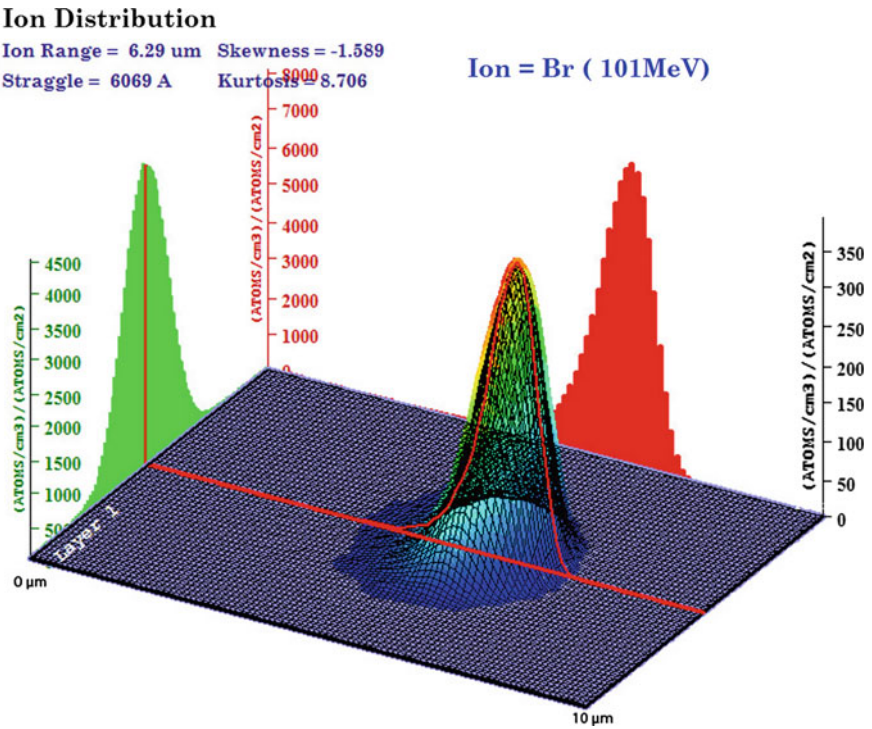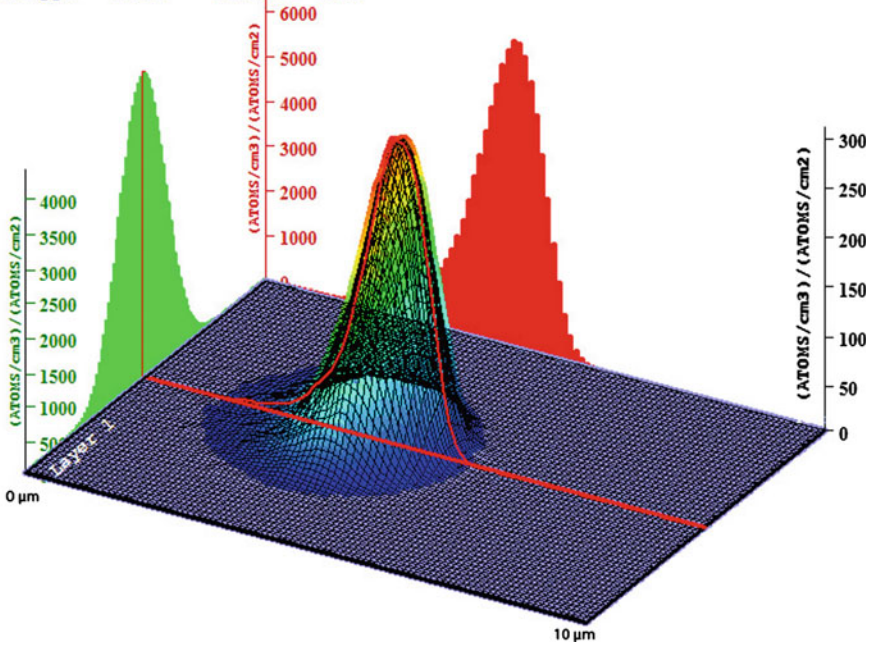

Fig. 3.5 SRIM2011 model showing ion distribution in uranium of 101 MeV bromine-87 ions slowing down [6]. The plot ordinate has units $(Atoms/cm^3)/(Atoms/cm^2)$. By multiplying with ion dose (units of $Atoms/cm^2$ of bromine-87), the ordinate converts to a density distribution of Br-87 with units of $(Atoms/cm^3)$. The ion source originates from the left side so the two dimensional plane indicates the depth and width of the ion distribution

Ion Distribution

Ion Range = 4.22 um Skewness = -1.139
**Straggle = 6843 A   Kurtosis = 5.443**

Ion = La (60 MeV)

Fig. 3.6 SRIM2011 model showing final ion distribution of 60 MeV lanthanum-147 ions transported through uranium metal [6]. The plot ordinate has units (Atoms/cm^3)/(Atoms/cm^2). By multiplying with ion dose (units of Atoms/cm^2 of La-147), the ordinate converts to a density distribution of La-147 with units of (Atoms/cm^3). The ion source originates from the left side so the two dimensional plane indicates the depth and width of the ion distribution

$$KE_{\text{La}-147} = \frac{87}{147 + 87} \, 162 = 60.23 \, \text{MeV} \tag{3.6}$$

$$KE_{\text{Br}-87} = \frac{147}{147 + 87} \, 162 = 101.77 \, \text{MeV} \tag{3.7}$$

The fission reaction shown in Eq. (3.8) is the consequence of the interaction of a fast neutron (energy greater than 1 MeV) and U-238. Fast fission of U-238, for example, provides a large part of the explosive yield in a thermonuclear weapon. The energy distribution of the fast fission products is similar to that of products in thermal fission.

Fig. 3.7 SRIM2011 model showing target ionization in uranium metal by 101 MeV bromine-87 ions [6]. The *left* ordinate is energy loss (eV/Å), the *right* ordinate is the number of recoil atoms
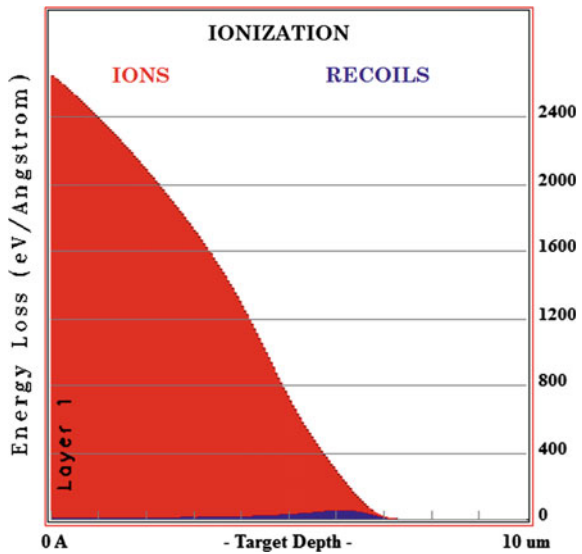
Fig. 3.8 SRIM2011 model of target ionization in uranium metal by 60 MeV lanthanum-147 ion [6]. The *left* ordinate is energy loss (eV/Å), the *right* ordinate is the number of recoil atoms

$$^{238}_{92}U + n_{fast} \rightarrow {}^{239}_{92}U \rightarrow ff_h + ff_l + v \cdot n_{fast} \tag{3.8}$$
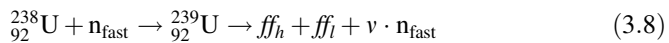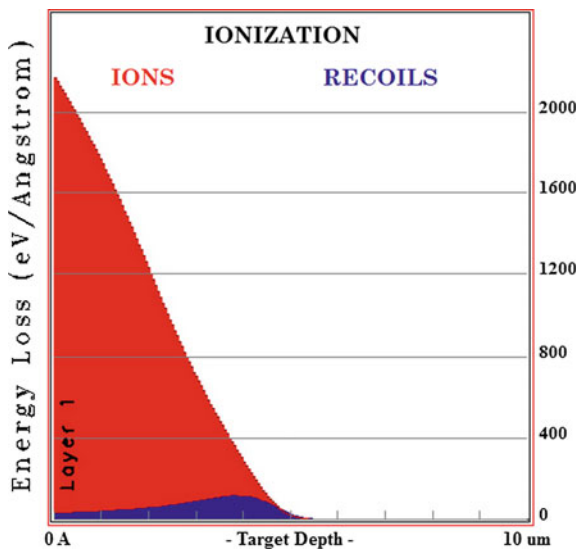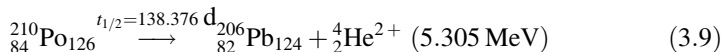
3.1.2 Alpha Particles

Alpha-emitting radioisotopes which are appropriate for use in a nuclear battery are described in Table 3.3. Polonium-210 is used an example here (Eq. 3.9).

Table 3.3 Potential α sources for nuclear batteries

Nuclide	Decay energy (MeV)	Half life (Years)	Other emissions (MeV, %)		Production reactions
Gd-148	3.182	74.6	N/A		Sm-147(α,3n) Eu-151(p,4n)
Po-208	5.216	2.8979	β^+	0.3783 (0.00223 %)	Bi-209(d, 3n) Bi-209(p,2n)
Po-210	5.305	0.379	γ	0.803 (0.0011 %)	Natural source
Th-228	5.52	1.9131	α	5.340 (27.2 %) 5.423 (72.2 %)	Natural source
			γ	0.216 (0.25 %)	
U-232	5.414	68.9	α	5.263 (31.55 %) 5.32 (68.15 %)	Pa-232(β) Th-232(α, 4n)
			γ	0.1–0.3 (low %)	
Pu-236	5.867	2.857	α	5.721 (30.56 %) 5.768 (69.26 %)	Np-236(β) U-235(α, 3n)
Pu-238	5.593	87.74	α	5.456 (28.98 %) 5.499 (70.91 %)	Np-238(β) Np-237(n, γ)
Am-241	5.638	432.2	α	5.442 (13 %) 5.485 (84.5 %)	Pu-241(β)
			γ	0.05954 (35.9 %)	
Cm-243	6.168	29.1	α	5.742 (11.5 %) 5.785 (72.9 %) 5.992 (5.7 %) 6.058 (4.7 %)	Multiple-n capture U-238, Pu-239
			γ	0.2–0.3 (20 %)	
Cm-244	5.902	18.1	α	5.762 (23.6 %) 5.805 (76.4 %)	Multiple-n capture U-238, Pu-239, Am-243
			γ	Low percentage	
Bk-248	5.793	9			Cm-246(α,pn)
Cf-250	6.128	13.07	α	6.0304 (84.6 %) 5.989 (15.1 %)	Multiple-n capture U-238, Pu-239, Cm-244
			γ	0.04285 (0.014 %)	
Cf-252	6.217	2.645	SF	FF (3.092 %)	Multiple n capture U-238, Pu-239, Cm-244
			α	6.0758 (15.7 %) 6.118 (84.2 %)	
			γ	0.043–0.155 (0.015 %)	
Es-252	6.739	1.292	α	6.5762 (13.6 %) 6.632 (80.2 %)	Bk-249(α,n) Cf-252(d,2n)
			γ	0.043–0.924 (25 %)	

The criteria used in identifying these isotopes is based on a half-life between 0.379 and 100 years. Other emissions are shown such as gamma emission (for which additional shielding would be needed) [7]

$$\ce{^{210}_{84}Po_{126}} \xrightarrow{t_{1/2}=138.376\,\text{d}} \ce{^{206}_{82}Pb_{124}} + \ce{^{4}_{2}He^{2+}} \quad (5.305\,\text{MeV}) \tag{3.9}$$

Alpha particles are swift heavy ions whose interactions with matter are governed by the Bethe-Bloch stopping power equation. The range of an alpha particle will be greater than the range of a fission fragment in uranium metal due to its lower charge and mass. This means that the alpha particles shown in Fig. 3.9 will travel a distance of 9.32 μm, as opposed to 4.22 μm for heavy fission fragments and 6.29 μm for light fission fragments. The ionization produced by an alpha particle along its path in a solid will follow a classical Bragg curve with a Bragg peak (see Fig. 3.10), whereas a fission fragment has no Bragg peak (see Figs. 3.7 and 3.8), due to the highly changing linear energy transfer of fission fragments as it picks up electrons during the slowing down process. Further, the range of any charged particle is a function of the electron density of the stopping material, such that less dense materials provide a lower stopping power than higher density materials. For
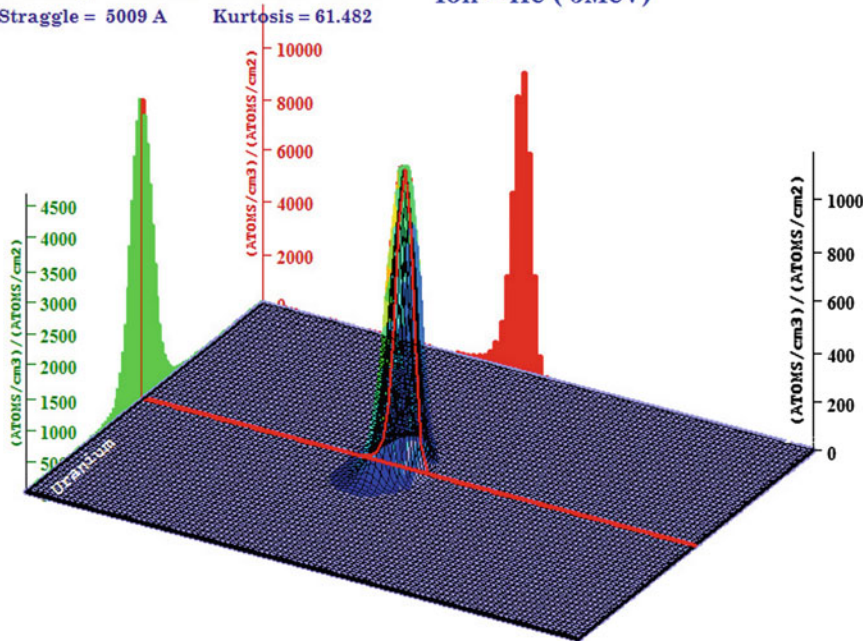
Fig. 3.9 SRIM2011 model showing final ion distribution of 5.3 MeV alpha particles in uranium metal [6]. The plot ordinate has units (Atoms/cm^3)/(Atoms/cm^2). By multiplying with ion dose (units of Atoms/cm^2 of He-4), the ordinate converts to a density distribution of He-4 with units of (Atoms/cm^3). The ion source originates from the left side so the two dimensional plane indicates the depth and width of the ion distribution

Fig. 3.10 SRIM2011 model
showing target ionization
produced in uranium metal by
5.3 MeV alpha particles [6].
The *left* ordinate is energy
loss (eV/Å), the *right* ordinate
is the number of recoil atoms
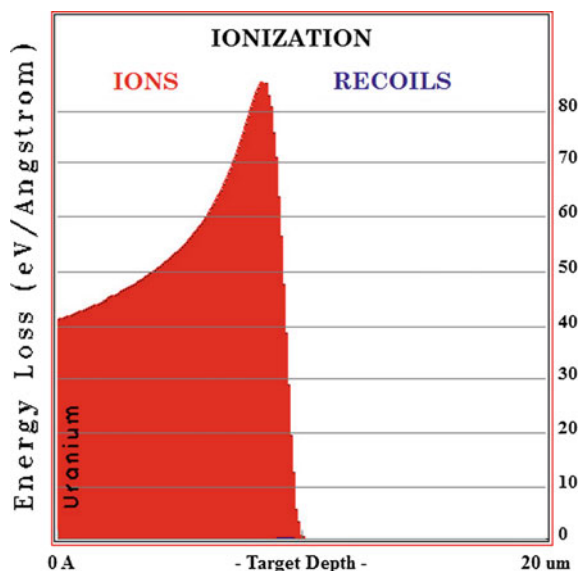
example, the range of 5 MeV alpha particles in air is 40.6 mm (as compared to
9.32 μm in uranium metal). Therefore, it is often instructive to talk about ranges in
terms of areal density, which is the linear range divided by the density of the
material. The areal density is independent of density changes of the absorbing
materials and is similar for similar-Z materials (see the next section for more
discussion on this concept).

3.1.3 Beta Particles and Positrons

An isotope which produces an electron and antineutrino is a β^- emitter, while an
isotope which produces a positron and neutrino is a β^+ emitter. Energetic electrons
transfer energy to the electrons of the target material via Coulomb scattering and
Bremsstrahlung emission as calculated by the modified Bethe formula. Beta-
emitting radioisotopes which have suitable half-lives are shown in Table 3.4.

If an isotope instead emits a positron, the β^+ will encounter some electron in
orbit around an atom. The two will then mutually annihilate to produce two
energetic gamma rays. These gamma rays then interact with matter, using mech-
anisms which are very different from those of electrons or other charged particles.

Compared to high velocity heavy ions, the path of an electron in matter is
complicated. Because the incident electron has a mass equal to that of the electrons
in the target, the electron undergoes significant scattering and follows the random
walk-like path shown in Figs. 3.11 and 3.12.

**Table 3.4** Potential β^- sources for nuclear batteries

Nuclide	Decay energy (MeV)	Half life (Years)	β_{max} (MeV)	Other emissions (Units in MeV)		Production method
H-3	0.019	12.33	0.019	N/A		Li-6(n, α)
Ar-39	0.565	269	0.565	N/A		Ar-38(n, γ) KCl(n, γ)
Ar-42	0.6	32.9	0.6	N/A		Ar-40(n, γ) Ar-41(n, γ)
Co-60	2.824	5.2713	0.318	γ	1.17 (99 %) 1.33 (0.12 %)	Co-59(n, γ)
Kr-85	0.67	10.755	0.67 (99.6 %) 0.15 (0.4 %)	γ	0.514 (0.4 %)	Fission product
Sr-90	0.546	28.77	0.546	β_{max}: 2.281 (Y-90, daughter)		Fission product
Ru-106	0.039	1.0234	0.039	N/A		Fission product
Cd-113m	0.58	14.1	0.58	N/A		Cd-112(n, γ) Cd-113(n, n)
Sb-125	0.767	2.73	0.7667	γ	0.5 (5–20 %)	Sn-124(n, γ)
Cs-134	2.058	2.061	0.662 (71 %) 0.089 (28 %)	γ	0.6–0.8 (97 %)	Cs-133(n, γ)
Cs-137	1.175	30.1	1.176 (6.5 %) 0.514 (93.5)	γ	0.6617 (93.5 %)	Fission Product
Pm-146	1.542	5.52	0.795	γ	0.747 (33 %)	Nd-146(p,n) Nd-148(p,3n)
Pm-147	0.225	2.624	0.225	N/A		Nd-146(n, γ)
Sm-151	0.076	90	0.076	N/A		Fission product
Eu-152	1.822	13.54	1.818	γ	0.1–0.3	Eu-151(n, γ)
Eu-154	1.969	8.592	1.845 (10 %) 0.571 (36.3 %) 0.249 (28.59 %)	γ	0.123 (38 %), 0.248 (7 %), 0.593 (6 %), 0.724 (21 %), 0.759 (5 %), 0.876 (12 %), 1.0 (31 %), 1.278 (37 %)	Eu-153(n, γ)
Eu-155	0.253	4.67	0.147 (47.5 %) 0.166 (25 %) 0.192 (8 %) 0.253 (17.6 %)	γ	0.086 (30 %) 0.105 (21 %)	Sm-154(n, γ)
Tm-171	0.096	1.92	0.0964 (98 %) 0.0297 (2 %)	γ	0.0667 (0.14 %)	Er-170(n, γ)
Os-194	0.097	6	0.0143 (0.12 %) 0.0535 (76 %) 0.0966 (24 %)	γ	0.01–0.08	Os-192(n, γ) Os-193(n, γ)
Tl-204	0.763	3.78	0.763	N/A		Tl-203(n, γ)

Table 3.4 (continued)

Nuclide	Decay energy (MeV)	Half life (Years)	β_{max} (MeV)	Other emissions (Units in MeV)		Production method
Pb-210	0.063	22.29	0.0169 (84 %) 0.0635 (16 %)	γ	0.046 (4 %)	Natural source
Ra-228	0.046	5.75	0.0128 (30 %) 0.0257 (20 %) 0.0392 (40 %) 0.0396 (10 %)	γ	low E (low %)	Natural source
Ac-227	0.044	21.773	0.02 (10 %) 0.0355 (35 %) 0.0448 (54 %)	α	4.953 (47.7 %) 4.940 (39.6 %)	Ra-226(n, γ)
				γ	0.1 to 0.24 γ	
Pu-241	0.021	14.35	0.02082	α	4.853 (12.2 %) 4.896 (83.2 %)	Multiple-n capture U-238, Pu-239

The criteria used in identifying these isotopes is based on a half-life between 1 and 269 years. Other emissions are shown such as gamma emission (for which additional shielding would be needed) [7]
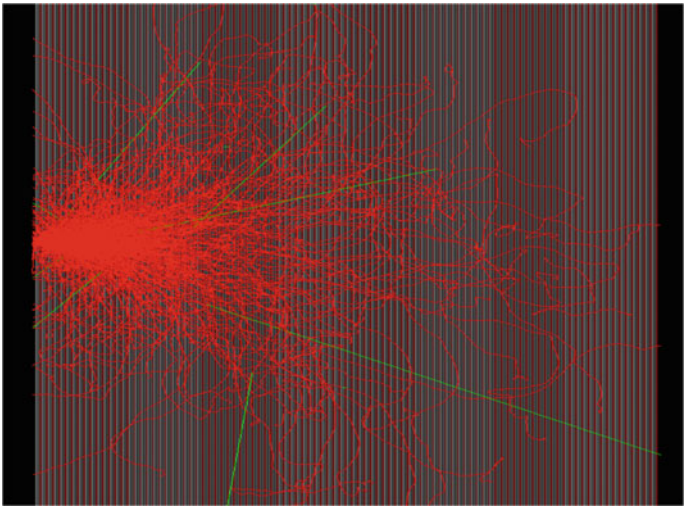
Fig. 3.11 GEANT4 simulation of Sr-90 Beta Decay into SiC of Slab, showing beta particle tracks (random walk path) and bremsstrahlung photons (*straight lines*) [8]

3.1.4 Shielding Considerations

It should also be noted that most alpha and beta emitters considered in nuclear battery technology do not emit significant levels of gamma rays due to potential shielding concerns. For instance, if Co-60 is utilized in a beta-based nuclear battery,
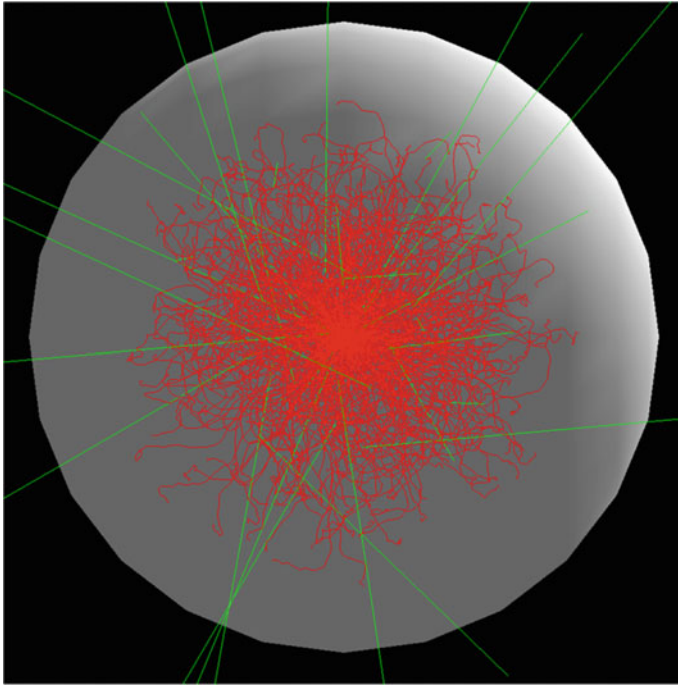
Fig. 3.12 GEANT4 simulation of Sr-90 Beta Decay into SiC of Spherical Model, showing beta particle tracks (random walk path) and bremsstrahlung photons (*straight lines*) [8]

then for 1 mW of power, assuming a 100 % conversion efficiency and complete escape of the high energy gamma rays, would require 1.76 Ci. The associated high energy gamma ray radiation (99 % of the decays will emit 1.17 MeV gamma rays) from this large activity limits its suitability in many situations where radiation effects to surrounding materials (e.g. electronics) and personnel is of importance. Unshielded, the dose-rate at 20 cm from the source is 57.1 Rem/h. If a 20 cm lead shield surrounds the device, the dose rate drops to 0.000569 Rem/h at the surface of the lead shield. This is a particularly bad problem for microscale nuclear batteries, where the shielding required to reduce the gamma-ray flux to acceptable levels oftentimes severely reduces the overall energy density (W_e/kg) of the battery, which also increases the battery footprint as a consequence.

An important point to make is that if the isotope has gamma emissions along with charged particle emissions, there will be a source of penetrating radiation to contend with. Depending on the gamma ray energy and probability of emission, the dose rates can be significant. For example, krypton-85 emits a 514 keV gamma ray 0.4 % of the time [9–11]. Even though the 0.4 % seems small, it can add up to a significant dose. A good example is based on an indirect nuclear battery developed by one of the authors. The device was simple in that the krypton-85 gas operated as both the source and transducer. The device drew commercial interest and two large

companies partnered with the author to develop the device. Beta particles emitted from the isotope caused ionization and excitation of the krypton gas. The excited atoms of krypton quickly form the krypton excimer molecule which then decays to an unbound ground state. The excimer emission is narrow (with a peak at 149 nm with a Full Width at Half Maximum of 10 nm). The excimer fluorescence is then captured by the photovoltaic cells on the walls of the pressure vessel. The theoretical efficiency of this method is over 20 %. The device drew commercial interest because the simplest configuration used a spherical pressure vessel filled with Kr-85 gas. The author and his collaborators designed a device for a space based mission that required 1,000 W of power. The device design concept required an activity of 1,000,000 Curies of krypton gas. The atomic density of krypton in the sphere is,

$$A(0) = \lambda N(0) \tag{3.10}$$

where $k = 0.693/t_{1/2} = 0.693/(10.755 \text{ year} \times 365 \text{ day/year} \times 24 \text{ h/day} \times 3600 \text{ s/h}) = 2.043 \times 10^{-9} \text{ s}^{-1}$.

$$N(0) = \frac{10^6 \text{Ci} \times 3.7 \times 10^{10} \frac{\text{decays}}{\text{s–Ci}}}{2.043 \times 10^{-9} \text{s}^{-1}} = 1.811 \times 10^{25} \text{ atoms} \tag{3.11}$$

There are 2.68×10^{19} atoms (or molecules) cm^{-3} in one atmosphere of gas at Standard Temperature and Pressure (STP) and this number is used in the calculation to find the pressure of 1,000,000 Ci of Kr-85 confined in the sphere. The calculation begins by assuming that the gas pressure in the sphere is low enough to be governed by the idea gas law. The number of atoms (or molecules) in the sphere at a pressure of one atmosphere (N_{atm}) is found by multiplying the sphere volume by the constant (*Volume$_{sphere}$* $\times 2.68 \times 10^{19}$). The pressure of Kr-85 in the sphere can be estimated from the relationship $P_{Kr85} = N(0)/N_{atm}$. This calculation shows that the pressure of 1,000,000 Ci of Kr-85 in the 1000 cm^3 sphere is 676 atmospheres. From an engineering point of view, neither the size of the sphere nor the gas pressure are significant challenges.

The sphere (radius of 6.2 cm) is small enough to be approximated as a point source in a shielding calculation. Using Radpro Calculator [12] to estimate the dose-rate at one meter from the bare sphere, the dose was found to be about 12.27 Rem/h. This dose-rate was determined to be unacceptable by the industrial partner due to radiation sensitive electronics in the package that was going to be deployed along with the power supply. In order to reduce the dose rate to an acceptable level at 1 m, the device needed a shield. Several shield thicknesses were examined and an 8 cm thick lead shield reduced the dose-rate to a workable level of 24 µRem/h. The mass of the 8 cm thick lead shield around the sphere is about 124.6 kg. This indicates that the device would have a mass to power ratio of approximately 0.1246 kg/W which is extremely good compared to mass to power ratio of an RTG ($\sim$5 kg/W).

3.1.5 Rules of Thumb and Their Limitations

The range R of electrons can be estimated using rules of thumb. For example, Eqs. (3.12) and (3.13) can be used to estimate the range of electrons in air. On the whole, rules of thumb such as these are useful for radiation protection considerations but, as discussed below, the usefulness of any rule of thumb quickly breaks down when applied to nuclear battery systems.

$$R_{air}(\text{ft}) \approx 12 \, \text{ft/MeV} \tag{3.12}$$

$$R\left(\text{kg/m}^2\right) = R(\text{m}) \cdot \rho\left(\text{kg/m}^3\right) \tag{3.13}$$

An ion pair which is produced from the interaction of beta particles with matter includes an electron which is kicked out of orbit during the Coulomb interaction; this electron is referred to as a secondary electron. Secondary electrons typically have kinetic energies in the keV range [13]. The secondary electrons create tertiary electrons through ionization and the tertiary electrons can interact to create quaternary, quinary, or higher-order electrons. Because of their equal mass and charge, electrons can transfer their full energy to a target electron through Coulomb interactions. Nonetheless, the electron energy distribution in an electron beam excited plasma [14] is very similar to the spectra created by light ion bombardment (Fig. 3.13).

For example, the maximum energy of the beta particle produced by the decay of phosphorus-32 (^{32}P) is 1.71 MeV. According to Eq. (3.12) the range of the beta particle in air is $1.71 \times 12 = 20.5$ ft ≈ 21 ft. For health physics professionals, this number would be used as an estimate for a safe distance from the source.

There are also similar conservative calculations used by professionals to estimate shielding thicknesses. The concept of areal density is the basis of one such method. It can also be used to conservatively estimate the range of a beta particle in a target material. The areal density is the density of a target material per square centimeter. It is related to the electron density of a given material which is dependent upon the atomic density and atomic number of that material. Since beta particles interact with the electrons which make up the atom, it also can be used to estimate the amount of energy lost by the beta particle as a function of distance (μm^{-1}). Materials with higher electron density have more electrons for the beta particle to interact with and thus will stop the electron in a shorter distance. The areal density is calculated for a specific material using Eq. (3.13), where ρ is the mass density of the material in g/cm^3. In many texts, the areal density is also referred to as 'the range' and given the symbol R. The reader must sort out how the term 'range' is used in each reference. There are rules of thumb for areal density which are shown in Eqs. (3.14–3.18), where E_{max} is the maximum beta energy in MeV, and areal density is given in g/cm^2 (and uses the symbol R).

Fig. 3.13 Nascent and asymptotic electron energy distributions for 1-MeV alpha particle bombardment of helium [13]

$$E_{max} \approx 2 \cdot R(g/cm^2) \quad \text{for } 1 \le E_{max} \le 4\,\text{MeV} \tag{3.14}$$
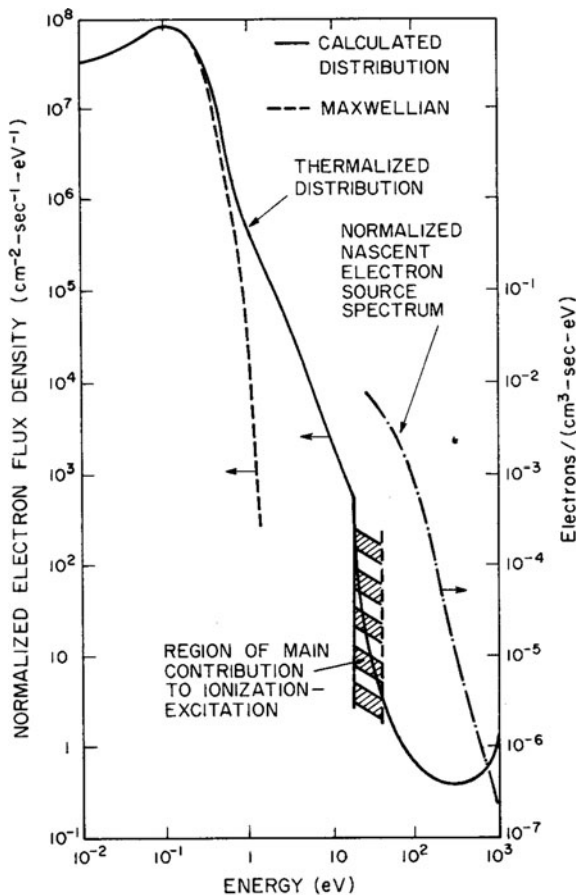
$$E_{max} \approx 1.92 \cdot R^{0.725} \quad \text{for } R \le 0.3\,\text{g/cm}^2 \tag{3.15}$$

$$R(g/cm^2) \approx 0.407 \cdot (E_{max})^{1.38} \quad \text{for } E_{max} \le 0.8\,\text{MeV} \tag{3.16}$$

$$E_{max} \approx 1.85 \cdot R + 0.245 \quad \text{for } R \ge 0.3\,g/cm2 \tag{3.17}$$

$$R(g/cm^2) \approx 0.542 \cdot E_{max} - 0.133 \quad \text{for } E_{max} \ge 0.8\,\text{MeV} \tag{3.18}$$

Models which calculate energy deposition using rules of thumb to find areal density, and therefore particle ranges, will introduce significant errors if used in nuclear battery calculations. The rules of thumb presented above overestimate particle range in order to ensure adequate radiation protection. For example, consider the beta emissions of
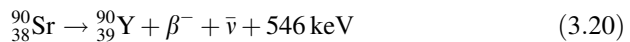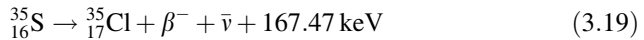
sulfur-35 $\left(^{35}_{16}S\right)$, strontium-90 $\left(^{90}_{38}Sr\right)$, and yttrium-90 $\left(^{90}_{39}Y\right)$. The maximum energy of the beta particle emitted by ^{35}S is 0.167 MeV, which results in a required areal density of $0.407(0.167)^{1.38} \approx 0.034$ (g/cm^2) from Eq. (3.16). For a silicon carbide target with density $\rho = 3.210$ g/cm^3, the estimated range would be $R(cm) \approx R$ (g/cm^2)/$\rho \approx 0.034/3.210 \approx 0.0106$ cm. The maximum energy of a beta particle emitted by ^{90}Sr is 0.546 MeV, which has an estimated areal density of 0.407 $(0.546)^{1.38} \approx 0.177$ (g/cm^2), and the estimated range is $R(cm) \approx R(g/cm^2)/\rho$ 0.177/3.210 ≈ 0.0551 cm. The 2.28 MeV maximum energy of the beta particle emitted by ^{90}Y is considerably higher than the two previous examples. Yttrium-90 has an areal density of $2.28/2 \approx 1.14$ (g/cm^2) to stop the particles, which equates to a range in silicon carbide of $R(cm) \approx R(g/cm^2)/\rho \approx 1.14/3.21 \approx 0.355$ cm.

When two rules of thumb cover the same energy space, the significant errors between them are obvious. For example, Eq. (3.18) covers beta energies greater than 0.8 MeV and Eq. (3.14) covers beta energies between 1 and 4 MeV. If Eq. (3.18) is used to estimate the range for a Sr-90 beta, it yields $0.546546 \times 2.280 - 0.133 \approx 1.103$ (g/cm^2) and a consequent range in cm of approximately equal to R (m) $\approx R$ (g/cm^2)/$\rho \approx 1.103/3.210 \approx 0.344$ cm. The difference between the two rules of thumb (Eqs. 3.14 and 3.18) is about 11 μm, an order of magnitude larger than the transducer scale length of some microscale nuclear battery designs. **Rules of thumb should never be used to design a nuclear battery**.

3.1.6 The Limitations of Average Beta Energy

In addition to the rules of thumb discussed above, there are other simplifications that may misrepresent energy deposition and, therefore, device efficiency. One common, but incorrect, assumption is that all beta particles are emitted with an energy of 1/3 β_{max} [15]. This simplifies the calculation of energy deposition versus depth curve for the device, but at the cost of verisimilitude. The ionization profile produced by a true spectrum of beta particles is significantly different from the results of either the simple rules of thumb described above or the 1/3 β_{max} assumption would indicate. A second fatal simplification arises when it is assumed that the ionizing particles are not emitted isotropically. The lack of accurate transport models creates shifts in the energy deposition profile within the energy transducer, so a higher fraction of the incident energy is deposited deeper within the device, which is not the case [16]. Realistic modeling of these sources is essential to accurately represent energy deposition within the nuclear battery. Three relevant beta-decay reactions with low, medium, and high-energy are shown in Eqs. (3.19–3.21).

$$^{35}_{16}S \rightarrow ^{35}_{17}Cl + \beta^- + \bar{\nu} + 167.47\,\text{keV} \tag{3.19}$$

$$^{90}_{38}Sr \rightarrow ^{90}_{39}Y + \beta^- + \bar{\nu} + 546\,\text{keV} \tag{3.20}$$

Table 3.5 Characteristics of common beta-emitting radioisotopes

| Isotope	Half-life	Max energy	Average energy		% Difference	Daughter isotope
			1/3 βmax rule (keV)	Spectrum (keV)		
S-35	87.51 days	167.47 keV	55.8	53.1	+5	Cl-35
Sr-90	28.8 years	546 keV	182	167	+9	Y-90
Y-90	2.67 days	2.28 MeV	760	945	−20	Zr-90

The average energy is calculated using the 1/3 β_{max} rule and using a full spectrum analysis. The differences in the average energy are substantial for high energy beta sources [7]

$$^{90}_{39}\text{Y} \rightarrow {}^{90}_{40}\text{Zr} + \beta^- + \bar{v} + 2.28\,\text{MeV} \tag{3.21}$$

Table 3.5 shows pertinent data for the three beta emitters, including half-life, the average beta energy according to the commonly-used rule of thumb (1/3 β_{max}), and the average beta energy calculated using the beta spectrum. As can be seen in Fig. 3.14, the sulfur-35 beta spectrum intensity continuously increases as energy decreases, the beta spectrum intensity of the medium-energy strontium-90 emitter tends to flatten out at low energies, and the high energy yttrium-90 beta spectrum intensity has a distinct maxima and then drops as energy decreases. As can be seen in Table 3.5, the differences between the average energy calculated by the 1/3 β_{max} rule and the average energy calculated directly from the spectrum differs significantly as the maximum energy of the beta particle increases. If the average beta energy is calculated using the 1/3 β_{max} rule, the error inherent in using the 1/3 β_{max} rule is propagated through the rest of the system calculations. These incorrect average energies will then be used to calculate incorrect estimates of particle range and stopping power. The 1/3 β_{max} rule should not be used for design calculations and modeling of nuclear batteries.

Accurate range calculations are essential when designing a nuclear battery in order to match the active region of the transducer (L_{trans}) in the optimum position to harvest the energy from the beta particle (λ_{RadTr}). To calculate the range of a beta particle in matter, the full beta energy spectrum should be used in the model (Fig. 3.14). Calculations which use the complete beta spectrum lead to the best


Fig. 3.14 Beta emission energy spectra for S-35 (*solid*), Sr-90 (*dashed*), and Y-90 (*inset*) [8]
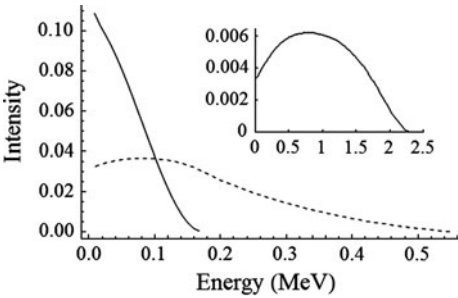
possible estimation of energy deposition profiles. This is clearly shown in the following example. The actual range of beta particles from S-35, Sr-90 and Y-90 decay have been calculated for a beam of beta particles hitting a slab and for a point source in the center of a sphere [8]. These results are significantly different from results that use the average beta energy calculated from the beta spectrum. This further reinforces the premise that unacceptable inaccuracies come from the use of any rules of thumb (Eqs. 3.14–3.18) when designing a nuclear battery. Results from the rules of thumb are several orders of magnitude larger than calculations based on the average beta energy (using the average based on the beta spectrum) or the full beta spectrum. It is interesting that there is about a factor of 4 difference between the range calculated from average beta energy and the range calculated with the full beta spectrum, where the range for the full beta spectrum is greater.

Figures 3.15 and 3.16 represent the energy deposition as a function of distance for a calculation based on the average beta energy and a calculation based on the full beta spectrum, respectively. In the slab geometry, the beta particles were simulated as monodirectional, normal to the stopping material, whereas the point source in the sphere was modeled as isotropic. The results are notably different and again reinforce why designs based on average beta energy have significant errors. Looking at Fig. 3.14, the beta spectrum from each of the isotopes that are represented in this discussion, it is apparent that there is a significant distribution of low energy beta particles which are emitted. By definition, the average beta energy is at the point where the number of beta particles greater than the average energy equal to the number of beta particles less than the average energy. For S-35, the low energy beta population continually increases as the energy approaches zero. For Sr-90, there is a slight peak at 0.08 MeV, but generally the population is flat at lower energies. For Y-90, there is a well-defined maximum in the spectrum at 0.8 MeV. The differences between Figs. 3.15 and 3.16 are not so surprising when the low energy betas in a full spectrum are taken into account.

In the calculations based on average beta energy shown in Fig. 3.15, there are distinct peaks for both the slab and spherical geometries for S-35, Sr-90 and Y-90. For S-35, the peaks occur at 6 μm for the slab geometry and at 10 μm for the spherical geometry. For Sr-90, the peaks occur at 35 μm for the slab geometry and at 65 μm for the spherical geometry. For Y-90, the peaks occur at 400 μm for the slab geometry and at 600 μm for the spherical geometry. In contrast, Fig. 3.16 shows that low energy betas from the spectrum dominate where the energy is deposited. Low energy betas will have a shorter range in the material than high energy beta particles. So, the energy deposited per unit depth into the stopping material for both S-35 and Sr-90 is highest near the surface of the stopping material and decays exponentially with depth. For the high energy Y-90 beta particles there is a distance where energy deposition peaks. For the slab case it peaks at 150 μm and for the spherical case it peaks at about 300 μm. Another interesting observation is that the maximum amount of energy that is deposited is substantially different (about a factor of two lower) for the full spectrum calculation as opposed to the average energy calculation.
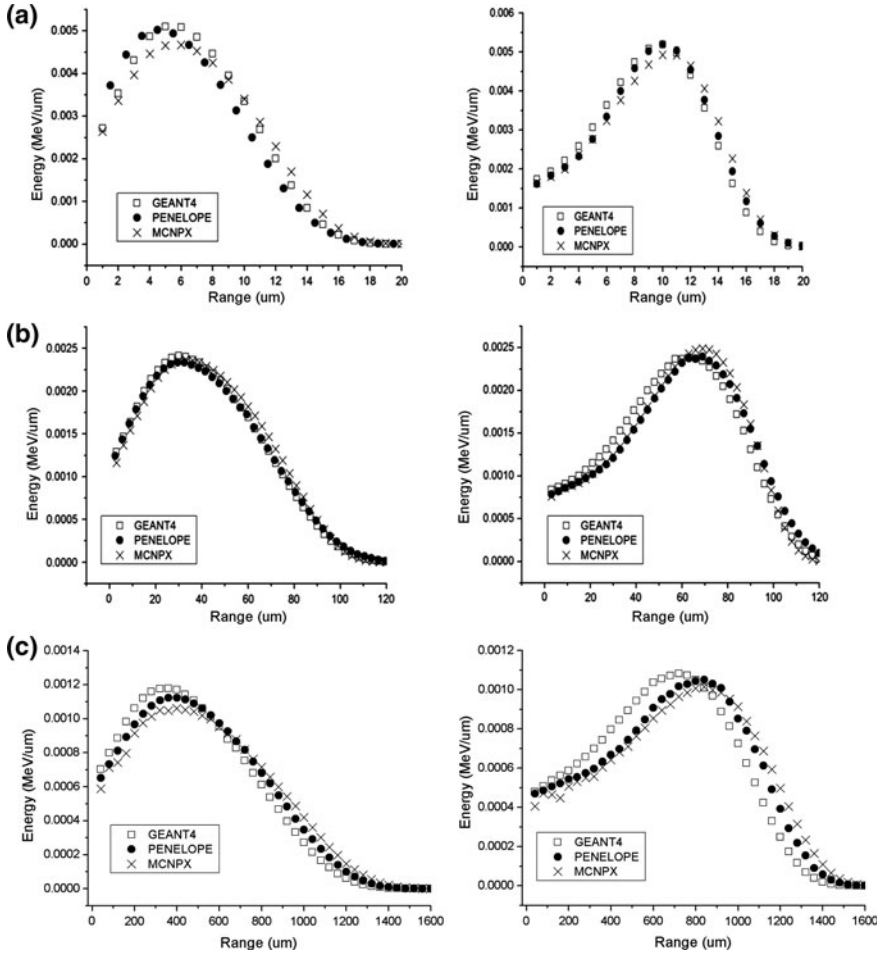
Fig. 3.15 Simulated energy deposition based on the average beta energy versus distance in both the monodirectional beta source incident on a slab (*left*) and an isotropic source at the center of a spherical (*right*) geometries using GEANT4, PENELOPE, and MCNPX codes for **a** S-35, **b** Sr-90, **c** Y-90. [8]

The implications of the observations above are significant. First of all, in using average beta energy to calculate the location of maximum energy deposition, and therefore the location of the transducer, there will be substantial errors in placement of the depletion layer within the cell. A betavoltaic cell is a p-n junction in which the p-type material and n-type material form a junction through compensation. This region in the cell is called the depletion zone. As will be discussed, by adjusting the density of p type impurities and n-type impurities, the depletion layer width will change. Typically, the depletion layer width in a well-designed cell will be about 1 μm thick. If the betavoltaic cell is viewed as a box, then it is possible to locate the
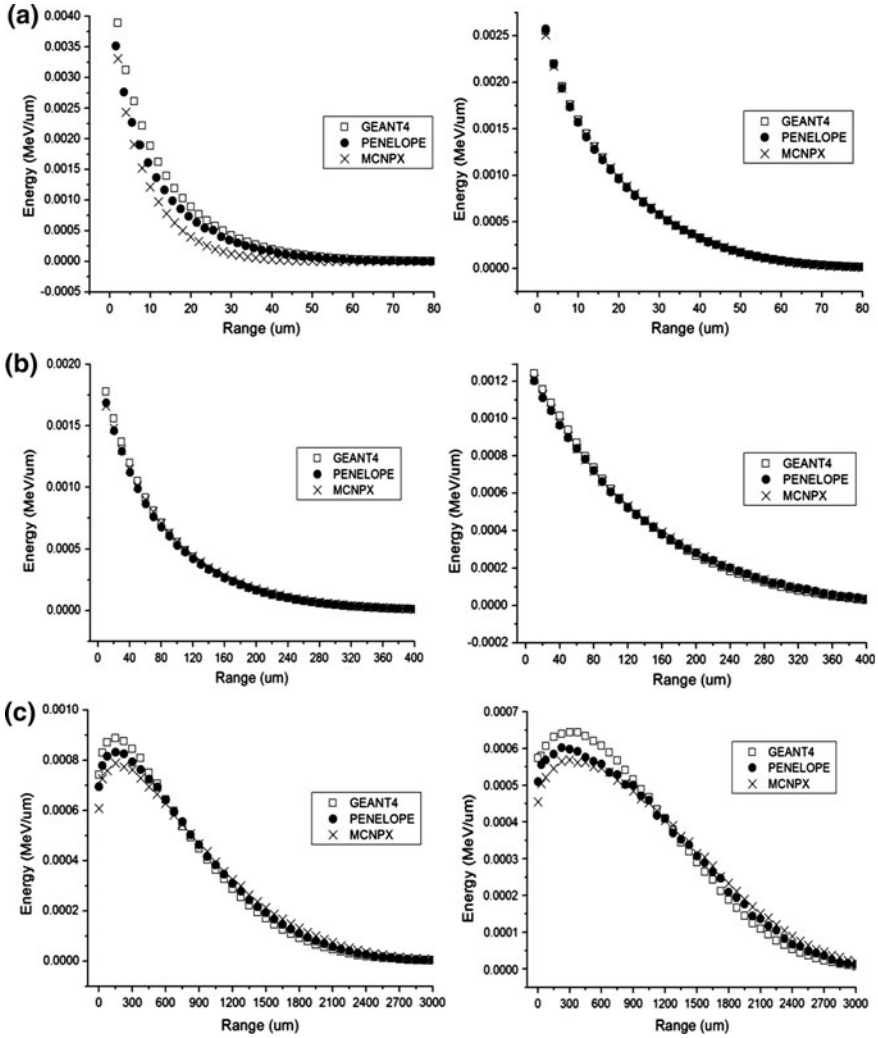
Fig. 3.16 Simulated energy deposition based on the full beta energy spectrum versus distance for the monodirectional beta source incident on a slab (*left*) and an isotropic source at the center of a spherical (*right*) models using GEANT4, PENELOPE, and MCNPX codes for **a** S-35, **b** Sr-90, **c** Y-90 [8]

depletion zone within the boundaries of the box. The challenge is to deposit as much of the energy from the source's beta particles into the 1 μm thick depletion layer as possible. Realizing that the slab model is idealized in that a monodirectional beta particle beam strikes the cell normal to the surface and that the spherical model is idealized by placing a point source at the center of the sphere where the beta source is equidistant from a shell within the sphere, both models vastly over

Table 3.6 Range of beta particles in SiC based on the rules of thumb from Eqs. (3.13–3.16) compared to results in Figs. 3.15 and 3.16

Radioisotope	Range in millimeters		
	Rule of thumb	Average beta	Beta spectrum
S-35	10.6	0.02	0.08
Sr-90	55.1	0.12	0.40
Y-90	344.0	1.6	3.00

The results from the beta spectrum are exact and this table shows the magnitude of expected errors in calculations which use rules of thumb or average beta energy [7]

predict the beta energy being deposited in any given layer. In a realistic device the beta source will be isotropic, thus creating a much greater challenge for depositing the energy of the beta particles in the thin depletion layer. In summary, by using average beta energies in design calculations, significant errors are made in locating the optimum position for the depletion layer. There is also a significant error in calculating the energy transfer rate to the depletion layer (Table 3.6).

3.1.7   What Types of Radiation Work Best with Nuclear Batteries and Why

The types of ionizing radiation that work well with nuclear battery technology where the major goal is to reduce the mass per watt are alpha emitters and beta emitters. Alpha emitters have the shortest ranges and can couple well to many types of transducer technologies. Beta emitters have a much longer range than alpha emitters as well as other complexities which make them a more difficult challenge to use. In the next section, examples of types of transducers that can be used in nuclear battery design are discussed to provide a more complete picture of how alpha and beta emitters can be coupled to the transducer.

3.2   Types of Transducers Used in Nuclear Batteries

The basic operational principles of a nuclear battery can be classified as being based on the generation of heat (Heat Based) or on the generation of ion pairs (Ion Pair Based). Several examples of heat based and ion pair based nuclear batteries will be explored.

3.2.1 Ion Pair Based

Alphavoltaic and betavoltaic cells are typical of semiconductor based energy conversion. These types of cells have been studied since the 1950s [17, 18]. The ionizing radiation creates electron-hole pairs in a semiconductor. The depletion region, where the p-n junction forms, creates a local potential due to the compensation of the n- and p-type regions, and this potential separates the electrons from the holes. The depletion region is limited in thickness to the micrometer range ($\sim$1 µm), as will be shown. If the range of the ionizing radiation in the solid is greater than the depletion region, then the fraction of charged pairs produced that the cell can harvest is low. Alpha particles have a range of about 20 µm in a solid. The theoretical maximum efficiency of an alphavoltaic cell based on silicon carbide was reported to be about 3 % [19]. Likewise, the range of a beta particle in a solid is much higher, thus the corresponding theoretical maximum efficiency of a betavoltic cell is around 1 % [8].

If the depletion layer can be extended beyond the 1 µm range, then the achievable efficiency can be increased [16]. In this reference, tables are generated for the energy transport efficiency (η_d) as a function of distance from the source for idealized geometries in SiC (mono directional beam on a slab or a point source in a sphere—this is an intentional overestimation of transport efficiency, since these idealized geometries represent the most efficient means to transport radiation to the depletion layer and all other designs will be less efficient. In other words, this logic leads to a theoretical maximum). The transport efficiency is maximized by choosing the thickness of the depletion layer and locating it at the peak of the energy deposition curve (see Table 3.7) for an alpha particle. In several references [8, 16, 19] the depletion layer was chosen as 1 µm because the impurity level in a high quality SiC wafer is typically on the order of 1×10^{16} atoms/cm^3. To broaden the depletion layer beyond 1 µm, as will be discussed, the dopant densities should be less than 1×10^{16} atoms/cm^3. However, the ability to reduce impurity densities below 1×10^{16} atoms/cm^3 is a technological challenge when this is about the same impurity density level that a crystal will have when fabricated by typical methods. One can try to compensate for high intrinsic donor or acceptor impurity levels in the wafer by counter-doping with acceptor or donor impurities, respectively to attempt to reduce effective dopant densities below 1×10^{16} atoms/cm^3, but the net increase in impurity density (dopant density plus counter dopant density) will result in shorter carrier lifetimes and a reduction in the efficiency of the cell.

The major problem with a p-n diode is that the n- and p-type impurities in the depletion region are displaced and the structure becomes more random due to ionizing radiation. Thus, the cell ceases to function as a p-n junction relatively quickly. The lifetime of a typical p-n junction beta or alpha voltaic cell is short even at low dose rates. At high dose rates the cell's lifetime could be on the order of milliseconds [20] since radiation damage is a function of dose rate. However, this is not the only problem that p-n diodes have. The other problem is a poor match between the scale length of the radiation and the transducer.

Table 3.7 GEANT4 and SRIM/TRIM calculations for predicting energy deposition in a Depletion Region of 1 μm thick for the slab and sphere models for a 5.307 MeV (e.g., Po-210) alpha beam or point source respectively [19]

Range (μm)	GEANT4						SRIM/TRIM	
	Sphere			Slab			Slab	
	Energy (keV)	% deposited	σ (%)	Energy (keV)	% deposited	σ (%)	Energy (keV)	% deposited
0–1	208	3.92	0.006	208	3.92	0.006	211	3.98
1–2	214	4.03	0.006	214	4.03	0.007	218	4.11
2–3	220	4.15	0.006	220	4.15	0.007	223	4.19
3–4	228	4.29	0.006	228	4.29	0.007	226	4.26
4–5	236	4.44	0.006	236	4.45	0.007	235	4.42
5–6	245	4.61	0.006	245	4.61	0.007	243	4.59
6–7	254	4.79	0.006	254	4.79	0.007	258	4.85
7–8	265	5.00	0.006	266	5.00	0.007	269	5.06
8–9	279	5.25	0.006	279	5.25	0.007	279	5.25
9–10	294	5.55	0.006	294	5.55	0.007	296	5.58
10–11	312	5.89	0.006	313	5.89	0.007	315	5.94
11–12	335	6.32	0.006	335	6.32	0.006	337	6.35
12–13	364	6.86	0.005	364	6.86	0.006	365	6.88
13–14	402	7.58	0.006	402	7.58	0.006	405	7.62
14–15	456	8.60	0.006	457	8.61	0.006	454	8.56
15–16	527	9.93	0.006	527	9.94	0.006	508	9.57
16–17	408	7.68	0.017	407	7.66	0.017	382	7.19
17–18	59	1.12	0.118	58	1.09	0.121	0	0.00
18–19	0	0.00	–	0	0.00	–	0	0.00
19–20	0	0.00	–	0	0.00	–	0	0.00
Total	5307	100.00	–	5307	100.00	–	5220	98.40

The ranges of beta particles do not match well with the depletion widths of p-n diodes except at very low beta energies. Table 3.8 shows the energy deposition characteristics in SiC, Xe gas and ZnSe for betas from tritium (average energy 5.45 keV), Ni-63 (average energy 17.20 keV), Sr-90 (average energy 196.03 keV) and Y-90 (average energy 934 keV). As can be seen from the table, 99.95 % of the beta energy is deposited in SiC within 1.71 μm for tritium, 15.7 μm for N-63, 474 μm for Sr-90 and 2873 μm for Y-90. This data shows that the scale length match for a depletion width of the order of 1 μm is good for tritium but gets much worse as the beta energy increases.

Large ions such as fission fragments have a range on the order of 5 μm. When compared to the 1 μm depletion region, this range is a much better match of scale lengths than that for most beta emitters (where betas at very low energy are on par with 5 μm). In this case the theoretical maximum energy conversion can approach

Table 3.8 Energy deposition characteristics of the beta particles emitted by four radioisotopes in various materials

| Target material	Isotope	E_{exp} (keV)	$E_{tot,M}$ (keV)	% Diff	Depth (in µm) of % $E_{tot,M}$ deposition			
					25 %	50 %	75 %	99.95 %
SiC	H-3	5.45	4.32	20.8	<0.1	0.128	0.292	1.71
	Ni-63	17.20	14.08	18.2	<1	0.968	2.47	15.7
	Sr-90	196.03	159.12	18.8	16.9	49.0	107.7	474
	Y-90	934.40	772.79	17.3	136	366	756	2873
Xe	H-3	5.45	3.72	31.7	29.7	83.7	190	1179
	Ni-63	17.20	11.95	30.6	181	548	1329	8929
	Sr-90	196.03	133.46	31.9	8170	22,880	49,909	247,437
	Y-90	934.40	655.57	29.8	64,838	169,497	348,379	1,148,492
ZnS	H-3	5.45	4.01	26.4	<0.1	0.0987	0.2361	1.3941
	Ni-63	17.20	13.04	24.2	<1	< 1	1.84	12.5
	Sr-90	196.03	101.62	48.2	10.9	31.5	70.5	344
	Y-90	934.40	476.51	49.0	86.97	236.4	498.9	2119

E_{exp} is the expected beta particle energy calculated using the spectral energy distribution [21]. $E_{tot,M}$ is the average beta energy deposited in a sample (where $L_{trans} \gg \lambda_{RadTr}$) as calculated by MCNPX. The % difference between the two methods is shown in column 5. The last four columns describe the depth at which 25, 50, 75 and 99.95 % of $E_{tot,M}$ is deposited for the various beta emitters and materials [7]

20 %. Unfortunately, the radiation damage to the junction will be even more rapid with these larger fragments of higher energy because of large dose rates.

3.2.1.1   Efficiency of a Beta or Alpha Voltaic Cell Based on a Classic P-N Junction

A junction is formed between n- and p-type semiconductor materials. At the junction's interface, the diffusion of charge carriers across the junction sets up a space charge which in turn sets up an electrical potential and electrical field (Fig. 3.17). The depletion region thus has an electrical field which separates electron-hole pairs when they are created by the interaction of radiation with the material. Outside of the depletion region, electron-hole pairs which are created by the interaction of radiation with matter do not have electrical fields to cause their separation. The most likely fate of the charge carriers beyond the depletion region is that they will instead recombine or become trapped by defects. Some of the charge carriers may drift into the depletion region and become part of the cell current driven by the junction's electric field.

Once an electrical field is in place, a driving potential for current flow exists within the cell. The absolute efficiency (η_{ab}) of an energy conversion device is
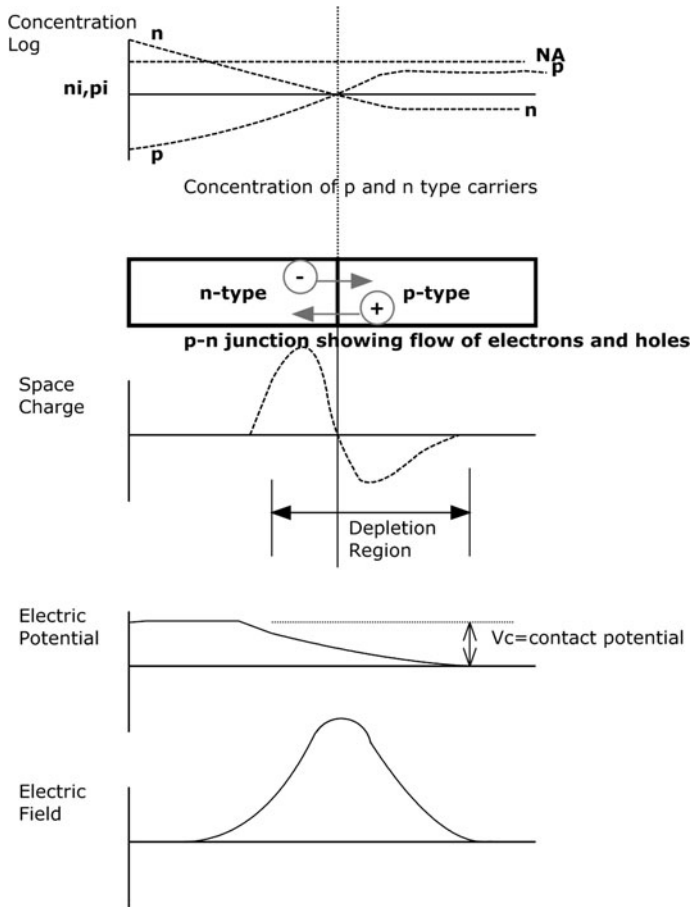
Fig. 3.17 Illustration of a p-n junction showing (from *top* to *bottom*): concentration profiles of n and p type materials; junction interface with charge carriers compensation; diffusion of charge carriers across the junction to produce space charge; the electrical potential; and electric field [7]

always defined as shown in (Eq. 3.22), where P_{out} is the output power from the energy conversion device calculated by (3.23), P_{total} is the total power deposited in the energy-transducing regions of the device, and P_{rad} is the total radioisotope power incident on the cell; P_{total} can be calculated from (3.24).

$$\eta_{ab} = \frac{P_{out}}{P_{total}} \tag{3.22}$$

$$P_{out}(\mathrm{W}) = V(\mathrm{Volts}) \cdot I(\mathrm{A}) \tag{3.23}$$

where V is cell potential in volts and I is the cell current in Amps.

$$P_{total}(\text{W}) = A(\text{Bq}) \cdot E_{dis}\left(\text{eV} \cdot \text{Bq}^{-1}\right) \cdot 1.6 \times 10^{-19}\,(\text{J/eV}) \qquad (3.24)$$

where A is radioactive source activity, E_{dis} is the energy of the particle produced by the decay of the source.

To estimate the cell current I, one can find the maximum current that can be created in the cell by the interaction of radiation with matter. The maximum current will be dependent on the energy transport efficiency of the radiation (beta or alpha) to the depletion zone. This can be expressed in a term which represents the fraction of power that is deposited in the depletion zone and is a factor called η_d (Eq. 3.25). This is typically calculated by using Monte Carlo based transport codes.

$$\text{Power absorbed in depletion zone} = P_{dpl} = P_{total} \cdot \eta_d \qquad (3.25)$$

The maximum rate of charge production in the depletion zone is then found through the number of electron-hole pairs that are created per second in the depletion zone. As discussed previously, Monte Carlo radiation transport codes do not have the capability of modeling electron and ion motion in the media. The use of the W (eV/ion pair) value, which is the average amount of energy that it takes to make an electron-hole pair, in this calculation is necessary. Monte Carlo codes have the capability of calculating the rate of energy absorbed spatially in a material. But, as previously discussed, the spatial and temporal distribution of electrons and ions should be in close proximity to the spatial energy deposition in a solid. Thus, a reasonable estimate is to use the spatial rate of energy lost calculated by Monte Carlo Codes to find the power density in the depletion zone and then use the power density distribution to estimate the electron and ion density distribution. Therefore, the number of electron-hole pairs created per second (N_e) in the depletion zone is,

$$N_e(\#\text{ pairs/s}) = \frac{P_{total}(\text{J/s}) \cdot \eta_d}{\text{W}(\text{eV/ion pair})} \cdot 6.25 \times 10^{18}\,(\text{eV/J}) \qquad (3.26)$$

Assuming that the cell has no losses due to traps, the production rate of electron-hole pairs is proportional to the maximum ideal short circuit current (J_{sc}) in the junction. Ideal short circuit current is equal to the production rate of electron-hole pairs multiplied by the charge per electron (1.6×10^{-19} C):

$$J_{sc} = N_e(\#\text{pairs/s}) \cdot 1.6 \times 10^{-19}(\text{C/pair}) \qquad (3.27)$$

$$J_{sc} = P_{total} \cdot \eta_d/\text{W} \qquad (3.28)$$

The power out is related to the open circuit voltage (V_{oc}) multiplied by the short circuit current (J_{sc}) and the Fill Factor (FF). Thus, the maximum power out that a p-n junction is capable of producing is shown in Eq. (3.29). In Eq. (3.30), P_{max} is

the optimized power output of the cell and the FF is typically > 0.7 for high grade solar cells.

$$P_{out}(\mathrm{W}) = V_{oc}(\mathrm{V}) \cdot J_{sc}(\mathrm{A}) \cdot FF = \frac{V_{oc} \cdot P_{total} \cdot \eta_d \cdot FF}{\mathrm{W}} \tag{3.29}$$

$$FF = \frac{P_{\max}}{V_{oc}J_{sc}} \tag{3.30}$$

Open Circuit Voltage (V_{oc}) and the Driving Potential Efficiency

When electron-hole pairs are created in a solid-state material, any energy transferred to the electron greater than the band-gap energy (E_g) eventually ends up becoming heat. Thus, the process of creating electron-hole pairs has a material dependent efficiency (shown in Table 3.9). When creating an electron-hole pair, the energy that is expended to create the charge carriers is E_g (eV). In a beta or alpha voltaic cell, the electron-hole pair is driven by the junction voltage. The maximum voltage is the open circuit voltage V_{oc}. The maximum power produced by the cell is thus the open circuit voltage times the short circuit current, J_{sc}. Current flow I (C/s) is electron density ρ_e (electrons/m^3) times charge per electron times the drift velocity u (m/s) times the surface area A (m^2). This is very similar to a photovoltaic solar cell, and therefore, for a nuclear battery the maximum possible current will be equal to the number of electron-hole pairs created in the depletion zone per second, assuming no recombination losses.

Using an alternate definition, one can start with the electron-hole production rate through the interaction of the radiation with matter in Eq. (3.26) to define the short circuit current, as in Eq. (3.28), and the maximum power out in Eq. (3.29). The power expended to create the current flow (P_{ex}) can be defined as the electron flow rate times the energy used to form a single electron-hole pair (e.g., the band gap (E_g) energy),

$$P_{ex}(\mathrm{W}) = N_e(\mathrm{pair/s}) \cdot E_g(\mathrm{eV/pair}) \cdot 1.6 \times 10^{-19}(\mathrm{J/eV}) \tag{3.31}$$

The concept of the driving potential efficiency (η_{dp}) was introduced by Oh, et al. [19]; it originates from the relationship between the open circuit voltage and the band gap of the cell material. The magnitude of the open circuit voltage is less than or equal to the material band gap. A simple way to consider this relationship is that the cell power output will be less than the power expended in creating the electron-hole pairs. The ratio of the power out to the power expended is the driving potential efficiency, as shown in Eqs. (3.32) and (3.33). The open circuit voltage can then be represented as the product of the driving potential efficiency and the band gap, shown in Eq. (3.34).

Table 3.9 Properties for some common semiconductor materials which are useful for direct nuclear energy conversion [22]

Material	Minimum band-gap (E_g) (eV)	Electron drift mobility (μ) (cm²/V-s)	Density (ρ) (g/cm³)	Atomic mass (g/mol)	Molar density (mol/cm³)	Displacement energy (E_d) (eV)	Mean ionization energy (W eV) [22]	Klein Formula* (W eV)	Eg/ W
Silicon	1.12	1450	2.329	28.1	0.0829	~19	3.63	3.64	0.308
Germanium	0.68	3900	5.323	72.6	0.0733	30	2.96	2.404	0.23
Gallium arsenide	1.42	8500	5.317	144.6	0.0368	10	4.13	4.476	0.344
Silicon carbide	2.9	400	3.22	40.1	0.0803	28	6.88	8.62	0.421
Gallium nitride	3.39	1000	6.15	83.7	0.0735	24	8.9	9.99	0.381
Diamond	5.48	1800	3.515	12	0.293	43	12.4	15.84	0.442

*Klein Formula for predicting W values for semiconductors (W = 2.8 × Eg + 0.5 eV [23]). The predicted values from the Klein Formula are different than the measured values especially at larger band-gap energies

$$\eta_{dp} = \frac{P_{out}}{P_{ex}} = \frac{V_{oc}(\text{V}) \cdot \left(\frac{N_e(\text{electron/s})}{6.25 \times 10^{18}(\text{electron/c})}\right)}{E_g(\text{eV/pair}) \cdot N_e(\text{pair/s}) \cdot 1.6 \times 10^{-19}(\text{J/eV})} \tag{3.32}$$

$$\eta_{dp} = \frac{V_{oc}}{E_g} \tag{3.33}$$

$$V_{oc} = \eta_{dp} \cdot E_g \tag{3.34}$$

So, the maximum efficiency can be written in terms of the power out and total power of the emitter and can be calculated from Eq. (3.35). Substituting Eq. (3.32) causes this expression to simplify to Eq. (3.36). Similarly, the use of the pair production efficiency η_{pp} discussed by Oh, et al. [19], shown in Eq. (3.37), will resolve Eq. (3.36) to the convenient form shown in Eq. (3.38).

$$\eta = P_{out}/P_{total} = V_{oc}(\text{V}) \cdot \eta_d \cdot \left(\frac{FF}{\text{W(eV/pair)}}\right) \tag{3.35}$$

$$\eta = \eta_{dp} \cdot E_g \cdot \eta_d \cdot \frac{FF}{\text{W(eV/pair)}} \tag{3.36}$$

$$\eta_{pp} = \frac{E_g(\text{eV})}{\text{W(eV/pair)}} \tag{3.37}$$

$$\eta = \eta_{dp} \cdot \eta_d \cdot \eta_{pp} \cdot FF \tag{3.38}$$

The efficiency calculation requires one more parameter, the open circuit voltage. Using the ideal PV cell-equivalent circuit in Fig. 3.18, the output current for an ideal PV cell is related to the dark saturation current of the p-n junction (I_D) and radiation generated current (I_L) by taking the nodal balance of the circuit in Eq. (3.42).

Fig. 3.18 Ideal alpha or beta voltaic cell equivalent circuit
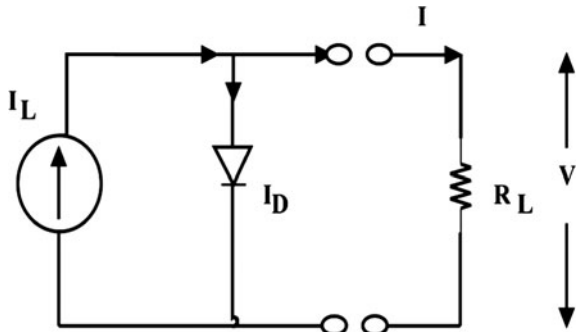
The open circuit voltage is a function of the dark saturation current (I_0) and the radiation generated current (I_L). The diode current is a function of the dark saturation current in Eq. (3.39), where I_0 is the reverse saturation current which is a function of the material and temperature, q is the electron charge (1.602×10^{-19} C), k_B is Boltzmann's constant (1.381×10^{-23} J/K), T is the cell temperature in Kelvin and n is the shape factor (for an ideal cell $n = 1$). The open circuit voltage occurs when the radiation generated current balances the diode current. So setting $I = 0$ and using Eq. (3.40) for I_D, one can find the open circuit voltage as shown in Eq. (3.41).

$$I = I_L - I_D \tag{3.39}$$

$$I_D = I_0 \left(e^{\frac{qV}{nk_BT}} - 1 \right) \tag{3.40}$$

$$V_{oc} = \frac{nk_BT}{q} \cdot \ln\left(\frac{I_L}{I_0} + 1\right) \tag{3.41}$$

There is also a relationship between band gap energy and open circuit voltage. The dark saturation current I_0 depends on the charge carriers due to the temperature of the cell T. The relationship between the dark saturation current and band-gap E_g is shown in Eq. (3.42).

$$I_0 = D \cdot T^3 \cdot e^{-\frac{qE_g}{nk_BT}} \tag{3.42}$$

As the band-gap increases, the dark saturation current will decrease. Thus, open circuit voltage will increase for the ideal cell as band gap energy goes up. The highest open circuit voltage achieved for a wide band-gap cell (e.g., diamond) was 2.6 V [24], which is equivalent to a driving potential efficiency (η_{dp}) of 0.48.

Depletion Zone Width and Current

The collection probability is the probability that a carrier generated in a cell by the interaction of radiation with matter in a region of the cell will be collected and thereby contribute to the radiation generated current flow (I_L). The carriers generated in the depletion region will have a collection probability of unity because the electron-hole pairs are quickly separated by the electric field and eventually are collected. Outside of the depletion zone, the collection probability decreases because the electron-hole pairs must diffuse into the depletion region. If the distance is more than one diffusion length away from the junction, the collection probability is negligible (Fig. 3.19). For example, the diffusion length in SiC can vary from 0.07 μm to a few μm depending on material defects [25, 26].

In the determination of the width of the depletion zone, the conduction of charge carriers is important, but even of more significance is the lifetime of the charge
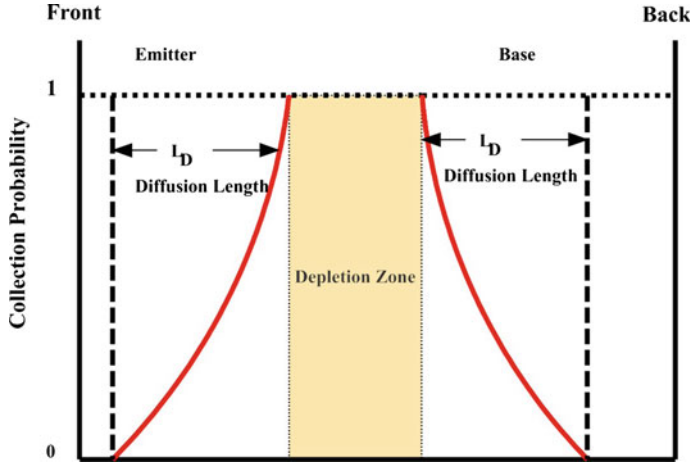
Fig. 3.19 The collection probability for a linearly graded alpha or beta voltaic structure. The collection probability is negligible beyond the diffusion length of carriers

carriers within the semiconducting material, define as the time from their creation or injection to their subsequent collection by a true conductor (e.g., copper). The lifetime of charge carriers (electrons and holes) in semiconductors are governed by the traps that are present within the band structure. The consequence is that the depletion region is limited to a very small thickness. This means that only the energy that is deposited by ionizing radiation within the depletion region has a collection efficiency of unity for power production. The depletion layer thus limits the efficiency of the energy conversion system. Equations (3.43) through (3.45) describe the pertinent properties of the semiconductor through the intrinsic carrier concentration, n_i, the voltage across the depletion region, V_{bi}, and the depletion region width, W [27].

$$n_i = 2\left(\frac{2\pi k_B T}{h^2}\right)^{3/2}(m_n m_p)^{3/4}\exp\left(-\frac{E_g}{2k_B T}\right)$$ (3.43)

where k_B is Boltzmann's constant, T is the temperature of the semiconductor in Kelvin, E_g is the band gap energy, and m_p and m_c are the effective masses of the holes and electrons, respectively.

$$V_{bi} = \frac{k_B T}{e}\ln\left(\frac{N_a N_d}{n_i^2}\right)$$ (3.44)

where e is the unit electron charge, N_a is the relative concentration of vacancies available in the p-type region, N_d is the relative concentration of electrons in the n-type region.

$$W = \left(\frac{2\varepsilon_s V_{bi}}{e} \cdot \frac{N_a + N_d}{N_a N_d} \right)^{1/2} \tag{3.45}$$

where ε_s is the permittivity.

As can be seen in Eqs. (3.43–3.45), the potential barrier and the depletion region width are based on the intrinsic semiconductor properties and the doping concentrations N_a and N_d in the respective p- and n-type regions of the semiconductor. Doping concentration is the primary means of varying the potential barrier and depletion width. The equations show that by reducing the doping concentrations, larger depletion widths are formed, but at a penalty of a lower potential barrier. The potential approaches zero as the doping concentration product approaches the square of the intrinsic carrier concentration and there is no depletion region. In addition, the doping concentration must be greater than the injected charge from the depletion region for the transport of the generated charges to be in the low injection regime, and very low doping concentrations are not controllable in a semiconductor.

In order to understand the depletion width, 4H-SiC is chosen as an example material. For this semiconductor, ε_s is about 10 [28], m_n and m_p were taken to be 1.2 m_e and 0.76 m_e, respectively, and the band gap is approximately 3.25 eV at room temperature [29]. Using a temperature of 300 K in Eq. (3.43), the intrinsic doping concentration for this material was found to be 9.5×10^{-9} cm^{-3}. This information is used with Eqs. (3.44) and (3.45) and both N_d and N_a are varied between 10^{15} and 10^{20} cm^{-3} to calculate the range of depletion widths in silicon carbide (see Fig. 3.20). It can be seen that the largest depletion region width in silicon carbide is 2.6 μm. This shows that the depletion width is the factor that limits the absorption efficiency of ionizing radiation in any planar single p-n junction-based nuclear battery system. It should be noted that in order to achieve a depletion width of 2.6 μm, the impurity levels have to be on the order of 0.1 ppm. Achieving sub-ppm impurity levels is difficult for SiC. It is more reasonable to obtain impurity levels in the 1–10 ppm range. This leads to the conclusion that a depletion width on the order of 1 μm is approximately the maximum size that is feasible [19].

3.2.2   Schottky Barriers

The Schottky barrier is a potential energy barrier between a metal and a semiconductor that forms a diode. It depends on the differential work function between a semiconductor and a metal contact. The surface interface between the metal and semiconductor forms a depletion region that is effectively 100s of nanometers thick. Thus the effective size of the energy conversion region is thin and not well matched to the ranges of ionizing radiation. The theoretical maximum efficiency for Schottky barrier structures is approximately 0.3 % for alphas and approximately 0.1 % for low energy betas. Schottky barriers are less susceptible to radiation damage since
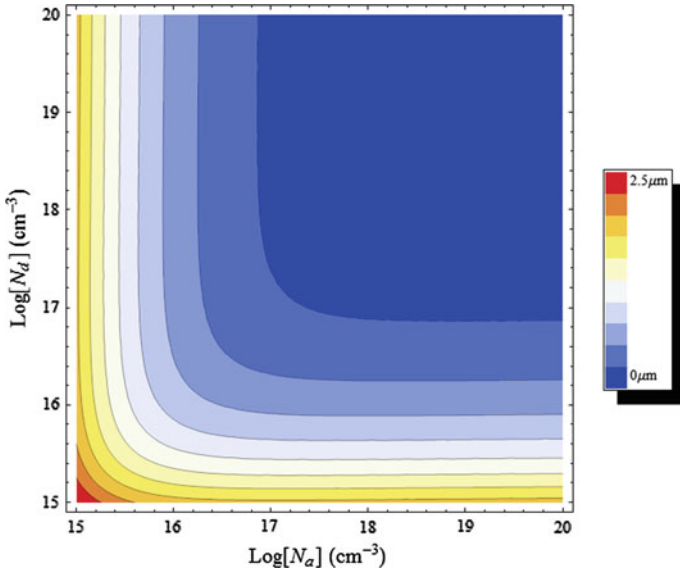
Fig. 3.20 Density plot indicating depletion region width for varying donor and acceptor density concentrations in 4H-SiC [7]

the atomic layer bonding the metal to the semiconductor is thin and is thus less prone to displacements caused by the radiation. Schottky barriers can be formed between liquid semiconductors and metals. These types of Schottky diodes are not as prone to radiation damage since the liquid constantly wets the interface.

Fission fragments have a better match (a range of about 5 μm) for the ∼ 100 nm depletion region of a Schottky barrier diode. For fission reactions combined with a Schottky barrier diode, the theoretical maximum efficiency approaches 3 %. This is still not attractive enough for a large scale direct energy conversion system in fission reactors.

A Schottky barrier is formed when two different materials with different work functions are placed in direct contact with each other. A Fermi potential will form at the material interface. Because this boundary between the two materials is sharp, a Schottky barrier will have a much thinner depletion zone than a p-n junction. The width of the depletion region for a Schottky barrier, W, is expressed by Sze and Ng [30]:

$$W = \sqrt{\frac{2\varepsilon_s}{qN}(V_{bi} - V_A)} \tag{3.46}$$

$$\eta_{dp} = \frac{V_{bi}}{E_g} \tag{3.47}$$

where V_{bi} is the built-in voltage in the Schottky contact, N is the dopant density, q is the unit charge, ε_s is the permittivity of the semiconductor, and V_A is the applied voltage across the junction in the forward bias. In the beta or alpha voltaic mode, $V_A = 0$. A typical barrier height for a SiC Schottky barrier is 1 V [31]. The depletion width for a Ni/4H-SiC Schottky diode is given for several donor concentrations in Östlund [32]. With a dopant density of 1×10^{17} cm^{-3}, the depletion width of a Ni/4H-SiC Schottky diode is about 0.25 µm.

The efficiency of a Schottky barrier diode for nuclear energy conversion will be significantly less than a p-n diode due to the smaller depletion width as well as a lower potential barrier height (V_{bi}). The smaller depletion width will decrease the transducer scale length and thus will decrease efficiency. The lower potential barrier height will lower the driving potential efficiency in Eq. (3.46) where V_{bi} is substituted for V_{oc}. The difference between V_{bi} and V_{oc} can be substantial, $V_{bi} = 1$ V and $V_{oc} = 2.04$ V [33], which can reduce η_{dp} by 50 %.

3.2.2.1   Liquid Semiconductor Schottky Barrier

The use of a liquid semiconductor to mitigate radiation damage to a nuclear battery was patented with a priority date of November 21, 2003 [34]. The premise of this cell is that two plates with a liquid semiconductor (such as selenium) between them, one forming a Schottky barrier and the other an Ohmic contact, can form a potential barrier which will serve as the driving force for the collection of electron-hole pairs created in the cell. The semiconducting property of a molten semiconducting metal, such as germanium, is accompanied by a rapid temperature-dependent increase in conductivity. Thus, the molten material has metallic properties. There exist, however, some materials which upon melting do not exhibit metallic conductivity but retain their semiconducting properties. These materials are primarily the chalcogens (oxygen, sulfur, selenium, tellurium and polonium). Selenium is particularly interesting due to the decrease in conductivity as temperatures increases, thus exhibiting semiconducting behavior at high temperatures. The preferred embodiment of the cell uses selenium as the liquid semiconductor. There is a depletion region that is formed in the cell by the Schottky barrier where the collection efficiency will be close to 100 %, and there will be a rapid drop off in collection efficiency a diffusion length or so beyond the depletion region. A test cell was built by Global Technologies Inc. and operated at an efficiency of about 1 %. This efficiency is greater than the expected efficiencies of solid-state Schottky cells. However, the diffusion lengths in a liquid medium should be larger than those in a solid, which in turn should lead to higher efficiencies than solid-state Schottky cells. Thus, the 1 % efficiency reported is reasonable. The basic technology behind the Global Technology Inc. liquid selenium Schottky cell has since been explored by others using a beta source that is mixed with the liquid [35].

A theoretical study was published on a liquid nuclear battery by the Jet Propulsion Laboratory. This study [36] used liquid gallium as the electrolyte in an electrolytic cell. The driving voltage was the work function difference between the

anode and cathode ($\sim$1.6 V). The basis for the device is that the liquid gallium would be a semi-metal (the conductivity of liquid gallium is linear with temperature and is on the order of 26–46 $\mu\Omega$-cm, which appears to be metallic—e.g., silver has a resistivity at room temperature of 1.59 $\mu\Omega$-cm). Furthermore, it was argued that the gallium ion does not immediately recombine, thus leading to high current collection efficiencies. Unfortunately, the ion and electron mobilities and carrier lifetimes in the liquid metal were not discussed, making it difficult to evaluate the study.

3.2.3 Direct Charge Collection

The Direct Charge Nuclear Battery (DCNB) is based on the conversion of the kinetic energy of a charged particle generated by nuclear decay to potential energy stored in an electric field. Several theories have been developed to describe the operation of a DCNB [37, 38].

The following derivation is more fundamental than many of the other approaches. It examines how the kinetic energy of the charged particle is converted to stored energy in an electric field. The DCNB consists of a radioisotope source which is the emitter of charged particles. The source is thin enough so as to allow the bulk of the kinetic energy in the emitted particle to escape the layer of source material. The DCNB also has a collector which is separated from the charged particle source by a vacuum (a separation distance of l). The breakdown voltage in a vacuum is about 1×10^5 V/cm [39]. The vacuum is void of atoms which will interact with the charged particle and absorb some of its energy. Thus, the particle will slow down due to the electric field and it will collide with the collector. The charge will remain in the collector, contributing an additional charge to add to the strength of the electrical field. This effectively converts the kinetic energy of the charged particle into stored potential energy in the form of an electric field.

3.2.3.1 The Ideal Match Between the Electric Field and the Ionizing Radiation

In an ideal system, the charged particle will travel perpendicular to the electric field where it will slow down sufficiently so that its velocity is zero when it attaches to the collector. Because there is no kinetic energy remaining in the charged particle when it attaches to the collector in this ideal match-up, its energy is fully converted into stored potential energy in the DCNB. The additional charge will incrementally increase the electric field created by the separation of the charged particle from its paired opposite (e.g., for a beta particle the paired opposite is an ion) trapped in the radioisotope layer. If the match-up is less than ideal, the charged particle still has kinetic energy when it collides with the collector. This remaining kinetic energy in

the particle generates heat and ionization (as described in Chap. 1), which effectively heats the collector. In this case the excess kinetic energy is wasted.
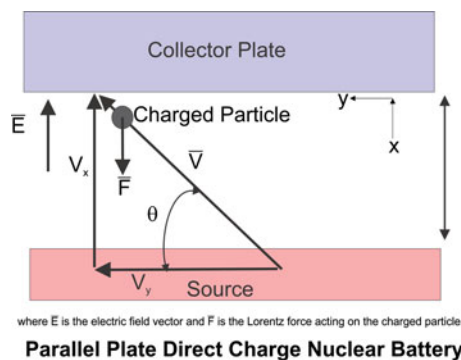
No DCNB design is ideal, thus a significant amount of the kinetic energy in the charged particles ejected by the radiation source will interact with matter and generate heat. Thus there are significant inefficiencies which will be described in the following text. These inefficiencies in a DCNB are associated with imperfect geometries and other import factors.

- One factor is self-absorption, where energy is lost as the charged particle moves through the source layer.
- There will also be losses associated with the charged particle emission being isotropic. Some part of the velocity vector will be perpendicular to the electric field and the energy associated with the perpendicular velocity component will be a loss because that portion of the energy will eventually interact with matter and will be converted into heat.
- There will be inefficiencies in the electron collections process such as electron backscatter and electron emission from the collector material.

DCNB Design and Inefficiencies

Putting the above concepts into context, envision a process where the source (for this construct it is assumed that the source is a beta emitter) is coated on a rectangular plate located a distance "*l*" from the collector is a parallel plate (see Fig. 3.21). The space between the two plates is a vacuum.

Each particle emitted has an equal probability of being emitted at any angle of emission. The particles which are collected must have a high enough kinetic energy

where E is the electric field vector and F is the Lorentz force acting on the charged particle.

Parallel Plate Direct Charge Nuclear Battery

Fig. 3.21 An illustration of a parallel plate DCNB. The electron is emitted at an angle θ. The electric field is in the positive x direction which impedes the electron's velocity vector in the x direction due to the Lorentz force. (Note that if the charged particle were an ion, simply reverse the field. The ion would experience a Lorentz force which impedes its velocity vector in the x direction)

to overcome the electrical field created by the accumulated charge on the collector plate. Looking at the charge build up process, the first particle which is emitted has no electrical potential to overcome, so it will collide with the collection plate and will interact with the material causing the particle to slow down. The transfer of kinetic energy from the charged particle to the collector plate material results in the collector plate gaining heat. Each charged particle that is collected will incrementally build up the electric field. The electric field for a parallel plate capacitor is,

$$\vec{E} = \frac{Q}{A\varepsilon_0}\hat{x} \qquad (3.48)$$

where Q is the total charge in Coulombs collected on the plate, A is the area of the plate, ε_0 is the permittivity of free space (8.8542×10^{-12} Farads/m) and $\hat{x}$ is a unit vector in the x direction.

The electrical potential between the parallel plates is,

$$|V| = El \qquad (3.49)$$

where $|V|$ is the absolute value of the electrical potential in volts, E is the magnitude of the electric field vector, l is the distance between the plates in meters.

To provide an idea of how much energy is lost during the charge buildup phase, assume that the source of charged particles is a monoenergetic electron beam (of energy 100 keV) moving in the positive x direction, striking a 0.1 m by 0.1 m plate (a large enough area where edge effects considerations on the electric field are not significant). As previously discussed, the vacuum breakdown voltage is 1×10^7 V/m. Thus a 0.01 m spacing (l) between the plates is sufficient to prohibit a breakdown for a voltage of 1×10^5 V (i.e., the ideal matchup between the electric field and the 100 keV particle). Using Eqs. (3.48) and (3.49), an equation for the charge on the plate needed to produce 100 kV is,

$$Q = E_x A \varepsilon_0 = 10^7 \times 10^{-2} \times 8.854 \times 10^{-12} = 8.854 \times 10^{-7}\,\text{C} \qquad (3.50)$$

The number of electrons (N_e) needed to produce this charge is,

$$N_e = 8.854 \times 10^{-7}\text{C}/1.66 \times 10^{-19}(\text{C/electron}) = 5.53 \times 10^{12}.$$

The buildup time (τ_b) to fully charge the plate for a source that produces 3.7×10^{10} electrons per second is

$$\tau_b = 5.5353 \times 10^{12}\text{electrons}/3.77 \times 10^{10} = 150\,\text{s} = 2.5\,\text{min}.$$

As charge is accumulated on the plate, each electron which hits the plate will lose some of its kinetic energy to the plate material. The kinetic energy lost (KE_{lost}) can be calculated by summing the lost energy for each electron. The kinetic energy of the electron (KE_e) is,

$$KE_e = 100 \times 10^3 \, \text{eV/electron} \times 1.66 \times 10^{-19} \, \text{J/eV} = 1.66 \times 10^{-14} \, \text{J}.$$

The energy which is converted to potential energy stored in the electric field is $eE_x l$. As a charge is captured by the plate, the incremental field is increased by $e^2 l/A\varepsilon_0$. Thus KE_{lost} is found by the sum,

$$KE_{lost} = \sum_{0}^{5.53 \times 10^{12}} \left(1.6 \times 10^{-14} - n \cdot 2.881 \times 10^{-27} \right) \sim 0.5 \qquad (3.51)$$

where,

$$\frac{e^2 l}{A\varepsilon_0} = 2.881 \times 10^{-27}.$$

The ideal efficiency during the charge build up phase for converting kinetic energy to stored electrical field energy for a mono-energetic, mono-directional e-beam is $\sim 50\%$.

If the DCNB depends on the radioisotope to build up the charge on the plate, half of the kinetic energy in the particles is used to build up the electric field and the rest is lost to heat. Thus the efficiency of converting kinetic energy into stored potential energy in the electrical field for an ideal charge build up based system (η_b) is about 50%.

Some DCNB systems function by first building up a charge followed by a discharge. These are dynamic direct charge nuclear batteries and are limited in efficiency by the charge build-up phase. The efficiency of the dynamic systems are primarily limited by the charge build-up process (η_b), the mismatch of the field strength with the energy distribution of the particles, the transport efficiency of the particles out of the coating, the angular distribution of the particles being emitted, electron backscatter, and electron emission from the surface.

Some DCNB systems operate at steady-state by continually collecting charge and bleeding it off at a rate equal to the collection rate. During steady-state operation, enough charge is accumulated on the plate to produce a static electric field in which the charged particles emitted by the source slow down. The efficiency of the steady-state systems is primarily limited by the mismatch of the field strength with the energy distribution of the particles (η_{ED}), the transport efficiency of the particles out of the coating (η_{tr}), the effect of the angular distribution of the particles being emitted ($\eta_m \, \eta_f$), electron backscatter (η_{BS}) and electron emission (η_{EM}) from the surface. The impact of these efficiencies on the DCNB system efficiencies will be discussed.

Thus, the system efficiency for the Dynamic DCNB is,

$$\eta_{Dynamic} = \eta_b \eta_{ED} \eta_{tr} \eta_m \eta_f \eta_{BS} \eta_{EM} \qquad (3.52)$$

and the system efficiency for a steady state DCNB is,

$$\eta_{SS} = \eta_{ED}\eta_{tr}\eta_{m}\eta_{f}\eta_{BS}\eta_{EM} \qquad (3.53)$$

The potential energy that is stored per unit volume by the electric field of the parallel plate configuration is,

$$\rho_{\vec{E}} = \frac{\text{Energy}}{\text{Volume}} = \frac{1}{2}\varepsilon_0 E_x^2 \qquad (3.54)$$

where ε_0 is the permittivity of free space, $\rho_{\vec{E}}$ is the energy density, and Volume is plate surface area (A) times gap between the plates (l).

Mismatch of the Electric Field with the Energy Distribution of the Particles

After enough charge is trapped on the collector plate to produce an electric field which can slow down the particles from the source, a good fraction of the particle's kinetic energy can be stored in the electric field. The process depends on the Lorentz force to slow down the charged particle (Eq. 3.55).

$$\vec{F} = -e\vec{E} \qquad (3.55)$$

where $\vec{E}$ is the electric field.

The work in moving the charged particle from the source plate to the collector plate is,

$$W = \int_0^l -e\vec{E} \cdot d\vec{x} = -eE_x l \qquad (3.56)$$

If the particle velocity is sufficient to overcome the repulsive Lorentz force, it will contribute to the cumulative charge on the collector plate and will incrementally increase the electric field strength. It is important to realize that in the parallel plate configuration only the velocity component in the x direction (V_x) is impeded by the Lorentz force. Because of isotropic emission, the V_x component (Eqs. 3.57 and 3.58) will vary as a function of emission angle. The V_y component will not contribute to the energy stored in the electrical field and the energy associated with the y component of velocity is lost.

$$KE_x = \frac{1}{2}m_q V_x^2 \qquad (3.57)$$

where m_q is the mass of the charged particle.

The x component of the velocity is,

$$V_x = V \sin \theta \tag{3.58}$$

Thus,

$$KE_x = \frac{1}{2} m_q V^2 \sin^2 \theta = KE \sin^2 \theta \tag{3.59}$$

The fraction of energy which is stored as potential energy in the electrical field for this particle (η_q) is the kinetic energy in the x component times the fraction of this energy which is stored in the electric field (Eqs. 3.60 and 3.61).

$$\eta_q = \frac{KE \sin^2 \theta}{KE} \eta_{\vec{E}} = \eta_{\vec{E}} \sin^2 \theta \tag{3.60}$$

where,

$$\eta_{\vec{E}} = \begin{cases} \frac{eE_x l}{KE \sin^2 \theta}, & \text{for } KE \sin^2 \theta > eE_x l \\ 1, & \text{for } KE \sin^2 \theta = eE_x l \\ 0, & \text{for } KE \sin^2 \theta < eE_x l \end{cases} \tag{3.61}$$

η_q is an idealized form of the energy distribution factor η_{ED} (meaning $\eta_q > \eta_{ED}$) since η_q is derived for a mono-energetic charged particle source. Beta particles are emitted with a spectrum of energies as discussed in Appendix A, thus finding η_{ED} requires a more complex analysis. The spectral distribution of the beta particles must be accounted for in Eq. (3.60) in the KE term. The term becomes a distribution function for particle kinetic energy $F(E)$.

As previously discussed, the energy distribution is only one inefficiency factor. There are other factors which reduce the DCNB efficiency including isotropic emission ($\eta_j \eta_m$), energy losses from charged particles transporting out of source materials (η_{tr}), effects from secondary electron emission (η_{SEE}), and electron backscatter.

Effects of Angular Distribution

The angular distribution of the particles emitted by the source will reduce the efficiency of the device. Primarily, the electric field acts on the velocity component of the particle which is parallel to it due to the Lorentz force. The components of velocity which are perpendicular to the electric field are not affected, and thus the energy associated with the perpendicular components of velocity is lost. Another effect that is important is the loss of energy due to the mismatch of the velocity component with the field. Only particles with $KE_x = eE_x l$ are perfectly matched with the field and convert kinetic energy to potential energy stored in the field. If
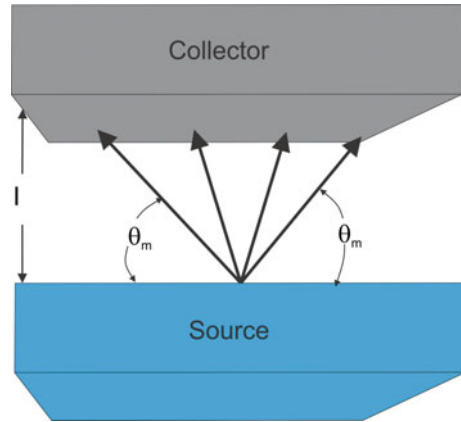
$KE_x > eE_xl$, then some of the energy is stored as potential energy in the field (the portion equal to eE_xl), while the remainder of the energy is lost. If $KE_x < eE_xl$, then none of the kinetic energy is converted to potential energy in the field. Based on these observations, there should be an emission angle which optimizes the efficiency of the DCNB. The operating voltage of a cell which has an isotropic source will be lower than that of the cell with a mono-energetic, mono-directional source because of the broad range of V_x due to the emission angle. The optimum operating voltage can be analytically determined.

In order to understand the effect of isotropic emission, assume that the kinetic energy of the particles are mono-energetic. An angle θ_m is defined which represents the emission angle where the electrical field is able to reduce V_x to zero when it reaches the collector plate. This emission angle is the point which determines the operating voltage of the DCNB (see Fig. 3.22). The V_x of the particle emitted at θ_m is,

$$V_x = V \sin \theta_m \tag{3.62}$$

The kinetic energy of this particle is,

$$KE_x = \frac{1}{2} m_q V^2 \sin^2 \theta_m = KE \sin^2 \theta_m \tag{3.63}$$

The electric field which reduces the particle's Vx at an emission angle θ_m is found by setting Eq. (3.56) equal to Eq. (3.63),

$$elE_x = KE \sin^2 \theta_m \tag{3.64}$$

So,

$$E_x = \frac{KE \sin^2 \theta_m}{el} \tag{3.65}$$

where *KE* is in electron volts, e is 1.6×10^{-19} C and l is the distance between the plates. The field strength will be in V/m.

Any particle that is emitted at an angle less than θ_m is turned around by the electric field before reaching the plate. The particles emitted at an angle equal to or greater than θ_m are collected. However, as indicated by Eq. (3.61), particles which are emitted at an angle greater than θ_m have excess energy (KE-elE_x) which goes into heating the collector plate. The fraction of kinetic energy that contributes to the potential energy of the field for any particle which is emitted at an angle greater than or equal to θ_m is,

$$\eta_m = \frac{KE \sin^2 \theta_m}{KE} = \sin^2 \theta_m \tag{3.66}$$

The fraction of particles (η_f) emitted by an isotropic source which have angles of emission between θ_m and $\pi - \theta_m$ is,

$$\eta_f = \frac{\pi - 2\theta_m}{2\pi} \tag{3.67}$$

So, the ideal efficiency of a parallel plate DCNB with a mono-energetic isotropic source is,

$$\eta_{ideal} = \eta_f \eta_m = \sin^2 \theta_m \frac{\pi - 2\theta_m}{2\pi} \tag{3.68}$$

The ideal efficiency will be reduced if the particles are not mono-energetic (e.g., beta particle spectrum), if there is electron backscatter, and/or if there is electron emission.

Using Eq. (3.68) and plotting ideal efficiency (η_{ideal}) as a function of the minimum angle of emission (θ_m), the optimum efficiency for an ideal DCNB using an isotropic mono-energetic source can be found (Fig. 3.23).

The ideal system efficiency does not account for energy distribution effects (η_{ED}), transport effects (η_{tr}), electron backscatter effects (η_{BS}), or electron emission effects (η_{EM}). It simply sets a theoretical maximum efficiency for a steady-state DCNB. In the case of an isotropic source emitting particles with energy of 100 keV as shown in Fig. 3.23, the operating voltage will be maximized for an emission angle of about 1 rad (or 57.3°) which is 70.8 kV. The ideal efficiency will be about 13.5 %.
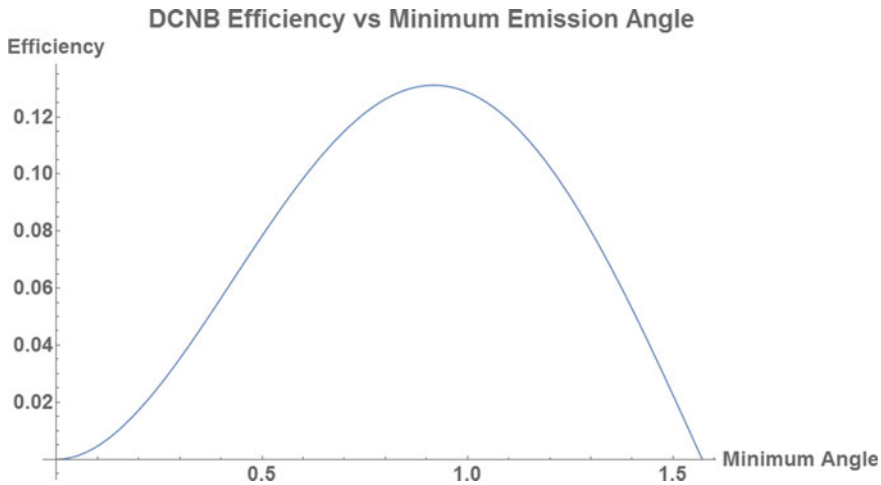
Fig. 3.23 The ideal efficiency of a DCNB as a function of minimum angle of emission

3.2.3.2   Reciprocating Cantilever

A reciprocating cantilever nuclear battery is a form of a DCNB. The principle of operation of a reciprocating cantilever is that a radioisotope source emits charge and that charge is collected on a receiver (the cantilever material). The kinetic energy from the charged particles is converted into potential energy stored in an electromagnetic field. The cantilever is a flexible column and the Lorentz force causes the column to bend towards the plate where the positive ions accumulate. When the column touches the plate, then current will flow. This is a dynamic charge build up as described by Eq. (3.51). In a dynamic DCNB, the charge is built up to a point where the field is strong enough to cause the cantilever to bend and touch the plate. As a dynamic DCNB, the intrinsic efficiency is 50 %, meaning that half of the energy is lost as heat and half is stored as potential energy in the electric field. The intrinsic efficiency does not include transport efficiency of the particles out of the coating (η_{tr}), nor does it include the efficiency of the transducer once a discharge is initiated ($\eta_{discharge}$), as well as other factors shown in Eq. (3.52) (i.e., the energy distribution of the particles (η_{ED}), the effect of the angular distribution of the particles being emitted ($\eta_m\eta_f$), electron backscatter (η_{BS}), and electron emission (η_{EM})). Figure 3.23 shows the idealized effect of the angular distribution of the particles being emitted having a peak efficiency of approximately 13.5 %. Due to the 50 % intrinsic efficiency of a dynamic DCNB, the idealized efficiency of a reciprocating cantilever is 6.75 %* ($\eta_{tr} \, \eta_{ED} \, \eta_{BS} \, \eta_{EM} \, \eta_{discharge.}$) (Fig. 3.24).
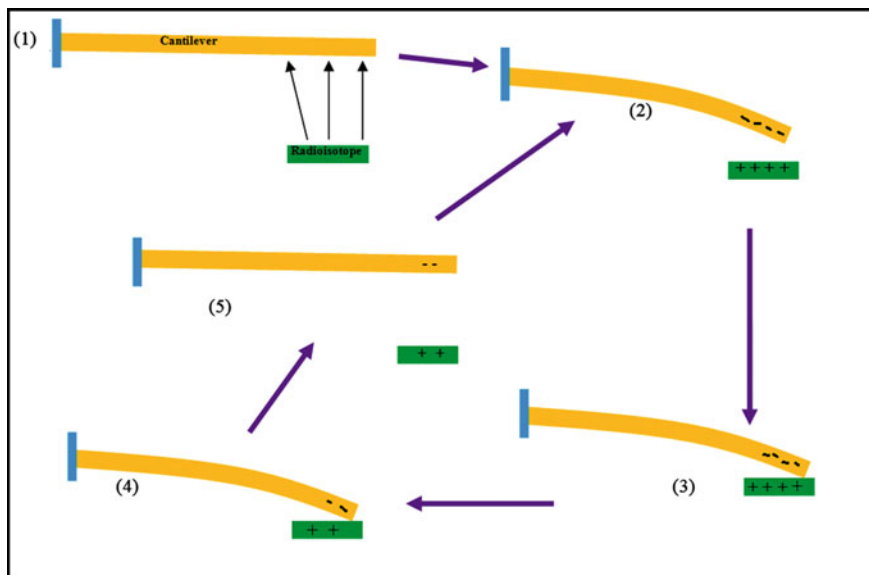
Fig. 3.24 Illustration of a self-cantilever system: *1* Electrons emitted from the beta source are collected on the cantilever. *2* Positive charges on the cantilever are due to charge transfer. The electrostatic force pulls the cantilever towards the beta source. *3* Cantilever gets in contact with source and charges are neutralized. *4* After charge neutralization, there is not enough attractive force to keep the cantilever in contact with the radioisotope. *5* The spring force retracts the cantilever to its original position and a new cycle begins

3.2.4   Indirect

NASA has successfully used thermionics with the Radioisotope Thermal Generator (RTG) systems in a number of missions (e.g., Apollo-SNAP-27 generators, Voyager, and Cassini). The energy resulting from the decay of radioisotopes starts out as very high-grade energy: multi-MeV, heavy, and highly charged particles. However, in the usual embodiment of radioisotope fuel in the RTG, as a solid, the charged particles are absorbed in a very short distance (micrometers) and thermalized to moderate temperatures (in the range of 600 K). At this temperature, the energy would be considered of significantly "lower grade," because the efficiency of the subsequent thermal energy conversion process is low. This latter process converts the heat into a more usable high-grade form of energy, such as electricity.

Thermoelectric generation of electricity using the Seebeck (thermocouple) effect has worked successfully in a number of power packages for satellites. Thermionic production of electricity directly inside reactor cores is again being pursued for space power applications.

In contrast, fluorescence produced from the interaction of charged particles from the radioactive decay of radioactive isotopes with a flourescer medium has been used to produce low intensity lights for remote applications, such as runway lights.

These devices involve relatively low power output. The fluorescence production process has some advantages which can be exploited by nuclear battery technology. Fluorescence can be transported away from the radiation source to a shielded transducer. This indirect photon based process involves a two-step method for converting the energy of the charged particles from nuclear reactions into a usable energy form such as electricity, chemicals, or coherent light. In the first step, the ions produced by nuclear reactions transfer their energy to an intermediate photon generator—a fluorescer medium. This step in the process uses a nuclear-driven fluorescer or NDF (a medium which produces incoherent narrow-band electro-magnetic radiation). In the second step of the process, the intermediate photons from the nuclear-driven fluorescer are absorbed by a material, which converts the photons into a useful high-grade energy form. The medium which converts the fluorescence into a useful product is called the transducer. The fluorescer can be in the form of a solid, a liquid or a gas. The transducer can be of many types depending on the desired product. Examples include: A photovoltaic cell for the production of electricity; a chemical medium that is photolytically transformed to a useful chemical (e.g., hydrogen); or a laser gain medium which produces laser light.

3.2.4.1 Gaseous Fluorescers

Gaseous fluorescers have been extensively studied as lighting sources. Examples of these include fluorescent lights which use a mercury vapor discharge to generate 254 nm light. The 254 nm light output interacts with phosphors to produce the visible spectrum that is used for lighting. Other examples include sodium lamps which use sodium vapor to generate the yellowish light emitted by street lamps. These two example fluorescent light sources are limited by self-absorption because they depend upon line emission.

PIDEC and RECS

In gases, the energy goes into ionization and excitation. In typical gas mixtures, the ionization and excitation produces excited states in the atoms or molecules that make up the gas. For low power density, the bulk of the excitations will occur in neutral atoms and molecules. The line emission will be dispersed over a broad range of the spectra from the ultraviolet to the infrared. Optical emitters based on line emission are subject to self-absorption and will only be optically thin over a limited size and pressure. The efficiency of a specific line with a narrow frequency is typically less than 1 %, which is generally the theoretical limitation of a single line (with few exceptions). One such exception is mercury, which can have high efficiencies at very low power density and low pressure (up to 70 %). Another exception is sodium which can have high efficiencies at low power density and low pressure (up to 40 %). Both mercury and sodium are not acceptable for use in a nuclear battery for several reasons. The low power density requirement means that

the size of the fluorescer would have to be very large in order to get a reasonable power output. Secondly, the efficiency of the light source would decrease as the size of the lamp increases due to the self-absorption effects of line emitters (meaning the lower energy state of the emitter is sufficiently dense as to absorb photons created by the spontaneous emission of an upper state). Mercury and sodium lamps are useful for fluorescer bulbs or street lights, respectively, because these lamps are scaled to a relatively small size with a low power density to avoid self-absorption, thus they are optically thin. As the lamp scales, it becomes optically thick and loses its efficiency.

Spectral Considerations for Excimer Emitters

The term excimer is short for excited dimers. A dimer is a short lived dimeric or heterodimeric molecule formed by two atoms, where at least one of the atoms has a completely filled valence shell (such as a rare gas). For example, rare gases can't form molecules in the ground state, but can form a molecule in an electronic excited state. Examples of excimer molecules include the rare gas excimers Ar_2* (where the "*" indicates an excited state), Kr_2* and Xe_2*, the rare gas-halide excimers ArF*, KrF*, XeF*, ArCl*, KrCl*, XeCl*, etc. and a number of other excimer gas combinations [40]. When an excimer molecule decays by spontaneous emission, a photon is given off by the bound excited molecular state to an unbound state where the atoms making up the molecule become neutral and independent. In an excimer gas mixture (a mixture of gases that form the excimer state), both ionization and excitation contribute to the formation of the excimer states (with about 50 % efficiency for photon production for rare gas excimers). Excimers thus depend upon the formation of ions and metastable states by the interaction of ionizing radiation with a gas. In an excimer forming gas, if the pressure of the gas is high enough (usually greater than a half atmosphere), the formation of excimers is favored over formation of atomic excited states (atomic excited states lead to undesirable line emissions from the atom). Excimers emit in a very narrow wavelength range (±10 nm). Additionally, excimers do not have a bound ground state and thus are not subject to self-absorption. Thus, excimer gas mixtures remain optically thin (meaning no self-absorption) over large size, large power density, and high pressure.

If the excimer is a rare gas excimer, like the xenon excimer, the bulk of the energy that goes into the formation of xenon ions and xenon metastable states proceeds into the formation of the xenon excimer state. From Table 3.9, it takes 21.9 eV to form an ion pair. The W* value for xenon metastable state formation (42 eV per metastable state) is also known [40]. The theoretical maximum efficiency for xenon excimer production (η_f) is the ratio of the xenon excimer photon energy (7.2 eV) divided by the W value for ion pair production plus the ratio of the xenon photon energy divided by the W* value for Xe metastable production shown in Eq. (3.69).

$$\eta_f \cong \frac{7.2}{21.9} + \frac{7.2}{42} = 0.5 \tag{3.69}$$

Thus the theoretical maximum efficiency of an energy conversion method using xenon excimer formation is about 50 %. This value of 50 % is approximately correct for all rare gas excimers.

Experimental measurements of excimer fluorescence efficiency are difficult due to the fact that typical research used high flux nuclear reactors as the power source to generate reasonable power densities in the excimer gas. One example is the calibrated measurement of the excimer fluorescence efficiency from xenon gas [41]. The goal of this experiment was to measure vacuum ultra violet (VUV) fluorescence production efficiencies from a nuclear-pumped xenon excimer system. The experiment was conducted using the F beam port of the University of Missouri Research Reactor (also known as MURR) as a source of neutrons to pump the $B^{10}(n, \alpha)Li^7$ reaction. Several constraints had to be considered: (1) a vacuum was required along the light path for the VUV radiation produced by excimer gas; (2) the detector needed to be shielded from the radiation emitted from port opening so a turning mirror was necessary; and (3) the production of activation products had to be minimized. The constraints led to the experimental design shown in Fig. 3.25. The use of the F beam port posed an interesting design problem. Primarily, the limited space of the port (1.2 in. inner diameter) presented the most significant challenge. Additionally, it was

Experimental Set up for the Excimer Efficiency Measurement
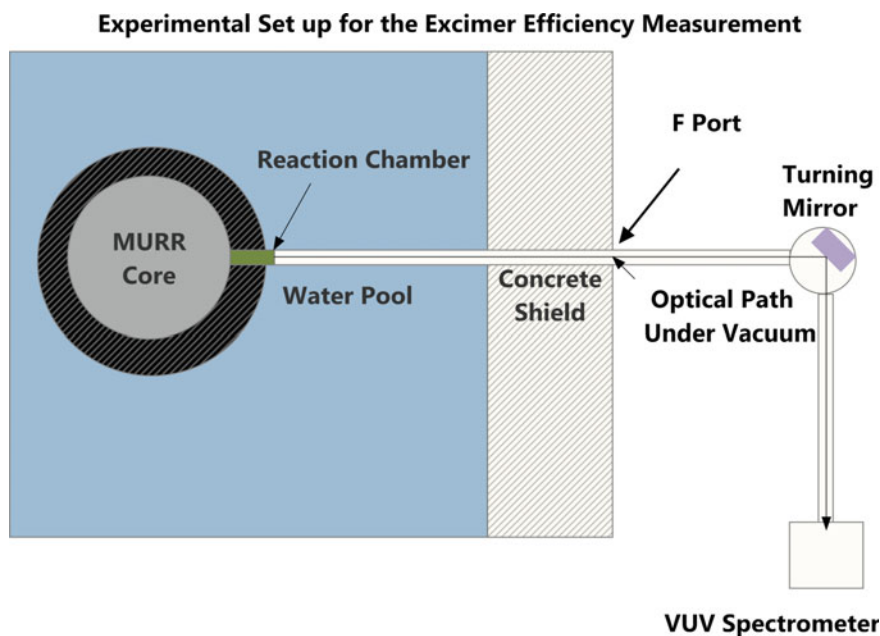
Fig. 3.25 Experimental position in the F beam port in the MURR reflector

necessary to measure the neutron flux distribution along the length of the active area of the port since this data was not known.

The flux was measured by using a hollow 6061 aluminum alloy tube. A rod with a very thin research grade gold wire wrapped around it was placed in the hollow aluminum tube. Additionally, a copper-constantine thermocouple wire was mounted at both ends and in the middle of the hollow tube. The thermocouple was used to measure the temperature profile of the hollow tube.

The hollow aluminum alloy tube was placed in the active area of the assembly and the optical light path tube and the reaction chamber assembly was vacuum tested before being set in beam port F. A pump down procedure was developed where the beam port tube was evacuated and filled with He. The optical path was vacuum checked. The reactor was then brought up to a power level of 500 kW. The temperature was measured and a profile indicating a gradient from the reaction chamber nearest the reactor to the opposite end of 50°F was recorded (T = 130 °F to T = 80.0 °F). The reactor power level was monitored as well as the exposure time during the run. After the run, the gold wire was taken out and cut up into pieces—0.5 cm long and the position of each piece in the reaction chamber was recorded. Each piece was analyzed for the amount of the gold isotope with an atomic mass of 198 (created by the thermal neutron activation reaction, $Au^{197}(n_{thermal}, \gamma)Au^{198}$). The amount of Au^{198} is proportional to thermal neutron flux. So the with the measured amount of Au^{198} in each piece of wire, the thermal neutron flux profile was found.

The optical system's major components were the reaction chamber, the vacuum tight optical path, and the turning mirror assembly. Of the major components, the reaction chamber and the turning mirror assembly were the most difficult to design.

Given the limited space of the beam port tube, a unique method of filling a reaction chamber with a sample gas had to be developed. This step was accomplished by using a multiple seal on the end cap (see Fig. 3.26).

It was also necessary to develop a turning mirror assembly which could be moved in the X-Y-Z direction and which maintained vacuum integrity. This task was accomplished by using a bellows mount and a rotational feed through (see Fig. 3.27).

The optical system required a preliminary test. An experiment was designed and performed that used helium gas which has no possible activation products. In order to calibrate an optical system, either a calibrated light source or a calibrated detector is required. In this experiment, a calibrated Sampson type UV lamp was used to calibrate the optical system. An additional experiment was run to find the time it would take to measure a reasonably high resolution spectra from helium using a strip chart recorder (note that a motor was used to move the grating in the Acton vacuum ultra violet spectrometer). From this experiment, it was determined that a spectra could be successfully taken within a 3 min period. The helium spectra that was taken matched up very well with a helium spectra taken in previous work [42]. Of the excimer fluorescers, xenon has the most hazardous activation products. These products include Xe^{125} and Xe^{133m}. The activation products accumulated
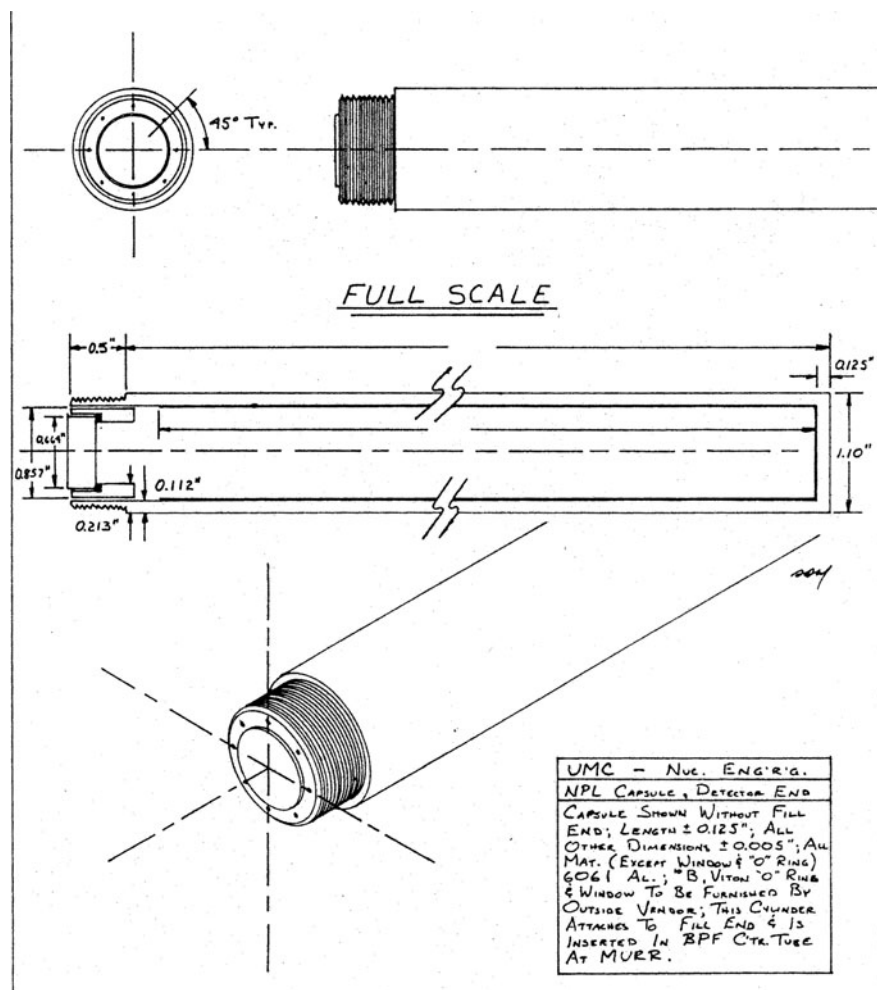
**Fig. 3.26** Reaction chamber used for fluorescence experiments

during a 5 min run, if released, were found to be within the reactor's maximum permissible concentration limits.

The xenon excimer experimental was run using 1 atm sample of Xe The efficiency for the production of xenon excimer fluorescence at 172 nm was measured and found to be 49 ± 10 %. This agrees well with the theoretical efficiency of 50 %. In general the nuclear-pumped excimer systems appear to operate very close to their theoretical maximum efficiency [40]. It should also be noted that under no circumstance should the excimer efficiency exceed the theoretical maximum efficiency.
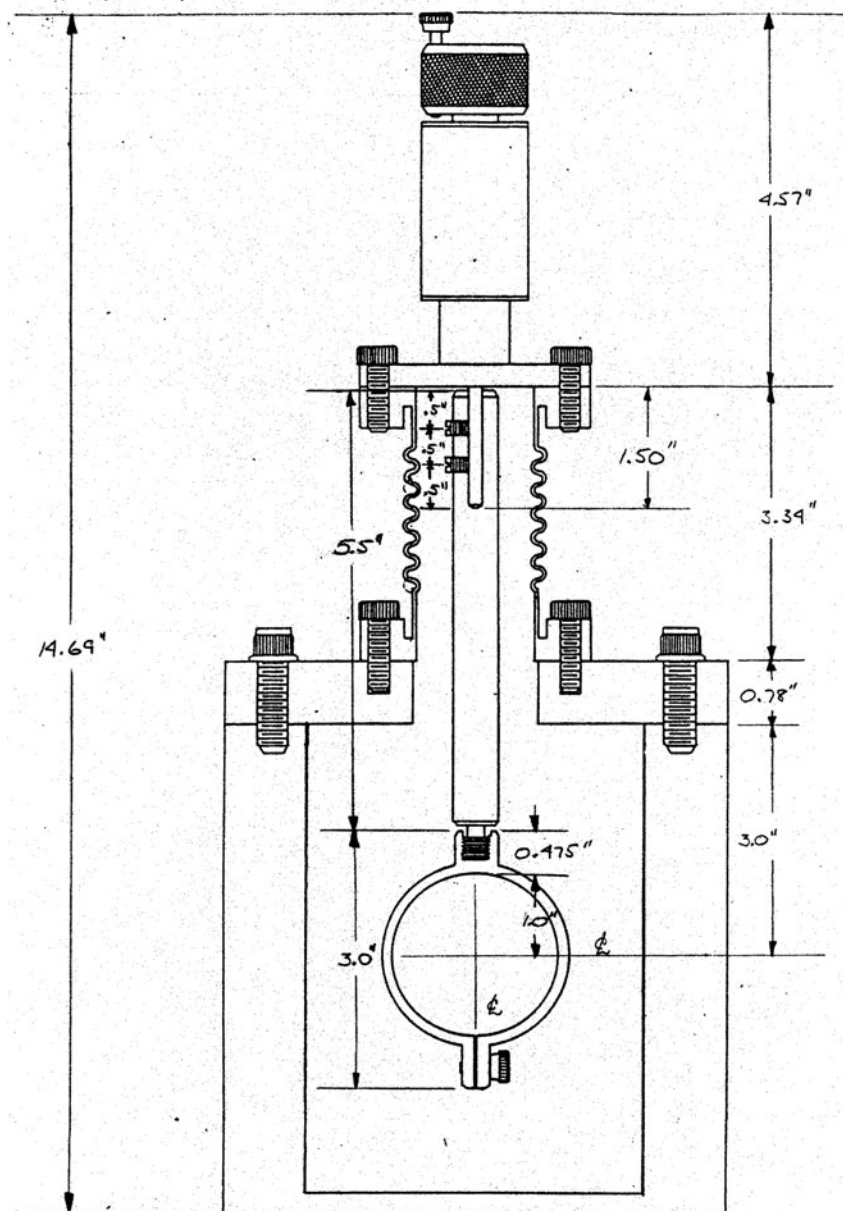
**Fig. 3.27** Diagram of the vacuum ultra violet turning mirror assembly

Fig. 3.28 Energy structure of
the xenon molecule [44]
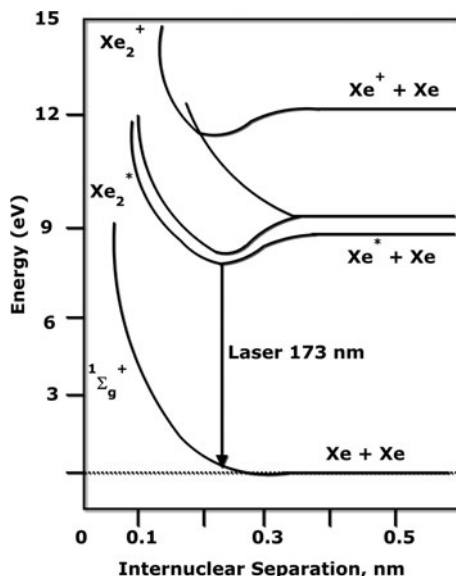
Effect of Impurities on Excimer Efficiency

Impurities will cause parasitic reactions which take energy away from the excimer
channel. The dominant reactions in forming the xenon excimer (Fig. 3.28) are 1, 7,
11, 13, 14, 22 and 36 from Table 3.10 [43].

Experimental data matches well with the model, as shown in Fig. 3.29. There are
parasitic reactions due to impurities which can channel energy away from the Xe^*
and Xe^+ states. These are:

$$Xe^* + M \rightarrow Xe + M^*(or\, M^+) \tag{3.70}$$
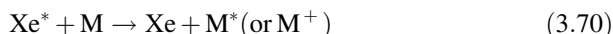
where M is the impurity atom or molecule, M* is the excited state of the impurity
atom or molecule and M^+ is the ionized state of the impurity atom or molecule.

$$Xe^+ + M \rightarrow Xe + M^+ \tag{3.71}$$

Even research grade purity rare gases have some impurity content, as shown in
Table 3.11. For example, if a chamber were filled with one atmosphere of xenon,
there are 2.44×10^{19} xenon atoms-cm^{-3}. One part per million of an impurity will
represent 2.44×10^{13} impurity atoms or molecules-cm^{-3}. These impurities will
siphon energy from the desired reactions that form excimers. A kinetic study
performed by one of the authors indicates that when impurities are at the ppm level,
the energy siphoned away from excimer formation can be significant when the
pumping power density is below 1 mW-cm^{-3}. As the power density increases, the
siphoning effect of the impurity "burns out" and the percentage of energy siphoned
away from excimer formation decreases. The "burn out" effect is due to slower

Table 3.10 Reactions used in the Xe model [43]

No.	Reaction	Rate constant (s^{-1}, cm^{-3} s^{-1}, or cm^{-6} s^{-1})
1	$Xe^* + 2Xe \rightarrow Xe_2^*(1\Sigma) + Xe$	1.7×10^{-32}
2	$Xe^{**} + Xe \rightarrow Xe^* + Xe$	1.0×10^{-10}
3	$Xe^* + Xe \rightarrow Xe + Xe$	3.5×10^{-15}
4	$Xe^{**} + 2Xe \rightarrow Xe_2^{**} + Xe$	1.0×10^{-31}
5	$Xe_2^{**} + Xe \rightarrow Xe^* + 2Xe$	1.0×10^{-11}
6	$Xe_2^*(1\Sigma) + Xe \rightarrow Xe_2^*(3\Sigma) + Xe$	1.2×10^{-13}
7	$Xe^* + Xe^* \rightarrow Xe^+ + Xe + e$	2.0×10^{-9}
8	$Xe_2^*(1\Sigma) + Xe_2^*(1\Sigma) \rightarrow Xe_2^+ + 2Xe + e$	5.0×10^{-10}
9	$Xe^+ + 2Xe \rightarrow Xe_2^+ + Xe$	2.5×10^{-31}
10	$Xe_2^+ + e \rightarrow Xe^{**} + Xe$	2.3×10^{-7}
11	$Xe_2^*(1\Sigma) \rightarrow 2Xe + hv$	2.1×10^{-8}
12	$Xe^{**} \rightarrow Xe^* + hv$	1.5×10^{-7}
13	$Xe_2^*(3\Sigma) + e \rightarrow Xe_2^*(1\Sigma) + e$	1.8×10^{-7}
14	$Xe_2^*(1\Sigma) + e \rightarrow Xe_2^*(3\Sigma) + e$	4.9×10^{-7}
15	$Xe_2^{**} + e \rightarrow Xe_2^*(3\Sigma) + e$	5.0×10^{-7}
16	$Xe_2^{**} + e \rightarrow Xe_2^*(1\Sigma) + e$	2.0×10^{-7}
17	$Xe_2^*(1\Sigma) + e \rightarrow 2Xe + e$	1.3×10^{-9}
18	$Xe_2^+ + e \rightarrow Xe^* + Xe$	2.3×10^{-7}
19	$Xe^* + 2Xe \rightarrow Xe_2^*(3\Sigma) + Xe$	4.4×10^{-32}
20	$Xe_2^*(3\Sigma) + Xe_2^*(3\Sigma) \rightarrow Xe_2^+ + 2Xe + e$	5.0×10^{-10}
21	$Xe_2^*(3\Sigma) + Xe_2^*(1\Sigma) \rightarrow Xe_2^+ + 2Xe + e$	5.0×10^{-10}
22	$Xe_2^*(3\Sigma) \rightarrow 2Xe + hv$	1.0×10^{-7}
23	$Xe_2^*(3\Sigma) + e \rightarrow 2Xe + e$	1.3×10^{-9}
24	$Xe^+ + Xe + e \rightarrow Xe^* + Xe$	1.0×10^{-26}
25	$Xe_2^+ + e + Xe \rightarrow Xe_2^*(1\Sigma) + Xe$	1.0×10^{-26}
26	$Xe_2^*(1\Sigma) + e \rightarrow Xe_2^+ + 2e$	5.00×10^{-9}
27	$Xe_2^*(3\Sigma) + e \rightarrow Xe_2^+ + 2e$	5.0×10^{-9}
28	$Xe_2^+ + e + Xe \rightarrow Xe_2^*(3\Sigma) + Xe$	1.0×10^{-26}
29	$Xe^{**} + Xe \rightarrow Xe + Xe$	1.0×10^{-15}
30	$Xe_2^*(3\Sigma) + Xe \rightarrow Xe_2^*(1\Sigma) + Xe$	4.6×10^{-15}
31	$Xe^{**} + e \rightarrow Xe^* + e$	8.0×10^{-7}
32	$Xe_2^*(3\Sigma) + e \rightarrow Xe_2^{**} + e$	3.0×10^{-7}
33	$Xe^{**} + Xe^{**} \rightarrow Xe^+ + Xe + e$	5.0×10^{-10}
34	$Xe_2^{**} + Xe_2^{**} \rightarrow Xe_2^+ + 2Xe + e$	5.0×10^{-10}
35	$Xe^* + e \rightarrow Xe + e$	1.0×10^{-9}
36	$Xe^+ + 2e \rightarrow Xe^* + e$	1.0×10^{-20}
37	$Xe_2^{**} \rightarrow Xe^* + Xe + hv$	1.0×10^{-8}

QUANTUM EFFICIENCY VS. POWER
DENSITY
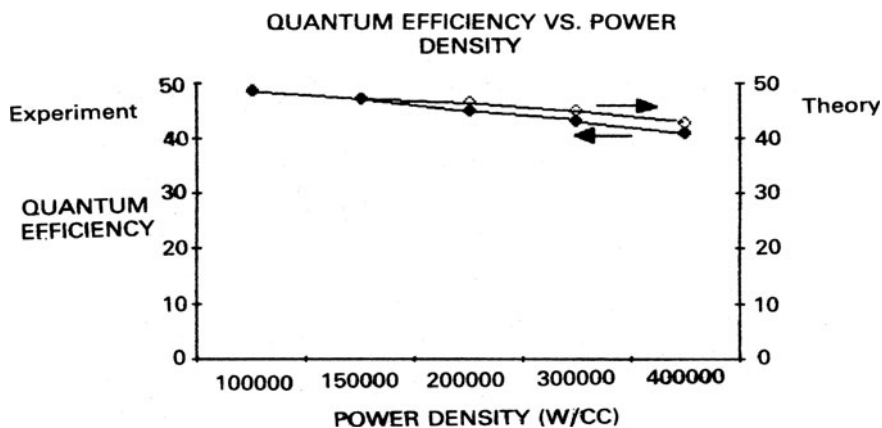
Fig. 3.29 Comparison of theoretical and experimental data for e-beam driven Xe_2* fluorescence efficiency at 3 atm. of Xe

**Table 3.11** The impurities in research grade xenon gas (99.999 % pure) are shown

Contaminant	Research Grade Xenon, 99.999 % pure (ppm)
Ar	1.0
CO_2	1.0
CF_4	0.5
H_2	2.0
Kr	5.0
N_2	2.0
O_2	0.5
Total hydrocarbons	0.5
H_2O	0.5

reaction rates that occur once an impurity ion is formed (like recombination or further excitation). At power densities above 1 W-cm^{-3} the bulk of the energy forms excimers. Thus, excimers lose efficiency due to siphoning at power densities below 1 W-cm^{-3} because of interactions between rare gas metastable states or ion states with low level impurities. However, at power densities above 1 W-cm^{-3}, excimers approach the theoretical maximum efficiencies of the gas because the impurity ground states are depleted rapidly.

PIDEC

The pursuit of the production of electrical power from a nuclear light bulb was suggested by one of the authors in 1981 [45]. The nuclear light bulb was based on the Photon-Intermediate Direct Energy Conversion (PIDEC) process shown in
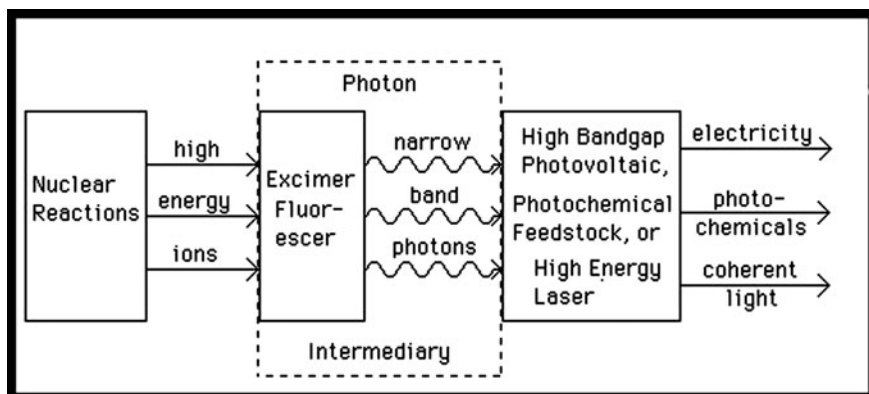
Fig. 3.30 Schematic diagram of the Photon-Intermediate Direct Energy Conversion (PIDEC) process

Fig. 3.30, and was conceived as a method of energy conversion for a variety of nuclear reactions including fission, advanced fuel fusion and radioisotope decay [45–47]. Advanced-fuel high temperature fusion, however, will not be available in the foreseeable future. Potential sources of ions from fission reactions and radioisotopes however, are viable near term energy sources. The nuclear-driven fluorescer concept, which was initially suggested as a photolytic driver for a nuclear-pumped laser in 1977 by the author, his fellow students and his mentor George Miley, was the fundamental component of the nuclear light bulb [48]. This concept makes feasible efficient ion-driven photon sources by removing the nuclear source material from the solid, where it prevented transmission of the photons, and moving it to the volume of the fluorescer gas by one of four methods; a gaseous source, a source embedded in thin films of arbitrary shape and size or as an aerosol source (Fig. 3.31) [40]. A critical component of the nuclear light bulb is that the scale lengths of the solid sources are chosen small enough so that most of the particulate energy escapes into the surrounding gas, creating a weak plasma which produces photons. The coexistence of weak plasma with an aerosol introduces a unique set of problems. Another critical aspect of the nuclear light bulb is that the combination of the photon producing weak plasma and the aerosol source or thin film source remains optically thin to allow the photons to transport out of the system. As will be discussed, the nuclear light bulb can be made optically thin. The nuclear light bulb in conjunction with radioisotopes led to the development of the Radioisotope Energy Conversion System (RECS) [49], Fig. 3.32.

RECS utilizes a two-step method for directly converting the energy of the charged particles from nuclear reactions into a usable energy form such as electricity, chemicals, or coherent light. In the first step the ions produced by nuclear reactions transfer their energy to an intermediate photon generator—a fluorescer medium. This portion of the RECS comprises what is called the nuclear-driven
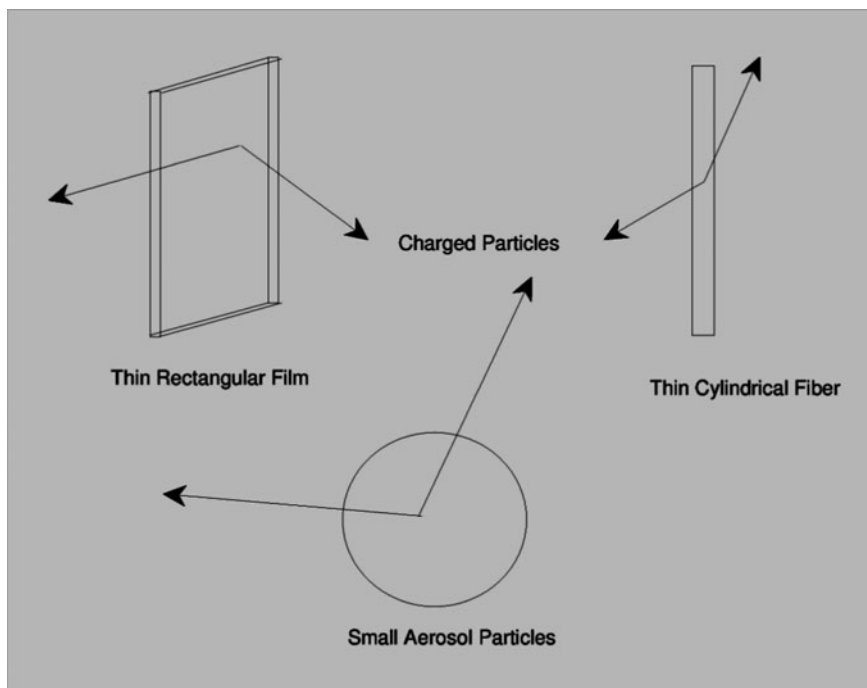
Fig. 3.31 An illustration of the use of *thin solid* geometries which allow reaction products to escape the solid matrix into a surrounding gas

fluorescer or NDF (a medium which produces incoherent narrow-band electromagnetic radiation). In the second step, the intermediate photons from the nuclear-driven fluorescer are absorbed by a material, which converts the photons into a useful high-grade energy form. This portion of the RECS is the photon energy converter.

The efficiency of the two-step PIDEC process, used for the RECS has two major advantages over thermal energy conversion, which is a many step process. These advantages are: (1) that it is a direct process producing a high grade photon source from a high grade ion source, thus avoiding the Carnot cycle efficiency limits imposed by thermalization and (2) that it is mechanically simple, potentially leading to more compact, more reliable, and less expensive systems.

The advantage of the two step process over a one-step direct energy conversion process is that of feasibility. The scale length for the transport of the primary high-grade ion source must match the geometrical scale of the energy converter. Energetic ions have a transport length of micrometers while useful energy converters, on the other hand, have a scale length of fractions of meters. For this reason, direct conversion of nuclear energy has not previously been possible. What was required (and provided by the nuclear light bulb concept) was an intermediate high-level energy converter that can be intermingled with nuclear material on a
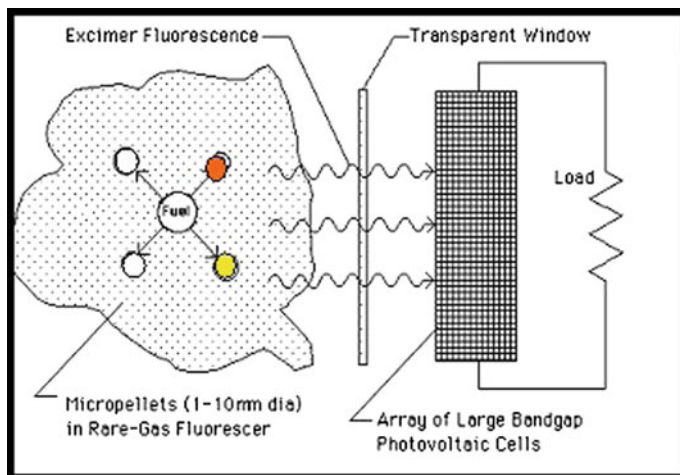
Fig. 3.32 Schematic diagram of the Radioisotope Energy Conversion System (RECS) which uses the radioisotope in aerosol form

micrometer scale-length, but produces an energy form that can be transported to meter scale-length direct converters producing useful output—a sort of "impedance matching" for the scale length of energy forms. With PIDEC that scale length matching medium is a fluorescing gas, the nuclear-driven fluorescer. The photons it produces can be transported great distances, making it possible to couple them to various energy conversion processes. Also, some conversion processes require greater power densities than the primary energy sources can provide. PIDEC can effectively implement optical concentrators, enabling achievement of the high threshold power density required for a conversion process such as a photolytic laser.

The RECS concept of high efficiency production of light from radioisotopes coupled to wide band-gap photovoltaic cells makes the nuclear light bulb especially useful for compact power supply applications.

Nuclear-Driven Fluorescers

Nuclear Driven Fluorescers (NDF) are photon producing media which directly use the energy from ionizing radiation. Scintillator materials, for example, constitute a medium which generates fluorescence. The reader may find references in the literature of the Former Soviet Union which refers to NDF media as scintillators [50]. Fluorescer media can be solids, liquids and gases [40].

The Ion Source

As shown in Fig. 3.32, one type of ion source can come from the decay of radioisotopes dispersed within a fluorescer gas. Effective dispersal is essential so that the ions produced by the isotope decay deposit most of their kinetic energy in the excimer gas rather than in the radioisotope material. There are several methods of achieving the desired dispersal: gaseous radioisotopes [46], radioisotopes embedded in thin films [51], microscopic aerosol of radioisotopes [47, 52, 53], or the atom embedded in a C60 cage [54]. The efficiency of transport of the ion energy from the radioisotope to the fluorescer medium varies with the scale length of the thin film or aerosol (or in the case of a gaseous radioisotope the transport distance of the particulate radiation in the gas), the chemical form of the radioisotope, and the uniformity of the radioisotope density. The variation of ion energy transport efficiency from a microsphere to the fluorescer medium with thin films and microspheres is discussed in the work of Chung and Prelas [51]. Energy transport efficiencies are about 60–70 % for reasonably designed thin films and 70–80 % for reasonably designed microspheres. The average atomic density in the medium must be on the order of 1×10^{19} particles cm^{-3}, enough to achieve reasonable power densities but not so great as to significantly degrade the transport of the fluorescence through the aerosol. Combining the constraints of efficiency and optical transparency determines scale length of the thin film or microspheres, as well as the number density. For example, a microsphere diameter of 5 μm and number density of 1×10^{6} cm^{-3}, which should not create significant absorption of the fluorescence [53, 55], results in a fuel density of 0.63 mg cm^{-3}, quite reasonable dimensions, and a good average number density (3.9×10^{19} atoms cm^{-3}) of the radioisotope. It is also possible to enhance the average number density by coating the aerosol particles with a thin reflective optical material. An alternative, which couples essentially 100 % of the ion energy to the fluorescer medium, is a gaseous radioisotope such as Kr-85 [9, 10].

Excimer Fluorescers

Excimer fluorescers are the most efficient optical radiators known and, because of their unbound lower levels, do not self-absorb. They radiate in a single, relatively narrow, band of wavelengths and are suitable for efficient photovoltaic energy conversion. The intrinsic fluorescence efficiencies of rare-gas and rare-gas halide excimers, based on standard W-value theory, are listed in column 2 of Table 3.12. Achievable efficiencies should be near the intrinsic values at the power and electron densities characteristic of nuclear reactions.

When combined with photovoltaic cells as the transducer, the combination of excimer fluorescence and PV cells can have high intrinsic efficiencies. This is shown in Table 3.13.

Experimental data on a number of excimer fluorescers show that the efficiencies match W-value theory. In fact, one group has reported measuring a nuclear-driven rare-gas excimer fluorescence efficiency higher than that predicted by W-value

Table 3.12 Excimer fluorescence efficiencies

Excimer	λ (nm)	η_{max}	Excimer	λ (nm)	η_{max}
NeF*	108	0.43	I$_2$	343	0.24
Ar$_2$	129	0.50	XeF*	346	0.24
Kr$_2$	147	0.47	Kr$_2$F*	415	0.17
F$_2$	158	0.44	Na$_2$*	437	0.46
Xe$_2$	172	0.48	HgI*	443	0.19
ArCl*	175	0.48	Li$_2$*	459	0.42
KrI*	185	0.37	Hg$_2$*	480	0.21
ArF*	193	0.35	HgBr*	502	0.17
KrBr*	206	0.33	KrO*	547	0.15
KrCl*	222	0.31	XeO*	547	0.15
KrF*	249	0.28	HgCl*	558	0.15
XeI*	253	0.37	K$_2$*	575	0.42
Cl$_2$	258	0.32	Rb$_2$*	605	0.41
XeBr*	282	0.29	CdI*	655	0.13
Br$_2$	290	0.29	Cs$_2$*	713	0.37
XeCl*	308	0.27	CdBr*	811	0.10

Table 3.13 Efficiencies for selected rare-gas and rare-gas halide excimer fluorescers (η_f) with well-matched wide-band-gap photovoltaic materials

Excimer	η_f	E_λ (eV)	Photovoltaic material	Band-gap energy (eV)	$\eta_{pv} = E_g/E_\lambda$	$\eta_{ie} = \eta_{pv} \times \eta_f$
Ar$_2$*	0.5	9.6	AlN	6.2	0.645	0.324
Kr$_2$*	0.47	8.4	AlN	6.2	0.789	0.345
	0.47	8.4	Diamond	5.5	0.655	0.308
Xe$_2$*	0.48	7.2	AlN	6.2	0.861	0.413
	0.48	7.2	Diamond	5.5	0.764	0.367
ArF*	0.35	6.4	AlN	6.2	0.969	0.339
	0.35	6.4	Diamond	5.5	0.859	0.301
KrBr*	0.33	6	Diamond	5.5	0.917	0.302
KrCl*	0.31	5.6	Diamond	5.5	0.982	0.304
Na$_2$*	0.46	2.84	ZnSe	2.7	0.951	0.437
	0.46	2.84	SiC	2.4	0.845	0.389
Li$_2$*	0.42	2.7	CuAlSe$_2$	2.6	0.963	0.404
	0.42	2.7	SiC	2.4	0.889	0.373

The theoretical maximum intrinsic efficiency for the match of the given excimer spectra to the PV cell band-gap (or maximum value for η_{in}) is η_{pv}, and the ion-to-electric efficiency, η_{ie}
E_λ (eV) is the average photon energy E_g is band-gap energy of the photovoltaic material

theory at 68 % [56]. However, this is clearly an outlier. All of the other experiments with a variety of excitation sources (e.g. electrons, fission fragments, protons) and particle densities have given fluorescence efficiency values near the theoretical limits predicted by W-value theory [40]. The most efficient excimer fluorescers are the rare-gas excimers.

The Photon Energy Converter

The key to the feasibility of the RECS is the photovoltaic Photon Energy Converter. The common impression of photovoltaics is that they cannot be very efficient. This misunderstanding comes from the fact that photovoltaics are most commonly employed as "solar cells." Solar cells are not very efficient, ranging from 10–20 % for commercial units and reaching as high as about 25 % for laboratory cells. However, the low efficiency is more due to the characteristics of the solar spectrum than to the photovoltaic devices themselves, especially for the laboratory units with efficiencies of ~ 25 %. The problem with the solar spectrum is that it is very broadband—its ratio of the average photon energy to the width (FWHM) of the spectrum ($E_{mean}/\Delta E$) is about 1. This is good for color vision but quite bad for efficient energy conversion. For excimers, however, this ratio is greater than 10. Under these conditions photovoltaics have intrinsic efficiencies of 75–95 %.

Photovoltaic cells for use in photon-intermediate direct energy conversion of electricity will require the development of a doped semiconductor material with a band-gap that matches the UV radiation. With wide band-gap photovoltaic cells, fusion ion driven fluorescence in a PIDEC system was studied [45, 57]. Fission ion driven fluorescence sources in a PIDEC system were studied as well [58].

Photovoltaic Conversion of Narrowband Fluorescence

For a given spectrum, the efficiency of conversion is basically determined by the variation of the irradiance with photon energy and by the substrate band-gap energy, E_g, of the photovoltaic converter. Complete conversion (100 %) is not possible because of the width of the solar spectrum. This leads to two competing effects on the efficiency. The first effect is that the energy of all photons with quantum energy $hv < E_g$ is lost because they do not have sufficient energy to excite electrons from the valence band to the conduction band. The power density lost in this case is given by

$$P_{lost} = \int_0^{E_g} W(E)dE \qquad (3.72)$$

where $W(E)$ is the irradiance in W/cm^2-eV.

Thus, the lower the band-gap of the photovoltaic converter, the larger the fraction of the total spectrum converted. Competing with this effect however is the fact that, for the photons with quantum energy $hv > E_g$ that do contribute, the

IRRADIANCE (W/sq cm/eV)
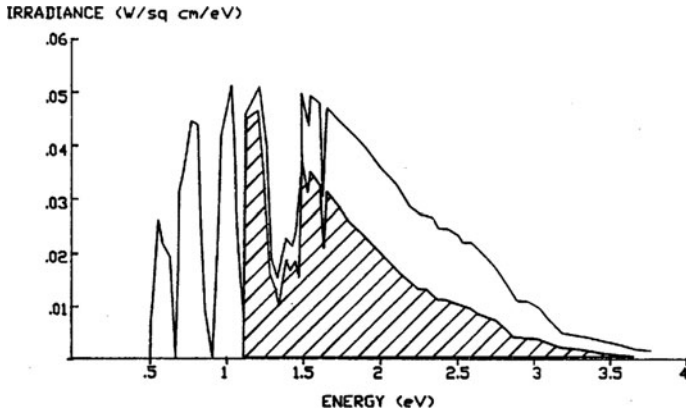
ENERGY (eV)

Fig. 3.33 Efficiency of photovoltaic conversion of broadband solar radiation using photovoltaics with $E_g = E_{min}$. Data points are fraction of total number of photons with an energy greater than E versus photon energy normalized to the average photon energy

Fig. 3.34 Efficiency of photovoltaic conversion of broadband solar radiation using Photovoltaics with $E_g = E_{av}$. Data points are fraction of total number of photons with an energy greater than E versus photon energy normalized to the average photon energy
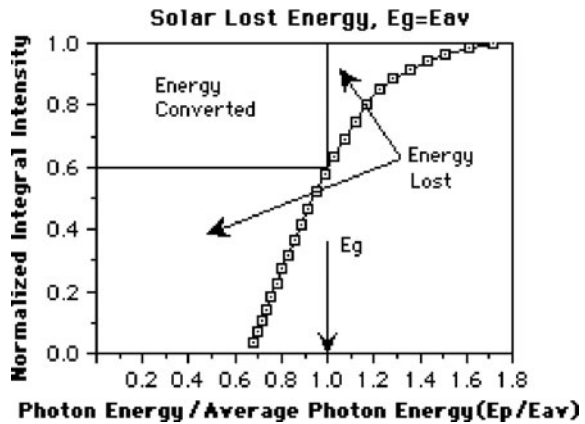
photon energy in excess of the band-gap energy is lost. Thus the maximum intrinsic efficiency for photovoltaic conversion, assuming an ideal collection device, is

$$\eta_{in} = \frac{\int_{E_g}^{\infty} W(E_i) \frac{E_g}{E_i} dE_i}{\int_{E_g}^{\infty} W(E_i) dE_i} \tag{3.73}$$

where E_i is the impact ionization energy.

These two effects are shown graphically in Figs. 3.33 and 3.34 for broadband (solar) and in Fig. 3.35 for narrowband (Xe$_2$*) radiation. In Figs. 3.33 and 3.34 it can be seen that for a broadband spectrum, such as the solar spectrum, there is no value of E_g that results in most of the energy being converted. In Fig. 3.35, on the

Fig. 3.35 Efficiency of photovoltaic conversion of narrowband excimer radiation using high bandgap photovoltaics. Data points are fraction of total number of photons with an energy greater than E versus photon energy normalized to the average photon energy
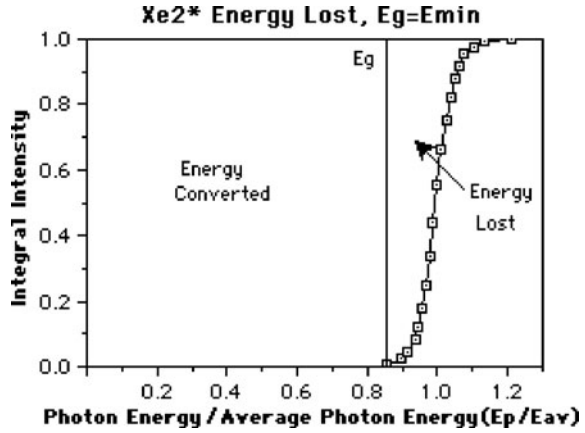
other hand, it can be seen that, for E_g just less than E_{min}, efficient energy conversion takes place.

Typically, the effect of the details of the solar radiation spectrum on calculating overall conversion efficiency is translated into a photon flux density, which then relates to an ideal short circuit current density. This is convenient because it is a good assumption that each photon absorbed and collected effectively causes one electron to move around the circuit. Also, after each electron thermalizes (gives off energy in excess of E_g to the lattice), it contributes the maximum energy amount E_g to the overall process.

This contribution is conveniently modeled in the photovoltaic device using the ideal Shockley model for the p-n junction. Using these concepts, the intrinsic conversion efficiency can be written in the following terms,

$$\eta_{in} = \frac{E_g \int_{E_g}^{\infty} N_{ph}(E)dE}{\int_{E_g}^{\infty} N_{ph}(E)EdE} = \frac{E_g N(E > E_g)}{E_{mean} N_{total}} = \frac{E_g \eta_{eg}}{E_{mean}} \tag{3.74}$$

where N_{ph} is the photon flux density in #/s-cm^2-eV, $N(E > E_g)$ is the photon flux in the interval $E > E_g$, N_{tot} is the total photon flux, and η_{eg} is the fraction of photons with $E > E_g$.

The solid lines in Figs. 3.36 and 3.37 show, respectively, the air mass 2 (AM2) irradiance of the solar spectrum (W/cm^2-eV) [11] and the irradiance for Xe$_2$*, a narrow-band fluorescer. For Xe$_2$*, $E_{mean}/\Delta E = 14$, compared to a corresponding value of 1.3 for the AM2 solar spectrum. For a narrow distribution one can have $E_g/E_{mean} \sim 1$ and still have $\eta_{EG} \sim 1$. A narrow-band spectra will consequently have the highest intrinsic efficiency. The crosshatched areas in Figs. 3.36 and 3.37 represent, respectively, the power density converted for the solar spectrum and for the Xe$_2$* spectrum. The ratio of the cross hatched area to the total area in both cases gives the intrinsic efficiency. The white area under each curve corresponds to
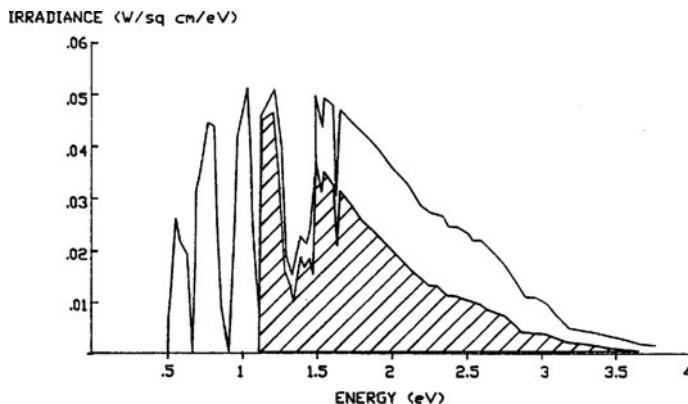
Fig. 3.36 The spectral irradiance of the solar spectrum (AM2). The cross hatched area under the curve is the fraction of energy which is usable with a 1.1 eV bandgap photovoltaic cell
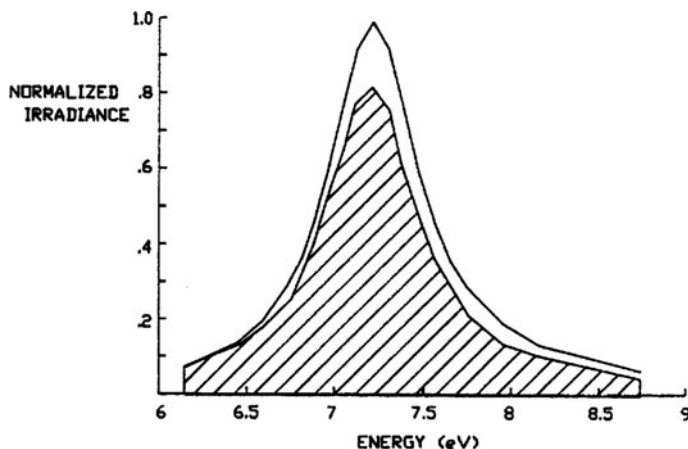

Fig. 3.37 The normalized irradiance of Xe_2* excimer source. The cross hatched area under the curve is the fraction of energy which is usable with a 6 eV bandgap photovoltaic cell

unconverted power. These figures illustrate that a large portion of the energy in a broad band source, such as a solar source, is wasted while a much smaller fraction of the energy in a narrow band source, Xe_2*, is wasted.

Figure 3.38 is a plot of maximum efficiencies for a p-n junction converter versus band-gap energy of the converter substrate material. Two plots are shown, one for an AM2 solar spectrum and one for a Xe_2^* spectrum. The previously derived equations were used to calculate these curves. Also shown are vertical lines representing the band-gap energies of the two materials theoretically predicted to maximally convert these two spectra. Lines representing Si and diamond are shown for comparison. The curve for the solar spectrum lies in between the two best

Fig. 3.38 The theoretical
maximum conversion
efficiency of photovoltaic
cells with various bandgap
energies using either a solar
spectrum or a Xe_2^* spectrum.
Band-gap energies associated
with Si, GaAs, diamond, and
AlN are shown
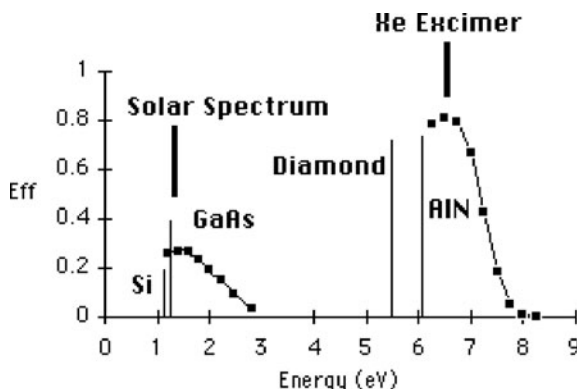
known curves of this type [40]. The approximately 30 % maximum is thought to be
an upper bound on the ability of a single material junction to convert the solar
spectrum. The highest known conversion efficiency for silicon, to date, has been
26 % obtained with a highly optimized MIS solar cell [40].

In contrast to the relatively low values for conversion of the solar spectrum, it
can be seen from Fig. 3.38 that efficiencies as high as 80 % can theoretically be
obtained using a p-n junction and converting the Xe_2^* spectrum. The efficiencies in
Fig. 3.38 assume a fill factor of 1. A fill factor of one is an optimistic assumption.
However, a fill factor of 0.8 is reasonable [59].

Wide Band-Gap Photovoltaic Materials

Table 3.14 lists several potential wide band-gap materials. One material, diamond
(5.4 eV), has recently received intense study as a microelectronic device substrate.
However, the most efficient excimer UV radiation sources, the rare-gas excimers,
have larger photon energies (>7 eV) and hence the development of higher band-gap
photocells for these excimers would be desirable. Table 3.13 matches the more
efficient and desirable fluorescers from Table 3.12 to materials with appropriate
band-gaps from Table 3.14. The theoretical maximum intrinsic photovoltaic effi-
ciency (the ratio of the band-gap to the mean photon energy) ranges from 75 to
95 %) while the corresponding theoretical maximum efficiency for conversion of
ion energy to electrical energy (the product of the photovoltaic efficiency and the
fluorescence efficiency) ranges from 30 to 45 %.

The outlook for wide band-gap photovoltaic cells is hopeful since p-n junctions
are available in some materials that are commercially available (e.g., SiC and GaN)
and p-n junctions have been made in these materials. Progress has also been made
in forming p-n junctions in other wide band-gap materials (e.g., diamond) [24].

It is possible to find flourescers that have photon energies that are lower than rare
gas excimers. For example, rare-gas halide excimers have lower photon energies
(3.5 eV for XeF*, 5.0 eV for KrF*, and 6.4 eV for ArF*) and, while their

Table 3.14 Band-gap energies for various semiconductors

Material	Band-Gap (eV)	Bandgap energy (eV)
Si	1.1	1685
CdSe	1.44	1370
ZnSe	2.26	1510
3C-SiC	2.36	3103
6H-SiC	3.05	3103
4H-SiC	3.21	3103
GaN	3.4	2770
ZnS	3.54	1920
UO$_2$	5.2	3150
Diamond	5.5	100*
AlN	6.02	2500

*Graphitization Temp

fluorescence efficiency may be lower than that of the rare-gas excimers, their photon energy falls in the range of commercially available p-n junctions in some semiconductor materials (Table 3.15).

PIDEC is an indirect energy conversion scheme which uses high efficiency fluorescers to convert the energy from ionizing radiation to photons. These photons are then transported to a transducer (photovoltaic cell where the band-gap energy is matched to the photon energy) to produce electrical current. A great deal of work has been developed around PIDEC in which different geometrical interfaces between the ionizing radiation and an excimer emitter have been examined. PIDEC was developed to overcome the limitations which were identified in the 1950s for p-n junction based betavoltaics and alphavoltaics (e.g., radiation damage, short lifetime, and low efficiency). PIDEC addresses some important issues; it is a way of matching the scale length of the radiation source to the transducer (the fluorescer can absorb all of the energy from the radiation source by adjusting size and pressure). It has high theoretical conversion efficiencies and provides a means of shielding sensitive transducers from radiation. Typical theoretical maximum system efficiencies can approach the theoretical limitation of rare gas excimers fluorescers as shown in Table 3.13 where η_f is the fluorescence efficiency, E_λ (eV) is the average photon energy and E_g is band-gap energy of the photovoltaic material. The variation in efficiencies is based on design parameters (e.g., interface between the fluorescer gas and radiation source, the system size, photon transport to the transducer, the operational characteristic of the p-n junction and matchup of transducer to photons). PIDEC was proposed for use with fusion [57], fission [58], and conventional decay sources [46, 60, 61].

Table 3.15 Properties for some commercially available wide band-gap materials are shown in this Table (3.20)

Property	GaP	3C-SiC	6H-SiC	4H-SiC	GaN	ZnO	Diamond	AlN	BN
Crystal structure	Zinc blende (Cubic)	Zinc blende (Cubic)	Wurtzite	Wurtzite	Wurtzite	Wurtzite	Diamond	Wurtzite	Zinc blende
Group of symmetry	T_d^2-F43 m	T_d^2-F43 m	C_{6v}^4-P6$_3$mc	C_{6v}^4-P6$_3$mc	C_{6v}^4-P6$_3$mc	C_{6v}^4-P6$_3$mc	O_h^7-Fd3m	C_{6v}^4-P6$_3$mc	T_d^2-F43m
Number of atoms per cm^3	$4.9 \cdot 10^{22}$				$8.9 \cdot 10^{22}$		$1.7 \cdot 10^{23}$	$9.6 \cdot 10^{22}$	
Debye temperature K	445	1200	1200	1300	600		1860	1150	1700
Density g cm^{-3}	4.14	3.166	3.21		6.15	5.642	3.515	3.255	3.48
Dielectric const. (static)	11.1	9.72	9.66	9.66	8.9	8.75	5.7	9.14	7.1
Dielectric const. (high freq.)	9.11	6.52	6.52	6.52	5.35	3.75		4.84	4.5
Effective longitudinal electron mass m_l	$1.12m_o$	$0.68m_o$	$0.20m_o$	$0.29m_o$	$0.20m_o$		$1.40\,m_o$	$0.4\,m_o$	$0.35m_o$
Effective transverse electron mass m_t	$0.22m_o$	$0.25m_o$	$0.42m_o$	$0.42m_o$	$0.20m_o$		$0.36\,m_o$		$0.24m_o$
Effective heavy hole mass m_h	$0.79m_o$				$1.4m_o$		$2.12m_o$	$3.53m_o$	$0.37m_o$
Effective light hole mass m_{lp}	$0.14m_o$				$0.3m_o$		$0.70m_o$	$3.53m_o$	$0.150m_o$
Electron affinity eV	3.8				4.1		−0.070	0.6	4.5
Lattice constant angstrom	5.4505	4.3596	$a = 3.0730$ $b = 10.053$	$a = 3.0730$ $b = 10.053$	$a = 3.189$ $c = 5.186$	$a = 4.75$ $c = 2.92$	3.567	$a = 3.11$ $c = 4.98$	3.6157
Optical phonon energy MeV	51	102.8	104.2	104.2	91.2		160	99.2	130
Band-gap eV	2.26	2.26	3.0	3.3	3.5	3.37	5.47	6.2	6.2–6.4
Breakdown V MV/cm	~1.1	~2	~3	~3	~3		1–10	1.2	2
Electron mobility cm^{2}V^{-1}s^{-1}	250	1000	380	800	300	80	2200	300	200
Hole mobility cm^{2}V^{-1}s^{-1}	150	50	40	140	350		2000	14	500
Melting Point C	1457	2830	2830	2830	2500	1977	4373	3273	2973
Thermal conductivity Wcm^{-1}C^{-1}	1.1	4.9	4.9	4.9	1.3	0.54	20	2.85	7.4
Hardness mohs scale	5	9.2	9.2	9.2		4	10		9.5

Gas

If a gaseous volume source is used, then it is possible to scale a PIDEC cell to a reasonable power density. In this section, an example based on a high pressure Kr-85 is used. Kr-85 uses the beta particles it releases to self excite the gas and produce excimer photons [9]. This example was chosen because it illustrates how effective a volume source can be.

If the PIDEC cell volume is 1 l at 1000 atm, it will contain about 3450 g of Kr-85.[1] Kr-85 produces about 0.51 W/g (see Chap. 1). The absolute maximum power density produced by 1000 atm of Kr-85 per cm^3 is 0.51 W/g times 3. 45 g/cm^3 which is 1.76 W/cm^3. The total power deposited in the 1 l volume with 1000 atm of Kr-85 is about 1,760 W. Using the Kr-85 as an intermediate transducer that produces fluorescence, the efficiency of converting the power deposited in the cell into fluorescence is 50 %. If the PIDEC cell uses a SiC photovoltaic cell as a transducer, the approximate efficiency of the photovoltaic cell in converting a Kr excimer photon to electrical power is approximately 16 % [60]. If the SiC photovoltaic cells are perfectly coupled to the fluorescence source, the PIDEC cell will produce about 140.8 W or a power density of about 0.1408 W/cm^3. This is an impressive power density, but as discussed in Chap. 2, there is a world-wide inventory of $\sim$373,000 g of Kr-85 [62] which is enough for only 108 units.

Solid Sources that Can Mimic Gas

Solid radioisotopes can effectively mimic gaseous like behavior by mixing the solid radioisotope in aerosol form with a gas or by embedding the solid radioisotope in thin fibers or films that hang in the gas (Figs. 3.31 and 3.39). The average density of radioisotopes in the mixed phase systems can be very high. These type of mixed phase systems can approach the maximum possible power density of a true volume source [10].
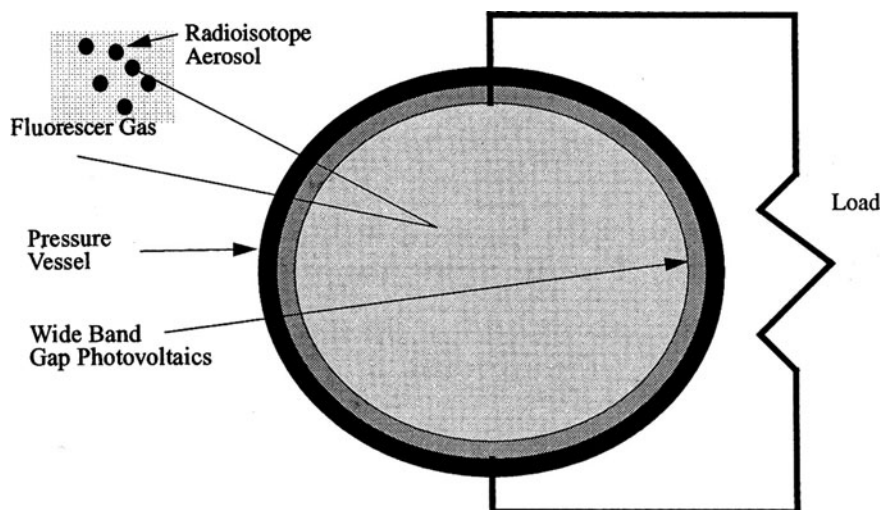
Solid-State

By focusing on the matching of scale lengths for the radiation transport process to the transducer in configurations which limit radiation damage, improvement in efficiency is possible. One example which might bear interesting results is the use of solid-state fluorescers which have limited or no self-absorption of the photon

---

[1]The mass of Kr is estimated using Van der Waals equation of state to describe the relationship between pressure and temperature as shown in the equation below, where n is the number of moles of Kr, a and b for Krypton are 0.5193 Pa $\cdot$ m^6/mol^2 and 0.000106 m^3/mol respectively, R is the universal gas constant (8.3145 J/mol $\cdot$ K) and T is temperature in Kelvin.

$$\left[P + a\frac{n^2}{V^2}\right]\left(\frac{V}{n} - b\right) = RT.$$

Fig. 3.39 Schematic diagram of a PIDEC nuclear battery which uses a radioisotope fuel in aerosol form [10]

emission. This differs from the discussion of solid-state scintillator research (e.g., polymers, phosphors, liquid scintillators, etc.). Scintillators were developed for radiation detection in situations where the dose rates were orders of magnitude lower than nuclear batteries. In prior nuclear battery research the existing scintillators were adopted for use in nuclear batteries. The self-absorption problems in these types of line sources have not been adequately considered as the power density in the scintillator scales up. The solid-state scintillator lifetime is thus short with strong ionizing radiation sources [63–67].

The self-absorption issue was considered for solid-state emitters by focusing on direct wide-band gap materials and excitons [68]. In this approach, the radiation source is embedded in a diamond crystal. As the radiation interacts with the diamond crystal lattice, the electron-hole pairs which form are weakly bound and create an exciton (with a binding energy of ~ 70 mV). Provided the crystal temperature is on the order of liquid nitrogen temperatures, the electron-hole pairs diffuse together and when they recombine, they do so directly without the need for a phonon. The photon energy is about 5.1 eV. The photon will efficiently exit the crystal and be transported to a photovoltaic cell that has a band-gap that matches well with the photon energy (e.g., $Al_xGa_{1-x}N$ *band-gap* can be tailored from 3.4 eV $(x_{Al} = 0)$ to 6.2 eV $(x_{Al} = 1)$ [69]). The Solid-State Electrical Generator using Radionuclide Induced Exciton Production (SEGRIEP) was conceived of for space exploration. Due to diamond's high thermal conductivity and the background temperature of space being 4 K, it was shown that it is feasible to build a radiative cooling system to maintain liquid nitrogen temperatures in the diamond crystal.

3.2.5 Solid-State Emitter and PV

Diamond is not a direct band-gap material but does have a bound exciton which can be used like a direct band-gap emitter. However, there will be no self-absorption of the exciton photon because the photon energy, 5.1 eV, is less than the band-gap of diamond, 5.49 eV. The binding energy of the electron-hole pair that makes up the exciton is 70 mV. This device will have temperature limitations that need to be explored. The theoretical maximum efficiency for this configuration is 33 %.

An approach being studied by the authors that is similar to the SEGRIEP concept is to use solid-state emitters based on high quality binary solid state crystals which exhibit wide band-gaps and direct band-gap transitions. In a direct wide band-gap binary material, the photon self-absorption and reabsorption processes are in balance until the photon escapes the solid. Loss processes such as luminescence emission from the surface and Auger recombination can be limited by proper design. The photon can escape through a loss cone that is coupled to a photovoltaic cell transducer (Fig. 3.40). Ionizing radiation will create displacements in the solid-state crystal. The rate of displacements will be on the order of 170 displacements per ion fragment. The number of photons created by each fragment (with estimated energy of 10 MeV) is on the order of 2 million (fraction of energy into electron-hole pair formation (0.42) times the energy of fragment (10,000,000 eV)/band-gap of semiconductor (2.2 eV for GaP)). Thus, the rate of photon generation exceeds the rate of potential trap formation by a factor of 20,000. The potential traps do continue to build up with time. However, if the device operates at a temperature where self-annealing can occur (600–800 K), there will be
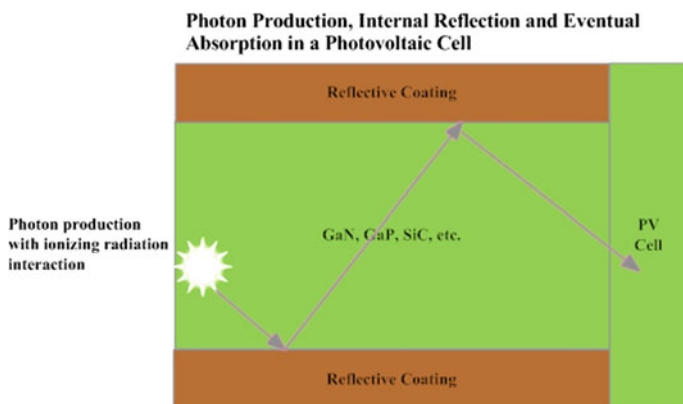
Fig. 3.40 The solid-state material interacts with radiation and produces an electron-hole pair. The pair recombines and produces a photon. The photon is then reabsorbed to form another electron-hole pair or to reflect off the surface. If an electron-hole pair is formed, it recombines and produces a photon. The process is in balance with few other losses and continues until the photon is lost through the loss cone into the PV cell. The theoretical maximum efficiency for this configuration is 33 %

a rate at which point defects (displacements) are repaired at a sufficient rate to limit the effects of displacements due to radiation damage. It is feasible to use this balance of defect creation and defect repair to extend the lifetime of the solid-state emitter. This device will still have radiation damage issues. Defects will be created in the emitter and the traps that are formed can absorb photons and electrons. The key to the extended lifetime of the emitter is through self-annealing to mitigate trap formation. Displacement issues are more serious with binary materials such as, III–V, than with diamond (used in the SEGRIEP concept). The physics of the process is still being researched and refined.

3.2.5.1 Phosphors

A number of phosphors have been developed for use in CRT based color TV and radiation detectors. The progress in materials is discussed.

Materials may emit light by incandescence (all atoms radiate) or luminescence (where a few atoms called emission centers radiate) when excited by electron beams or by other ionizing radiation (e.g., alphas, betas, neutrons or gamma rays). The mechanism is based on the interaction of ionizing radiation with matter [70]. The ionizing radiation interacts with matter by generating ions and excitation in the medium. The ions eject highly energetic electrons (primary electrons) which are further multiplied through collisions, creating secondary and higher order electrons. These energetic electrons excite the light-emitting centers which create the photons.

The class of nuclear batteries discussed in this section uses solid phosphors. When energetic electrons are incident on a solid surface, a small fraction of the electrons are scattered and reflected while the bulk of the electrons continue into the solid and create electron-hole pairs. The average energy (E_{av}) required to form an electron-hole pair near the band edges is given for both the direct or indirect band-gap by an empirical formula,

$$E_{av} = 2.67E_g + 0.87\,[\text{eV}] \tag{3.75}$$

where E_g is the band-gap energy for either director or indirect band-gap materials.

Inorganic phosphors have defects in the crystal structure such as dopants (or activators) or dislocations which create the emission center. The wavelength that is emitted is material dependent. The majority of phosphors lose efficiency over time due to several factors. The energy input into the phosphor can cause the activator to undergo a change of its valence state, the crystal lattice degrades due to radiation induced displacements, the activators can diffuse through the material, and the surface can oxidize thus creating a layer which absorbs either the excitation particle or the photons emitted by the phosphor.

Phosphors have been used in a number of applications such as lighting (e.g., fluorescence tubes and white light LEDs), phosphor thermometry (measuring temperature), glow-in-the-dark toys, radioluminescence (luminescence from interactions with ionizing radiation), electroluminescence (LCDs), and Cathode Ray

**Table 3.16** Typical high efficiency phosphors [71]

Material	Energy efficiency	Peak wavelength (nm)
$Zn_2SiO_4:Mn^{2+}$	8	525
$CaWO_4:Pb:$	3.4	425
ZnS:Ag,Cl	21	450
ZnS:Cu,Al	23, 17	530
$Y_2O_2S:Eu^{3+}$	13	626
$Y_2O_3:Eu^{3+}$	8.7	611
$Gd_2O_2S:Tb^{3+}$	15	544
$CsI:Tl^+$	11	Green
$CaS:Ce^{3+}$	22	Yellowish green
$LaOBr:Tb^{3+}$	20	544

Tubes (CRTs). Phosphors that have been developed for use in CRTs or radioluminescence are typically targeted for nuclear battery research based on their resistance to radiation damage. Some example phosphors with high efficiencies are shown in Table 3.16.

The more efficient phosphors in Table 3.16 have been used in nuclear battery research. For example, ZnS:Cu emits in the green wavelength [72] as shown in Fig. 3.41, and $Y_2O_2S:Eu$ emits in the red wavelength [73] as shown in Fig. 3.42.

A common cell design is based on rectangular geometries. An example of a cell design which demonstrates the main issues involved is shown in Fig. 3.43. Here, a thin coating of a beta emitting isotope is placed at the center of the cell. The isotope layer has a thickness "d" which should be thin enough to allow as much of the isotropic beta emission to exit the radioisotope layer and enter the phosphor layer. Optimizing d requires the use of modeling which take into account the beta emission spectrum (Appendix A) as well as the angle of emission. The cell is symmetric so that beta particles with both up and downward vector components

Fig. 3.41 The emission spectra for the ZnS:Cu phosphor. The emission ranges from about 400–650 nm with a peak at 530 nm
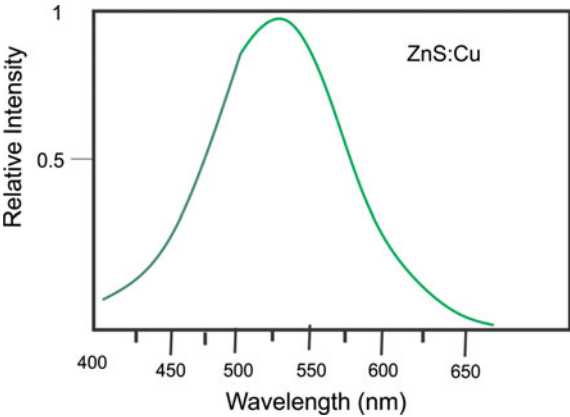
Fig. 3.42 The emission spectra for the Y_2O_2S:Eu phosphor. The emission ranges from about 570–650 nm with a peak at 626 nm
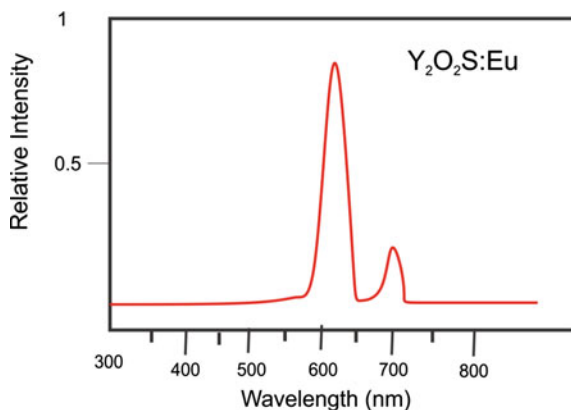
Fig. 3.43 Diagram of an indirect nuclear battery which uses a Pm-147 beta source and a ZnS:Cu phosphor which interacts with the beta particles and produces photons. The photons then are transported to photovoltaic cells [73]
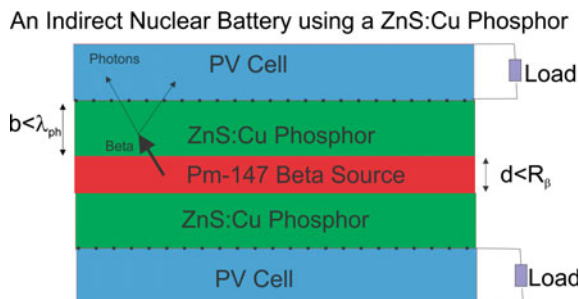

have a good probability of entering the phosphor. This typically requires that "d" is less than the range of the beta particle in the Pm-147 layer (R_β). The beta particle must then travel through the phosphor and interact. The phosphor layer has a thickness "b" which needs to be thick enough to absorb the energy from the beta particle. The interaction produces photons in the phosphor. The photon emission is isotropic. The photons which are born with a vector in the direction towards the Pm-147 layer are lost unless the design puts a thin reflective layer of aluminum on both side of the Pm-147 layer. The other complicating factor is that the phosphor layer is not optically thin, so there will be self-absorption of the photons. The design of the phosphor layer is complicated in that the thickness of the phosphor should be greater than the range of a beta particle in the phosphor (R_β) but less than the mean free path of a photon in phosphor layer (λ_{ph}). The grid has transparency efficiency (η_{Gtr}) which is defined as the fraction of photons which are transmitted through the grid. The photons then enter the photovoltaic cell. This is somewhat complicated in that the photons enter at the photovoltaic cell at angles which are much different than those experienced by solar cells (Figs. 3.44 and 3.45).

The photovoltaic cell used in a nuclear battery is basically the same type of cell used to capture solar energy. The photovoltaic cell has a band-gap of E_g, which needs to be matched as closely as possible to the emission spectrum of the

Fig. 3.44 This is a photovoltaic cell which consists of a n-type layer, a p-type layer and a depletion area. Solar radiation is made up of paraxial rays which impinge upon the solar cell and bounce between the reflective layers until the photon is absorbed. Solar cell architecture is optimized so that there is a high probability that the photon is absorbed by the depletion layer
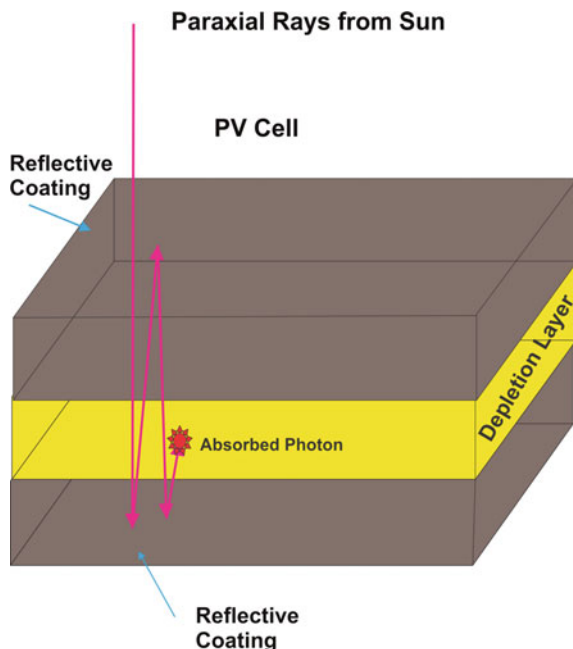
Fig. 3.45 This is a photovoltaic cell which consists of a n-type layer, a p-type layer and a depletion area. Fluorescence from the indirect battery phosphor produces rays which impinge upon the solar cell and bounce between the reflective layers until the photon is absorbed. The architecture for an indirect battery must be designed so that the probability that the photon is absorbed by the depletion layer is maximized
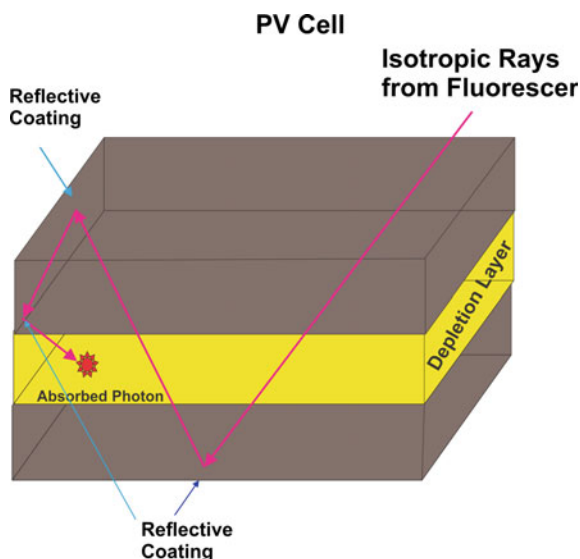
phosphor. As described in the previous section on gas fluorescers, since the phosphor has a broad emission spectrum, there will be inefficiencies in the conversion process. The cell is made by interfacing p-type material with n-type

material. A junction is formed between n- and p-type semiconductor materials. At the junction's interface, the diffusion of charge carriers across the junction sets up a space charge which in turn sets up an electrical potential and electrical field (Fig. 3.17). The depletion region thus has an electrical field which separates electron-hole pairs when they are created by the interaction of radiation with the material. Outside of the depletion region, electron-hole pairs which are created by the interaction of radiation with matter do not have electrical fields to cause their separation. The most likely fate of the charge carriers beyond the depletion region is that they will instead recombine or become trapped by defects. Some of the charge carriers may drift into the depletion region and become part of the cell current driven by the junction's electric field.

There is also another significant difference between the solar photon source and a phosphor photon source. First, assume that photons are rays being emitted from a source. A solar cell captures photons (operating as paraxial rays) from the sun as shown in Fig. 3.44. The reason that the rays are paraxial is that the sun is an isotropic photon emitter approximately 93 million miles from the earth. The earth intersects only the photons which are emitted in a very small solid angle. The photons which the earth intersects are essentially parallel rays or "paraxial."

The paraxial rays enter a solar cell at the same angle. The cell is coated with an antireflective material which allows the rays to enter with minimal reflection. It moves through the cell and will eventually be absorbed. However, the challenge is to absorb the photon in the depletion layer. Some photons are not absorbed by the depletion layer and they are reflected by the interface because the antireflective coating has a lower index of refraction than the photovoltaic cell materials. As light travels from one medium with an index of refection of n_1 to another medium with lower index of refraction n_2, the light will be refracted at 90° when it hits the interface at an angle greater than a critical angle (θ_c). This is called total internal reflection. The critical angle can be determined from Snell's law,

$$\sin(\theta_c) = \frac{n_2}{n_1} \tag{3.76}$$

where $n_1 > n_2$.

Thus any photon that is not absorbed will reflect off the bottom surface. This gives the photon one more pass at being absorbed in the depletion region where the p-n junction resides. If the photon is absorbed in the region outside of the depletion region, it will form an electron-hole pair. The electron-hole pair most likely will recombine thus emitting an isotropic photon of energy E_g. This photon will travel through the medium and hopefully be absorbed in the depletion layer. If not, and if it is able to reflect off of the top or bottom surface and is absorbed outside the depletion layer, it will again form an electron-hole pair and its most likely fate is to recombine. This process of perpetually creating electron-hole pairs and through recombination and creating a photon with energy equal to the band-gap will practically extend the photon lifetime until it is absorbed in the depletion layer, at

which point the most likely fate of the electron-hole pair is to be separated by the electric field thus creating a current.

The dimensions of the solar cell can be adjusted such that photons bounce between the top and bottom surfaces until the photons are absorbed with a high probability in the depletion layer.

Isotropic fluorescer sources such as phosphors enter the photovoltaic cells at various angles based upon the angle of emission and the reflective property of the waveguide which directs the photons to the PV cell. Due to the various angles at which a photon can enter the cell, there will be additional inefficiencies because of the wide variety of paths photons will take before they are absorbed or lost. The probability of absorption in the depletion layer will be lower than that for paraxial rays.

3.2.6 Hybrid Solid-State Emitter

A hybrid approach to addressing the self-absorption problem is to form micro-bubbles with excimer gases in the solid-state material [74]. Micro-bubbles can be formed at very high pressures in a solid-state material using ion implantation (up to 4 GPa). At 4 GPa, the density of a xenon gas bubble is on the order of 4 g/cm^3. The transport length of radiation in a high pressure xenon micro-bubble is about 5 μm, about the scale length of the heavy fragment. As shown in Fig. 3.46, the radioisotope can be coated on the cell's surface. A series of micro-bubbles lie between the radioisotope layer and the p-n junction. The particle from the radioisotope is emitted isotropically and the micro-bubble serves as both a shield to protect the junction as well as a photon source which emits at the excimer
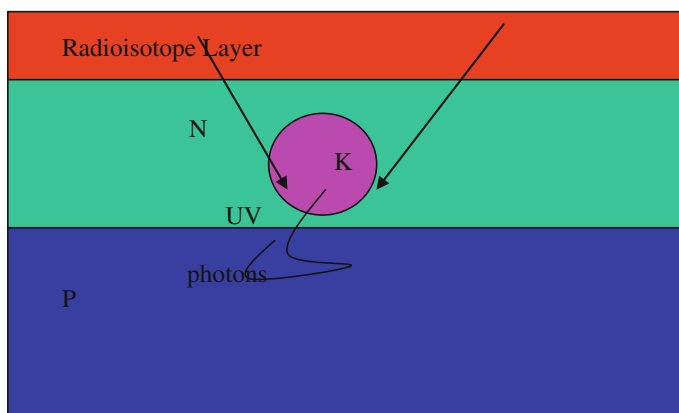
Fig. 3.46 Option A: Micro bubble as a radiation shield as well as a way of converting the kinetic energy of radiation into narrow band UV photons that are absorbed by the p-n junction

wavelength. The photons then resonate in the PV cell and are absorbed. Even at this high density the issues of pressure broadening should not lead to losses and the micro bubble should not self-absorb. Thus the cell will have a transducer scale length compatible with the radiation source and with the PV cell. The advantages of this approach are that the wide band-gap p-n structure will use a thin film with the radioisotope coated or imbedded into the structure. Wide band-gap materials can operate at high temperatures without efficiency loss and have high thermal conductivities. The films can be stacked, which will allow for scaling of the power source at relatively high power densities (see discussion on the limitations of nuclear battery power density). Problems with this mechanism do exist. Even though it is well known that micro-bubbles form by ion implantation, the possibility of the bubble delaminating the material may be a problem. The theoretical maximum efficiency for this configuration is 20–30 %.

3.2.7 Heat Based

Nuclear energy conversion systems based on heat production can take advantage of the fact that all of the energy content in ionizing radiation can be converted to heat, unlike systems which are based on ions produced by ionizing radiation where at most 50 % of the energy goes into ion production. Direct energy conversion systems based on heat production include the RTG (which uses the Seebeck effect), thermoelectric energy conversion and thermionic energy conversion.

3.2.7.1 Seebeck Effect and RTG

The thermoelectric effect was first observed by Thomas Johann Seebeck in 1821. In this experiment, a magnetic needle was deflected when it was positioned near a circuit made of two different conductors. Seebeck attributed the observation to temperature, but did not associate it with a current flow (which would produce a magnetic field) in the junction due to temperature. He went on to study many types of materials and saw variation of the effect. One of his choices of materials would have produced thermoelectric efficiencies near 3 %. This was on par with steam engine efficiencies during that time [75]. In 1834, Jean Charles Athanase Peltier observed that when current flowed through a junction made of two different materials, it caused the metal to either cool down or heat up depending on the direction of the current flow. This discovery was furthered by the work of Emil Lenz of the St. Petersburg Academy in 1838 when he demonstrated that water on a bismuth-antimony junction could form ice when current was flowed one direction or could melt ice when current flowed in the other direction.

William Thompson (also known as Lord Kelvin) reasoned that the Seebeck and Peltier effects were related. Based on a thermodynamic analysis, Lord Kelvin concluded that a third effect must exist in which heating and cooling could take
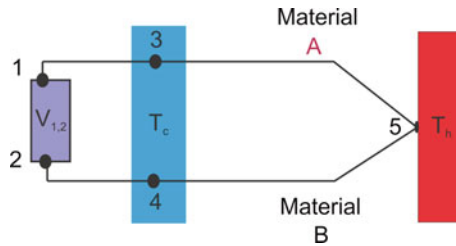
Fig. 3.47 The basic circuit for a thermocouple is shown. There are two materials (*A* and *B*) that make up the thermoelectric junction. *Point 5* is where the two materials are connected and are attached to the heat source (T_h). *Point 3* is where material A is attached to the sink (T_c) and *point 4* is where material B is attached to the sink. The voltage across *points 1* and *2* is the Seebeck voltage

place in a homogeneous conductor when current is flowed in the direction of a temperature gradient. This is called the Thompson effect.

In its most basic form, the thermoelectric effect occurs when two different metals are connected between a high temperature side (T_h) and a low temperature sink (T_c) as shown in Fig. 3.47. The voltage between points 1 and 2 ($V_{1,2}$) is the Seebeck voltage. The Seebeck voltage is related to the temperature difference between the heat source and the sink ($T_h - T_c$) by the Seebeck coefficient (α) as seen in Eq. (3.78).

$$\Delta V = V_2 - V_1 = V_{1,2} = (\alpha_A - \alpha_b)(T_h - T_c) = (\alpha_A - \alpha_B)\Delta T \qquad (3.77)$$

So,

$$\frac{dV_{1,2}}{dT} = \alpha_A - \alpha_B \qquad (3.78)$$

A basic thermoelectric generator has a heat source (at temperature T_h) and a thermal sink (at temperature T_c). There will be two semiconductor legs, one being a p-type material and one being an n-type material as shown in Fig. 3.48. A load (with resistance R_L) is connected between the two legs as shown in the figure.

Fig. 3.48 Shown is a thermoelectric generator which consists of a heat source, two legs, a thermal sink and a load. The length of the legs is x
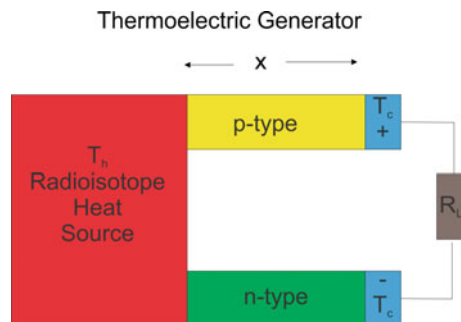
The efficiency of a thermoelectric generator is defined as,

$$\eta = \frac{P_0}{q_h} \tag{3.79}$$

where P_0 is the electrical power out of the generator and q_h is the thermal power input.

The thermal power into the hot legs of the thermoelectric generator from the heat source is dependent upon the thermal properties of the legs (namely the thermal conduction which goes as $K\Delta T$ where K is the thermal conductivity of the leg material). There will also be losses due to the current flow in the legs (this term goes as $\frac{1}{2}I^2R$ where R is the resistance of the leg materials and I is the current flow through the legs). Additionally, there is a heat generated due to the Peltier effect ($\alpha T_h I$). Since electrons flow from the n-type leg to the p-type leg, the current flow will have a minus sign. The term ½ comes from the fact that the Peltier effect causes absorption of heat at the source while half of the Joule heat is returned to the source. Thus,

$$q_h = K\Delta T + \alpha T_h I - \frac{1}{2}I^2R \tag{3.80}$$

The output power of the thermoelectric generator is,

$$P_0 = I^2 R_L \tag{3.81}$$

where R_L is the load resistor.

The open circuit voltage (V_{oc}) for the thermoelectric generator is the Seebeck voltage,

$$V_{oc} = \alpha\Delta T \tag{3.82}$$

So, the current that flows through the generator is,

$$I = \frac{\alpha\Delta T}{R + R_L} \tag{3.83}$$

Plugging Eqs. (3.81) and (3.82) into Eq. (3.80), the system efficiency becomes,

$$\eta = \frac{R_L I^2}{K\Delta T + \alpha T_h I - \frac{1}{2}I^2R} \tag{3.84}$$

The efficiency equation is very basic and more complex versions of this equation exist in the literature.

In evaluating thermoelectric generators, an important grouping of properties of the materials used is the figure of merit (Z),
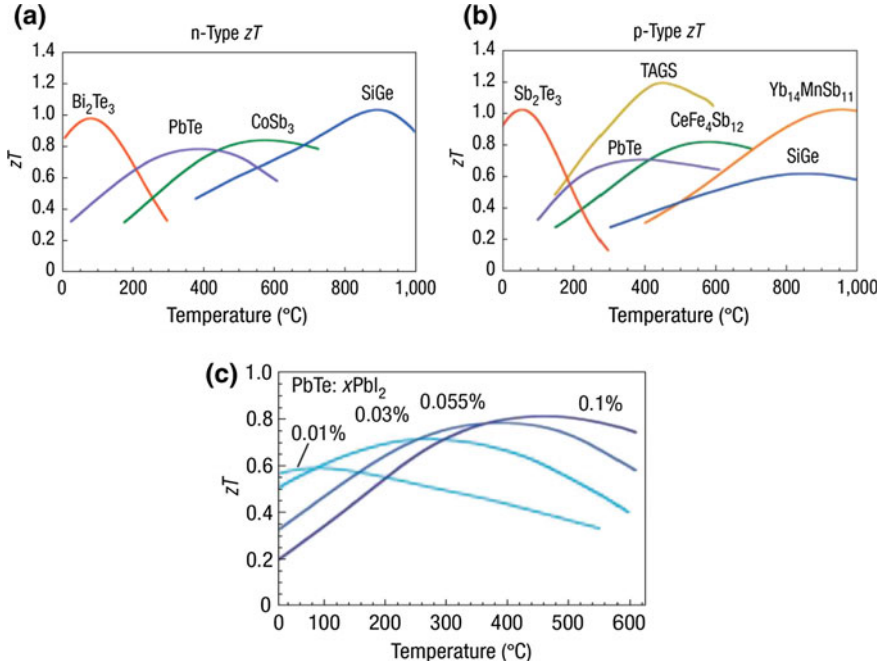
Fig. 3.49 Figure of merit of p-type materials (**a**), figure of merit for n-type materials (**b**), and doping concentration modifying the maximum *ZT* (**c**) [76]

$$Z = \frac{\alpha^2}{RK} \tag{3.85}$$

The figure of merit (*Z*) is an oft reported value which is used to judge the suitability of a material for a temperature range. Another value which is oft reported is the product *ZT*, which is a dimensionless number and provides basically the same type of information as *Z* as shown in Fig. 3.49.

RTGs are the "gold standard" in nuclear battery technology. They have had a long history of successful missions as shown in Table 3.17. Some of these RTGs are shown in Figs. 3.50, 3.51, 3.52, 3.53 and 3.54.

3.2.7.2 Thermoionics

The thermionic generator is basically made of two electrode surfaces (one an emitter and the other a collector) as shown in Fig. 3.55. The emitter is a metal with a known work function. In a metal, the electrons are free to move, but are bound to the metal by forces of attraction between the electrons and ions in the lattice. The

**Table 3.17** RTGs used in various NASA missions [76]

Mission	RTG	TE	Destination	Year	Mission length
Transit 4A	SNAP-3B7(1)	PbTe	Earth orbit	1961	15
Transit 4B	SNAP-3B8(1)	PbTe	Earth orbit	1962	9
Apollo 12 Figure 3.50	SNAP-27 RTG (1)	PbTe	Lunar surface	1969	8
Pioneer-10 Figure 3.51	SNAP-19 RTG (4)	PbTe	Outer planets	1972	34
Triad-01-1X	SNAP-9A (1)	PbTe	Earth orbit	1972	15
Pioneer-11 Figure 3.51	SNAP-19 RTG (4)	PbTe	Outer Planets	1973	35
Viking 1 Figure 3.51	SNAP-19 RTG (2)	PbTe	Mars	1975	4
Viking 2 Figure 3.51	SNAP-19 RTG (2)	PbTe	Mars	1975	6
LES 8 Figure 3.52	MHW-RTG	Si-Ge	Earth orbit	1976	15
LES 9 Figure 3.52	MHW-RTG	SiGe	Earth orbit	1976	15
Voyager 1 Figure 3.52	MHW-RTG	Si-Ge	Outer planets	1977	31
Voyager 2 Figure 3.52	MHW-RTG	Si-Ge	Outer planets	1977	31
Galileo Figure 3.53	GPHS-RTG	Si-Ge	Outer planets	1989	14
Ulysses Figure 3.53	GPHS-RTG (1)	Si-Ge	Outer planets/sun	1990	18
Cassini Figure 3.53	GPHS-RTG (3); RHU (117)	Si-Ge	Outer planets	1997	11
New Horizons Figure 3.53	GPHS-RTG (1)	Si-Ge	Outer planets	2005	3
MSL Figure 3.54	MMRTG	PbTe	Mars surface	2011	3

work function (φ) is defined as the energy at which electrons overcome the force of attraction.

When heat is applied to the emitter, the energy the free electrons will have a Boltzmann's energy distribution (Eq. 3.86). In Fig. 3.56, the function $f(E)$ is plotted as a function of energy. For this figure, a surface heated to 1,800 K has a work function of 4.15 eV. The cross hatched area represents the electrons whose energies exceed the work function and thus are emitted. One potential complication is a space charge buildup, which adds to the potential barrier the electrons must overcome. In this case, the electrons which are collected are those that have energy greater than the work function and potential barrier.

Fig. 3.50 SNAP 27 reactor used on the Apollo 12, 14, 15, 16 and 17 missions. The power output was initially 70 W. Its design lifetime was 2 years [77]
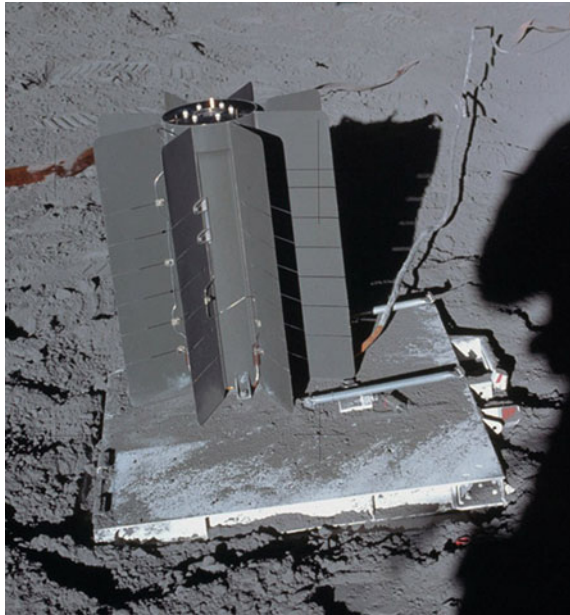
$$f(E) = 2\sqrt{\frac{E}{\pi}}\left(\frac{1}{k_B T}\right)^{3/2} e^{-\frac{E}{k_B T}} \tag{3.86}$$

The ideal current emitted by a heated surface is described by the Richardson-Dushman equation,

$$J = A_1 T^2 e^{-\frac{\varphi}{k_B T}} \tag{3.87}$$

where A_1 is a constant, T is temperature in Kelvin, φ is the work function and k_B is the Boltzmann constant.

The Richard-Dushman equation represents the saturation current from an emitting surface per unit area at a temperature T. The potential energy diagram of thermionic emitter and collector configuration is shown in Fig. 3.57.

In Fig. 3.57, electrons emitted by the emitter must have velocities such that they overcome the potential, $\delta + \varphi_c + V - \varphi_e$. This potential can be plugged into the Richardson-Dushman Eq. (3.87) to find the emitter current,
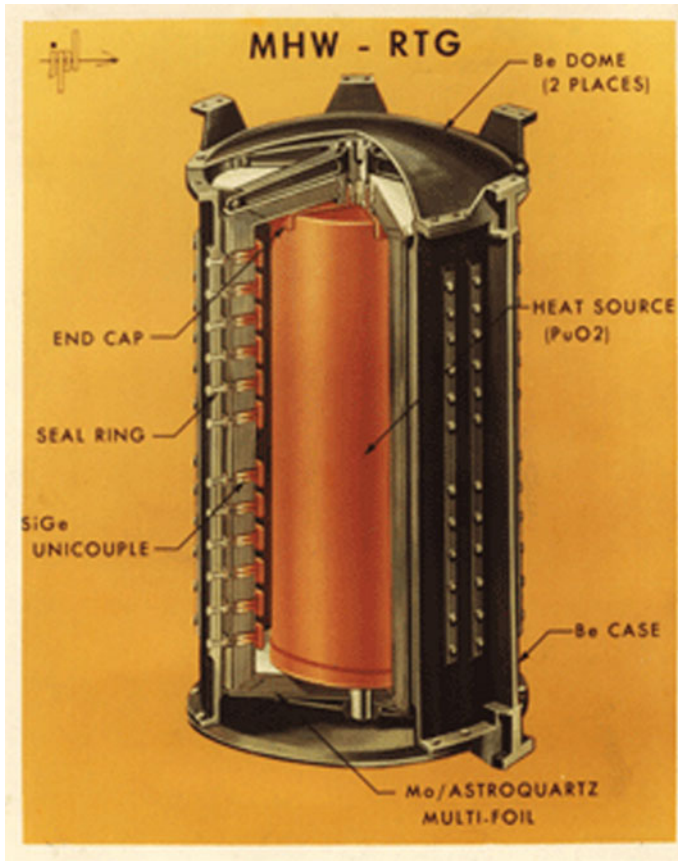
$$J_e = A_1 T_e^2 \exp\left[-\frac{e\varphi_e}{k_B T_e}\right] \exp\left[-\frac{e(\delta + \varphi_c + V + \varphi_e)}{k_B T}\right] \tag{3.88}$$

where $V_e = \varphi_k + \varphi_e = \delta\varphi_e + V$

Using the definition for V_e, Eq. (3.88) becomes
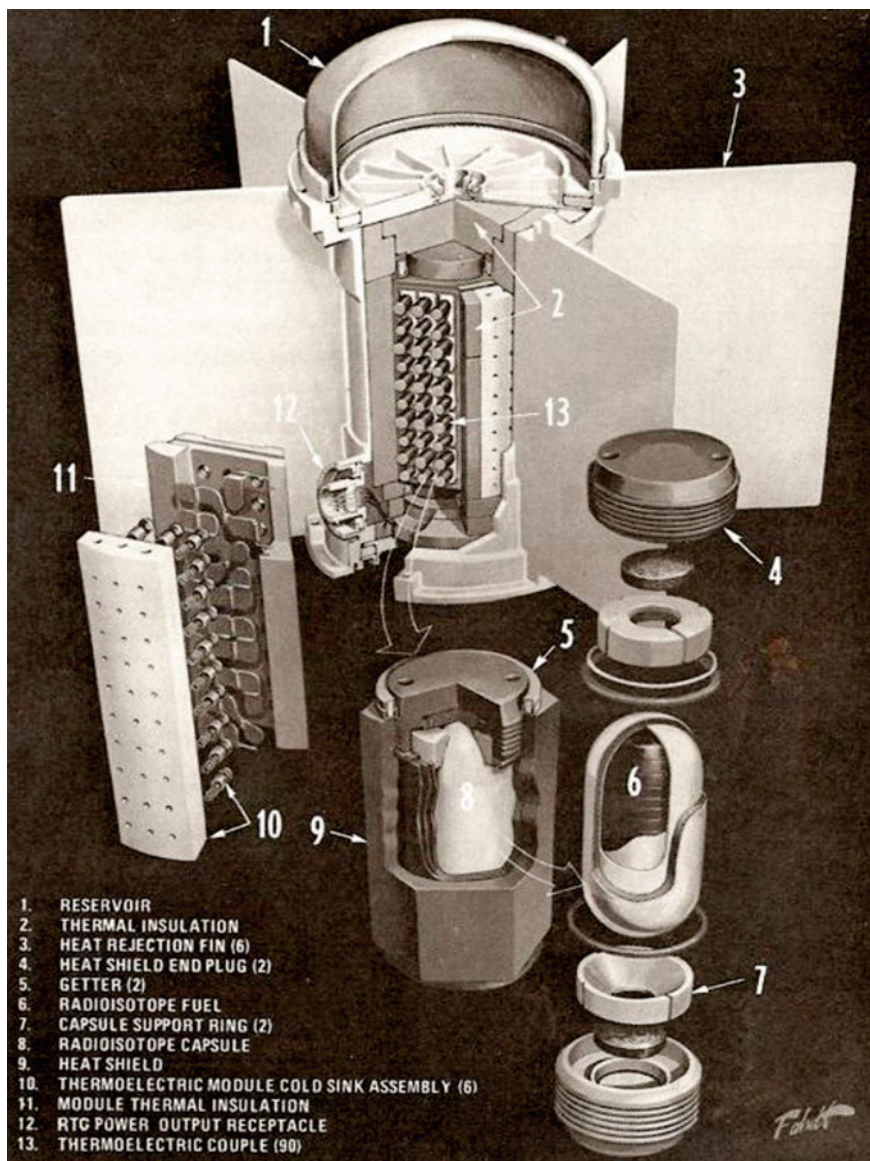
Fig. 3.51 SNAP 19 RTG used in Pioneer and Viking Missions. The initial power was 40.3 W electric for the Pioneer missions and 42.6 W electric for the Viking missions [77]

Fig. 3.52 The Multi-Hundred Watt (MHW) RTG was capable of producing 158 W electric. It was used on the Voyager missions [77]

$$J_e = A_1 T_e^2 \exp\left[\frac{-eV_e}{k_B T_e}\right] \tag{3.89}$$

The current from the collector to the emitter (or back current) comes from electrons in the collector that overcome the potential barrier δ. The back current is calculated from the Richardson-Dushman Eq. (3.87),

$$J_c = A_1 T_c^2 \exp\left[\frac{-e\varphi_c}{k_B T_c}\right] \exp\left[\frac{-e\delta}{k_B T_c}\right] \tag{3.90}$$
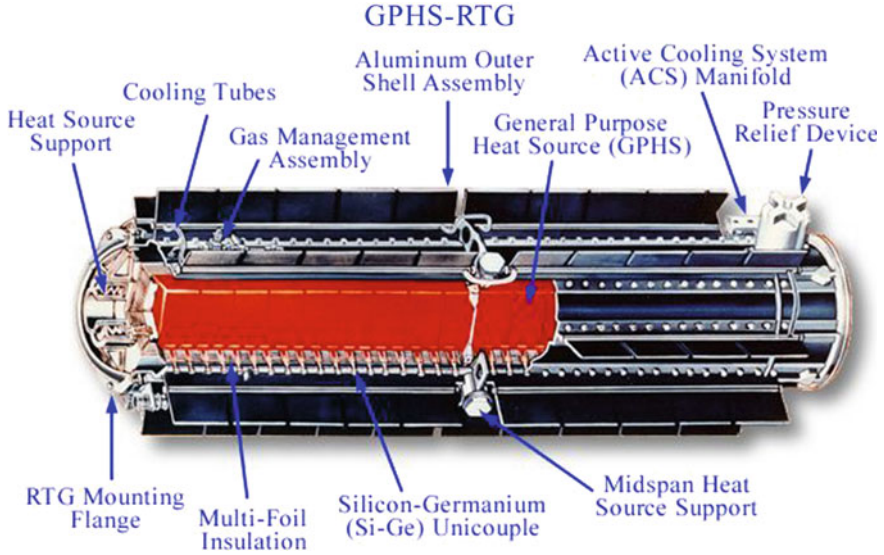
Fig. 3.53 The GPHS-RTG was used for the Ulysses and Cassini missions. Its power output was 292 W electric [77]

where $V_c = \varphi_c \delta$

$$J_c = A_1 T_c^2 \exp\left[\frac{-eV_c}{k_B T_c}\right] \tag{3.91}$$

The net current is,

$$J = J_e - J_c = A_1 T_e^2 \exp\left[-\frac{eV_e}{k_B T_e}\right] - A_1 T_c^2 \exp\left[-\frac{eV_c}{k_B T_c}\right] \tag{3.92}$$
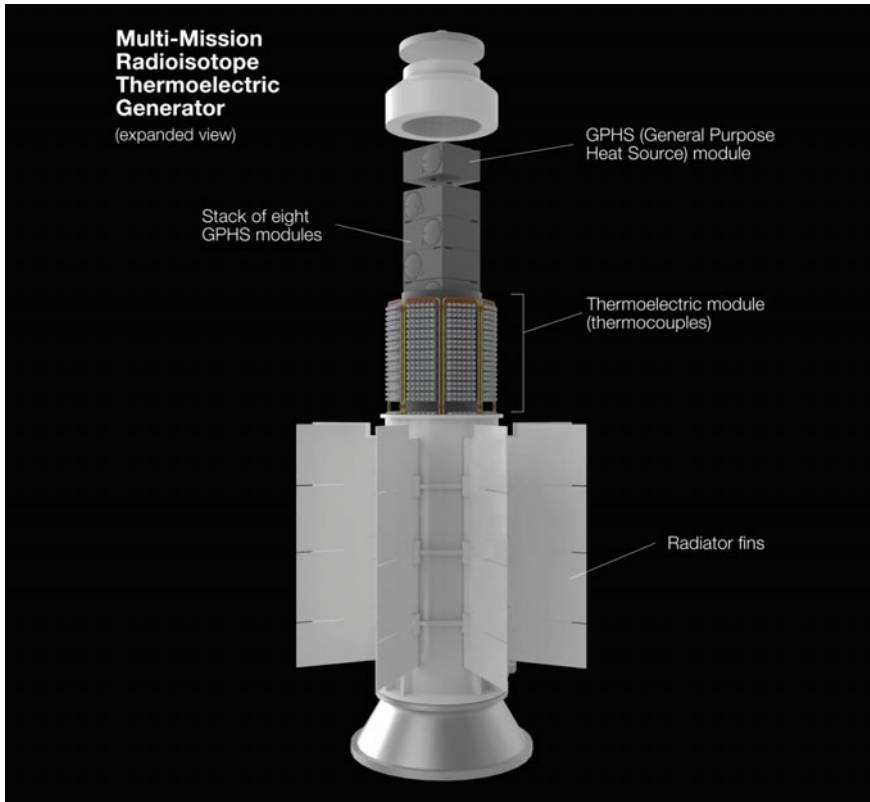
where J is a function of T_e, T_c, δ and φ_c.

The output voltage (V) is,

$$V = V_e - V_c = (\varphi_e - \varphi_c) + (\varphi_k - \delta) \tag{3.93}$$

When a load resistor (R_L) is added to the circuit, the voltage on the load (V_L) is,

$$V_L = V_e - V_c - IR_L$$

Fig. 3.54 The Multi-Mission radioisotope thermoelectric generator. The MMRTG will be used in NASA mars science laboratory rover mission [77]

where I is the current flow.

The open circuit voltage occurs when the net current flow (J) is zero. Thus the condition that $J_e = J_c$ gives,

$$A_1 T_e^2 \exp\left[-\frac{eV_e}{k_B T_e}\right] = A_1 T_c^2 \exp\left[-\frac{eV_c}{k_B T_c}\right] \tag{3.94}$$

Rearranging Eq. (3.94),

$$\frac{T_e^2}{T_c^2} = \exp\left[-\frac{eV_c}{k_B T_c}\right] \exp\left[\frac{eV_e}{k_B T_e}\right] \tag{3.95}$$

Fig. 3.55 The basic structure of a thermionic generator is shown. The generator consists of an emitter electrode and a collector electrode. The emitter electrode is heated and the collector electrode is cooled to a sink
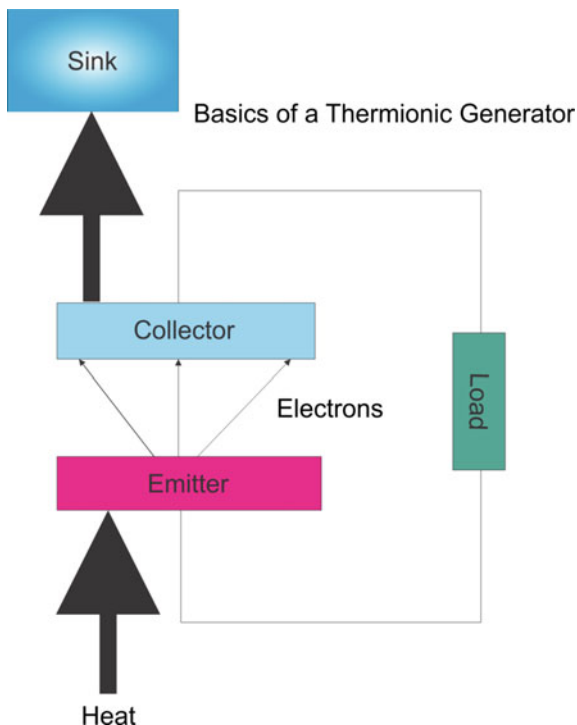
Fig. 3.56 The Boltzmann distribution of electron energy for a surface heated to 1,800 K. Shown is a line for a material with a work function of 4.15 eV. The electrons with energies above 4.15 eV are emitted from the surface
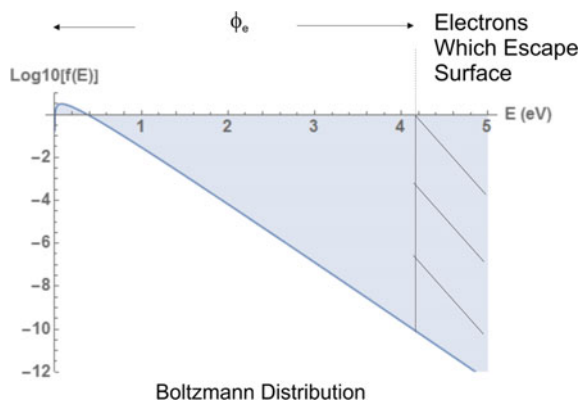
Equation (3.95) then becomes,

$$\left(\frac{T_e}{T_c}\right)^2 = \exp\left[\frac{e}{k_B}\left(\frac{V_e}{T_e} - \frac{V_c}{T_c}\right)\right] \qquad (3.96)$$

Fig. 3.57 The potential
energy level diagram between
the emitter and collector for a
thermionic device. V_e is the
potential energy of the
emitter, V_c is the potential
energy of the collector, φ_k is
the retarding potential barrier
due to space charge buildup, δ
is the retarding potential
barrier due to space charge
buildup on the collector side,
φ_c is the work function of the
collector, φ_e is the work
function for the emitter, V is
the operating voltage of the
cell, ψ_e is the electrical
potential for the emitter and
ψ_c is the electrical potential
for the collector
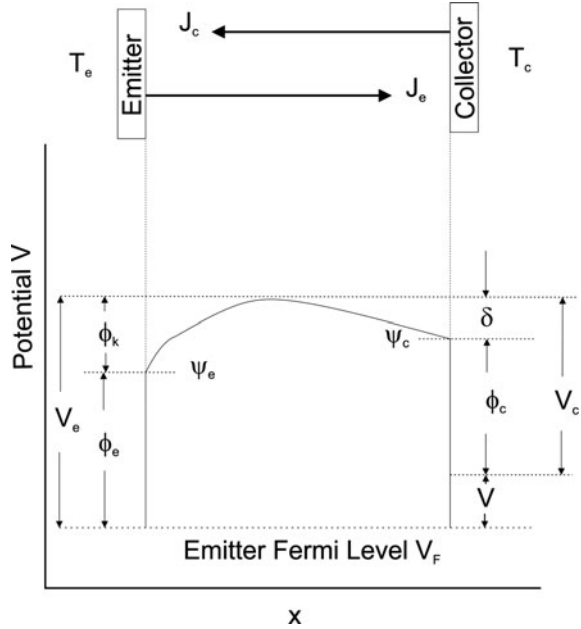
Take the natural log of Eq. (3.96),

$$2\ln\left[\frac{T_e}{T_c}\right] = \frac{e}{k_B}\left(\frac{V_e}{T_e} - \frac{V_c}{T_c}\right) \tag{3.97}$$

Realizing that $V_c = \varphi_c + \delta$ and $V_c = \delta + \varphi_e + V$,

$$2\ln\left[\frac{T_e}{T_c}\right] = \frac{e}{k_B T_e}\left[(\delta + \varphi_c + V_{oc}) - \left(\frac{T_e}{T_c}\right)(\varphi_c + \delta)\right] \tag{3.98}$$

Solve for V_{oc},

$$V_{oc} = \frac{2k_B T_e}{e}\ln\left(\frac{T_e}{T_c}\right) + (\varphi_c + \delta)\left(\frac{T_e}{T_c} + 1\right) \tag{3.99}$$

The efficiency of the cell is the power out ($V[J_e - J_c]$) divided by the power in
(q_s, which is the heat supplied by the emitter).

$$\eta = \frac{V(J_e - J_c)}{q_s} \tag{3.100}$$

Equation (3.100) does not take parasitic heat losses, space charge losses, or back
current losses into account.

Table 3.18 Various space based nuclear reactors developed over the years that operate with various energy conversion mechanisms

	SNAP 10 US	SP-100 US	Romashka USSR	Bouk USSR	Topaz 1 USSR	Topaz 2 USSR	SAFE 400 US
Date service	1965	1992	1967	1977	1987	1992	2016
KWth	45.5	2000	40	∼100	150	135	400
KWe	0.65	100	0.8	∼5	10	6	100
Fuel	U-ZrHx	UN	UC2	U-Mo	UO2	UO2	UN
Converter	TE	TEc	TE	TE	TI	TI	Bryton
Mass Kg	435	5422	455	∼390	320	1061	512
Neutron energy	Thermal	Fast	Fast	Fast	thermal	Epithermal	Fast
Control	Be	Be	Be	Be	Be	Be	Be
Coolant	NaK	Li	None	NaK	NaK	NaK	Na
Core Temp C	585	1377	1900	NA	1600	1900	1020
Emitter					Monocrystal Mo with W coating	Monocrystal Mo with W coating	
Collector					Polycrystalline Mo	Polycrystalline Mo	
Efficiency	1.4 %	5 %	2 %	∼5 %	6.67 %	9.3 %	25 %

The Topaz reactors used thermionics

TE-Thermoelectric, TI-Thermionic, Brayton-Brayton Cycle

The performance of a thermionic device is dependent upon the operating temperature and on the materials used for the emitter and collector. Table 3.18 is a summary of nuclear reactors using the method of direct energy conversion. The efficiencies achieved are consistent with the DCNB (which is the underlying mechanism of a thermionic energy convertor) discussed in this chapter.

3.2.7.3 Thermophotovoltaics

Thermophotovoltaics are similar in principle to PIDEC [75, 78–85]. The main differences are,

1. The photon spectrum is much broader. It is a black body spectrum coming off of a heat source (obeying Planks radiation formula in Eq. 3.101), and
2. The photovoltaic cells have to have a low band-gap in order to maximize the conversion of a black body spectrum to electricity since the emission for reasonably hot emitters is in the infrared (Fig. 3.58) [75].

Grey Body Emission vs Wavelength and Temperature
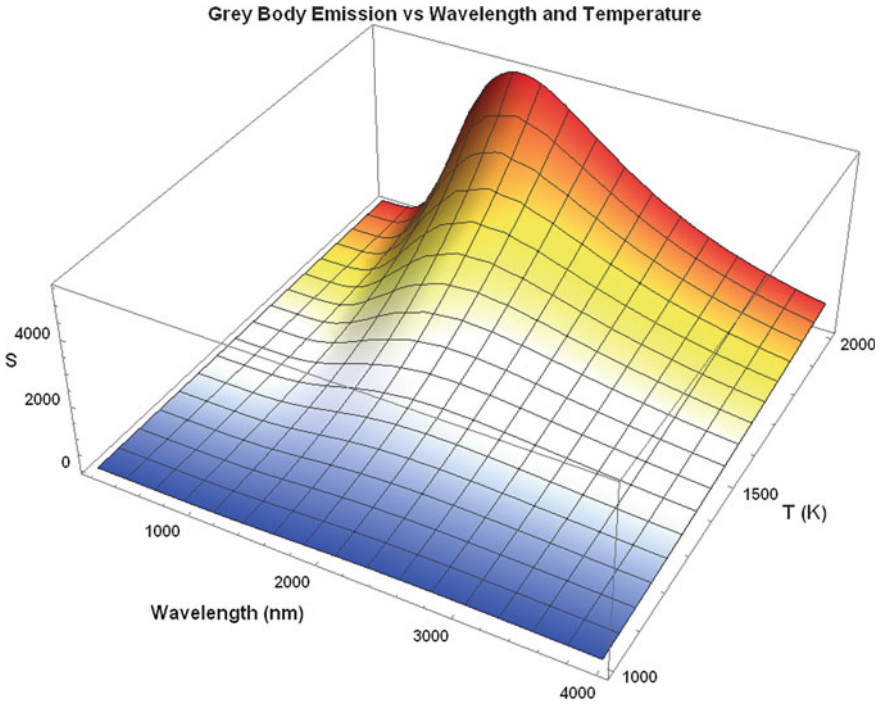
Fig. 3.58 Shown is the black body emission S (J/m^3-nm) as a function of wavelength and temperature

$$S_\lambda = \frac{8\pi hc}{\lambda^5}\frac{1}{\exp\left(\frac{hc}{\lambda k_B T}\right) - 1}$$ (3.101)

where S_λ is in J m^{-3} nm^{-1}, h is Planck's constant (6.62607 $\times$ 10^{-34} m^2 kg s^{-1}), c is the speed of light (2.99799979 $\times$ 10^8 ms^{-1}), k$_B$ is Boltzmann's constant (1.38 $\times$ 10^{-23} m^2 kg s^{-2} K^{-1}), λ is wavelength in meters, and T is temperature of the black body in Kelvin.

Wein's displacement law predicts the peak wavelength of a black body at any temperature and shown in Table 3.19.

$$\lambda_{peak} = \frac{b}{T}$$ (3.102)

where b = 2.9 $\times$ 10^6 nm K.

Thermophotovoltaic materials should match up with the grey body spectrum generated by the emitter. A diagram of a thermophotovoltaic cell is shown in Fig. 3.59.

Table 3.19 Peak wavelength at various black body temperatures

T (K)	λ peak (nm)	hν (eV)
1000	2900.00	0.43
1200	2416.67	0.51
1400	2071.43	0.60
1600	1812.50	0.69
1800	1611.11	0.77
2000	1450.00	0.86
2200	1318.18	0.94
2400	1208.33	1.03
2600	1115.38	1.12
2800	1035.71	1.20
3000	966.67	1.29
3200	906.25	1.37
3400	852.94	1.46
3600	805.56	1.54
3800	763.16	1.63
4000	725.00	1.72
4200	690.48	1.80
4400	659.09	1.89
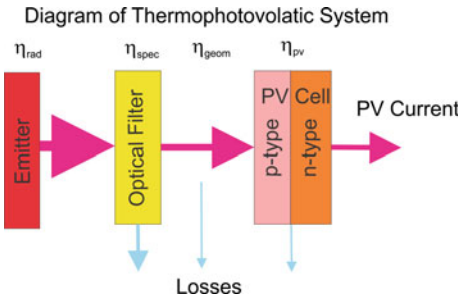
Fig. 3.59 Diagram of a thermophotovoltaic system. The emitter gives off grey body radiation with an efficiency (η_{rad}). The radiation then passes through an optical filter and the fraction of photons which can be absorbed by the photovoltaic cell has a spectral efficiency (η_{spec}). Emitted radiation expands and a portion will reach the photovoltaic. This is described by the geometrical factor (η_{geom}). Once absorbed in the photovoltaic cell, the photons are converted into an electrical current described by the photovoltaic efficiency (η_{pv})

The thermophotovoltaic generator system efficiency is (η_{system}),

$$\eta_{system} = \eta_{rad}\eta_{spec}\eta_{geom}\eta_{pv} \qquad (3.103)$$

Typical matchups between low band-gap materials (binary, ternary, or quaternary semiconductors) and emitter temperature are shown in Table 3.20.

Table 3.20 Thermophotovoltaic material properties and probable emitter operating temperature [79]

Material	Band-Gap Eg (eV)	Typical operating band-gap energy (eV)	Probable operating grey body temperature (K)
InP	1.344	1.344	3100
InGaAsSb	0.5–0.6	0.55	1300
InGaAs	0.4–1.4	0.55	1300
InPAsSb	0.3–0.55 eV	0.5	1200
Ge	0.66	0.66	1500
GaSb	0.72	0.72	1899

Thermophotovoltaic systems have promise. Theoretically, efficiencies of 30+ % have been predicted [83]. Practically, the system efficiencies range from about 0.04–24 % [80].

3.3 Summary

Ionizing radiation interacts with matter by creating ionization and excitation of the atoms and/or molecules that make up the material. In an energy conversion system which depends on the production of ions, there will be a reduction of efficiency due to the capability of producing ions (35–50 %) based on the transducer material properties. For systems which depend on heat, the ionization and excitation will eventually be converted to heat.

The energy conversion devices which are ion based include alphavoltaics, betavoltaics, Schottky barrier, direct charge collection and indirect systems such as PIDEC. A few heat based direct energy conversion systems were also discussed including the RTG, thermionics and thermophotovoltaics.

Problems

1. An electron is emitted from the source plate of a DCNB at angle $\theta = 30°$. Assuming this angle exceeds θ_m, what percent of the particle's initial kinetic energy will reach the collector? If the minimum angle of emission was determined to be 25°, what was the ideal efficiency of the parallel plate DCNB?
2. Suppose the distance between the source and the collector is 1.5 cm. A beta particle from Sr-90 is emitted off the surface of the source at the minimum angle of emission of 60°. What is the electric field strength between the source and collector? Calculate using the average energy determined by the 1/3 βmax rule as well as the full spectrum.
3. An RTG utilizing the Seebeck effect is placed in an environment resulting in a temperature gradient of 700 K between the radioisotope heat source and the heat sink. If material A has a Seebeck coefficient of 7.5 μV/K and material B has a Seebeck coefficient of −15 μV/K, what is the voltage produced?

4. Discuss the maximum efficiency limitations of ion pair based transducers.
5. Discuss the efficiency limitations of alphavoltaic cells.
6. Discuss the efficiency limitations of betavoltaic cells.
7. Discuss the efficiency limitations of Schottky barrier based nuclear batteries.
8. Discuss the efficiency limitations of direct charge collection nuclear batteries.
9. Discuss the efficiency limitations of a direct charge collection nuclear battery that works on charge build up and discharge cycles.
10. Design a 1 W electric indirect nuclear battery based on Kr-85. What is the dose rate to personnel for an unshielded nuclear battery with your design?
11. Discuss the efficiency limitations for an indirect nuclear battery using solid-state isotopes?
12. Discuss the best wide band-gap semiconductors that can be used as photo-voltaic cells for excimer fluorescence conversion.
13. What is the spectral matching efficiency for SiC, GaN, diamond and AlN with a xenon excimer fluorescence source?
14. Are phosphor emitters more efficient than excimer emitters? Explain your answer.
15. Explain the Seebeck effect and how it works.
16. Explain how thermionic systems work.
17. What are the strengths and the weaknesses of thermophotovoltaics?

References

1. Smith A, Fields P, Roberts J (1957) Spontaneous fission neutron spectrum of Cf252. Phys Rev 108:411–413
2. Nicodemus DB, Staub HH (1953) Fission neutron spectrum of U^{235}. Phys Rev 89:1288–1290
3. Zeynalov S, Hambsch F-J, Obertstedt S (2011) Neutron emission in fission of ^252Cf(SF). J Korean Phys Soc 59:1396
4. DOE-HDBK-1019/1–93 (1993) Nuclear physics and reactor theory. Department of Energy, Washington, DC
5. Turner JE, Kelsey KA (1995) Atoms, radiation, and radiation protection. Wiley, New York
6. Ziegler JF, Ziegler MD, Biersack JP (2010) SRIM–The stopping and range of ions in matter (2010). Nucl Instrum Methods Phys Res, Sect B 268:1818–1823
7. Prelas MA, Weaver CL, Watermann ML, Lukosi ED, Schott RJ, Wisniewski DA (2014) A review of nuclear batteries. Prog Nucl Energ 75:117–148
8. Oh K, Prelas MA, Rothenberger JB, Lukosi ED, Jeong J, Montenegro DE et al (2012) Theoretical maximum efficiencies of optimized slab and spherical betavoltaic systems utilizing Sulfur-35, Strontium-90, and Yttrium-90. Nucl Technol 179:9
9. Prelas M, Charlson E, Charlson E, Meese J, Popovici G, Stacy T (1993) Diamond photovoltaic energy conversion. In: Yoshikawa M, Murakawa M, Tzeng Y, Yarbrough WA (eds) Second international conference on the application of diamond films and related materials. MY Tokyo, pp 5–12
10. Prelas M, Popovici G, Khasawinah S, Sung J (1995) Wide band-gap photovoltaics. In: Wide band gap electronic materials. Springer, pp 463–474
11. Prelas MA, Hora HP (1994) Radioactivity-free efficient nuclear battery. Germany Patent

12. Radprocalculator (2015) Gamma emitter point source dose-rate with shielding. http://www.radprocalculator.com/Gamma.aspx

13. Guyot J, Miley G, Verdeyen J (1972) Application of a two-region heavy charged particle model to Noble-gas plasmas induced by nuclear radiations. Nucl Sci Eng 48:373–386

14. Giuliani JL, Petrov GM, Dasgupta A (2002) Electron energy deposition in an electron-beam pumped KrF amplifier: Impact of the gas composition. J Appl Phys 92:1200–1206

15. Bernard S, Slaback Jr Lester A, Kent BB (1998) Handbook of health physics and radiological health. Williams & Wilkins, Baltimore

16. Oh K (2011) Modeling and maximum theoretical efficiencies of linearly graded alphavoltaic and betavoltaltaic cells. M.Sc., Nuclear Science and Engineering Institute, University of Missouri, University of Missouri, Columbia

17. Rappaport P (1956) Radioactive battery employing intrinsic semiconductor. USA Patent 2,745,973, 1956

18. Anno JN (1962) A direct-energy conversion device using alpha particles. Nucl News 6

19. Oh K, Prelas MA, Lukosi ED, Rothenberger JB, Schott RJ, Weaver CL et al (2012) The theoretical maximum efficiency for a linearly graded alphavoltaic nuclear battery. Nucl Technol 179:7

20. Schott RJ (2012) Photon intermediate direct energy conversion using a Sr-90 beta source. Nuclear Science and Engineering Institute, University of Missouri, PhD

21. Eckerman KF, Westfall RJ, Ryman JC, Cristy M (1994) Availability of nuclear decay data in electronic form, including beta spectra not previously published. Health Phys 67:338–345

22. Wrbanek JD, Wrbanek SY, Fralick GC, Chen L-Y (2007) Micro-fabricated solid-state radiation detectors for active personal dosimetry. NASA/TM 214674

23. Ravankar ST, Adams TE (2014) Advances in betavoltaic power sources. J. Energy Power Sources 1:321–329

24. Popovici G, Melnikov A, Varichenko VV, Sung T, Prelas MA, Wilson RG et al (1997) Diamond ultraviolet photovoltaic cell obtained by lithium and boron doping. J Appl Phys 81:2429

25. Doolittle WA, Rohatgi A, Ahrenkiel R, Levi D, Augustine G, Hopkins RH (1997) Understanding the role of defects in limiting the minority carrier lifetime in sic. MRS Online Proc Lib 483:null–null

26. Seely JF, Kjornrattanawanich B, Holland GE, Korde R (2005) Response of a SiC photodiode to extreme ultraviolet through visible radiation. Opt Lett 30:3120–3122

27. Neamen DA (2003) Semiconductor physics and devices. McGraw Hill

28. Savtchouk A, Oborina E, Hoff A, Lagowski J (2004) Non-contact doping profiling in epitaxial SiC. Mater Sci Forum 755–758

29. Huang M, Goldsman N, Chang C-H, Mayergoyz I, McGarrity JM, Woolard D (1998) Determining 4H silicon carbide electronic properties through combined use of device simulation and metal–semiconductor field-effect-transistor terminal characteristics. J Appl Phys 84:2065–2070

30. Sze SM, Ng KK (2006) Physics of semiconductor devices. Wiley

31. Latreche A, Ouennoughi Z (2013) Modified Airy function method modelling of tunnelling current for Schottky barrier diodes on silicon carbide. Semicond Sci Technol 28:105003

32. Östlund L (2011) Fabrication and characterization of micro and nano scale SiC UV photodetectors. Student Thesis, Masters of Science, Royal_Institute_of_Technology. Stockholm, p 74

33. Eiting CJ, Krishnamoorthy V, Rodgers S, George T, Robertson JD, Brockman J (2006) Demonstration of a radiation resistant, high efficiency SiC betavoltaic. Appl Phys Lett 88:064101-064101-3

34. Tsang FY-H, Juergens TD, Harker YD, Kwok KS, Newman N, Ploger SA (2012) Nuclear voltaic cell. Google Patents

35. Wacharasindhu T, Jae Wan K, Meier DE, Robertson JD (2009) Liquid-semiconductor-based micro power source using radioisotope energy conversion. In: Solid-state sensors, actuators and microsystems conference, 2009. TRANSDUCERS 2009. International, pp 656–659

36. Patel JU, Fleurial J-P, Snyder GJ (2006) Alpha-voltaic sources using liquid ga as conversion medium. NASA: NASA Tech Briefs
37. Miley GH (1970) Direct conversion of nuclear radiation energy. American Nuclear Society
38. Galina Yakubova AK (2012) Nuclear Batteries with tritium and promethium-147 radioactive sources: design, efficiency, application of tritium and pm-147 direct charge batteries, tritium battery with solid dielectric. LAP Lambert Academic Publish*ng*
39. Mulcahy MJ, Bolin PC (1971) In: Agency ARP (ed) High voltage breakdown study: handbook of vacuum insulation. National Technical Information Services, Springfield, VA, p 78
40. Prelas MA, Boody FP, Miley GH, Kunze JF (1988) Nuclear driven flashlamps. Laser Part Beams 6:25–62
41. Prelas MA (1985) Excimer Research using nuclear-pumping facilities. National Science Foundation: NSF, p 1–131
42. Lecours MJ, Prelas MA, Gunn S, Edwards C, Schlapper G (1982) Design, construction, and testing of a nuclear-pumping facility at the University of Missouri Research Reactor. Rev Sci Instrum 53:952–959
43. Chung AK, Prelas MA (1987) Sensitivity analysis of Xe₂* excimer fluorescence generated from charged particle excitation. Laser Part Beams 5:125–132
44. Klein MB (1974) In: Laboratories HR (ed) Waveguide gas lasers. NTIS
45. Prelas MA (1981) A potential UV fusion light bulb for energy conversion. In: Presented at the 23rd annual meeting division of plasma physics American physical society, New York, NY, 1981
46. Prelas MA, Loyalka SK (1981) A review of the utilization of energetic ions for the production of excited atomic and molecular states and chemical synthesis. Prog Nucl Energy 8:35–52
47. Prelas MA (1981) In: Missouri U (ed) Notorized notes dust core reactor and laser. p 7
48. Boody EP, Prelas MA, Miley GH (1977) Nuclear generated excimer radiation for pumping lasers. University of Illinois, Nuclear Engineering Department
49. Prelas MA, Boody FP, Zediker M (1984) A direct energy conversion technique based on an aerosol core reactor concept. In: IEEE International conference on plasma science, p 8
50. Melnikov SP, Sizov AN, Sinyanskii AA, Miley GH (2015) Lasers with nuclear pumping. Springer, New York, NY
51. Chung A, Prelas M (1984) Charged particle spectra from U-235 and B-10 micropellets and slab coatings. Laser Part Beams 2:201–211
52. Prelas M, Boody F, Zediker M (1984) A direct energy conversion technique based on an aerosol core reactor concept. IEEE Publication, p 8
53. Prelas MA, Boody FP, Zediker MS (1985) An aerosol core nuclear reactor for space-based high energy/power nuclear-pumped lasers. In: El-Genk MS, Hoover M (eds) Space nuclear power systems. Orbit Book Company
54. Mencin DJ, Prelas MA (1992) Gaseous like Uranium reactors at low temperatures using C60 cages. In: Proceedings of nuclear technologies for space exploration. American Nuclear Society, Aug 1992
55. Guoxiang G, Prelas MA, Kunze JF (1986) Studies of an aerosol core reactor/laser's critical properties. In: Hora H, Miley GH (eds) Laser interaction and related plasma phenomena. Springer, pp 603–611
56. Walters RA, Cox JD, Schneider RT (1980) Trans Am Nucl Soc 34:810
57. Prelas M, Charlson E (1989) Synergism in inertial confinement fusion: a total direct energy conversion package. Lasers Part Beams 7:449–466
58. Prelas M, Charlson E, Boody F, Miley G (1990) Advanced nuclear energy conversion using a two step photon intermediate technique. Prog Nucl Energy 23:223–240
59. Lee MYJJ, Simones MMP, Kennedy JC, Us H, Makarewicz MPF, Neher DJA et al (2014) Thorium fuel cycle for a molten salt reactor: state of Missouri feasibility study. ASEE annual conference. Indianappolis, IN, p 28
60. Schott RJ, Weaver CL, Prelas MA, Oh K, Rothenberger JB, Tompson RV et al (2013) Photon intermediate direct energy conversion using a 90Sr beta source. Nucl Technol 181:5

61. Weaver CL (2012) PIDECα: photon intermediate direct energy conversion using the alpha emitter polonium-210. PhD Nuclear Science and Engineering Institute, University of Missouri. http://hdl.handle.net/10355/15908

62. Ahlswede J, Hebel S, Kalinowski MB, Roß JO, Update of the global krypton-85 emission inventory. Carl-Friedrich-von-Weizsäcker-Zentrum für Naturwissenschaft und Friedensforschung der Universität Hamburg

63. Steinfelds E, Tulenko J (2011) Isotopes and radiation: general-evaluation and verification of durability and efficiency of components of photon assisted radioisotopic batteries. Trans Am Nucl Soc 104:201

64. Steinfelds EV, Tulenko JS (2011) Development and testing of a nanotech nuclear battery for powering MEMS devices. Nucl Technol 174:119–123

65. Steinfelds E, Tulenko JS (2009) Designs and performance assessments of photon assisted radioisotopic energy sources. Trans Am Nucl Soc 100:672–674

66. Steinfelds E, Prelas M (2007) More sources and review of design for radioisotope energy conversion systems. Trans Am Nucl Soc 96:811–812

67. Bower KE, Barbanel YA, Shreter YG, Bohnert GW (2002) Polymers, phosphors, and voltaics for radioisotope microbatteries. CRC Press

68. Prelas MA, Sved J, Dann A, Jennings HJ, Mountford A (1999) Solid state electric generator using radionuclide-induced exciton production, WO 1999036967 A1

69. Shan W, III JWA, Yu KM, Walukiewicz W, Haller E, Martin MC et al (1999) Dependence of the fundamental band gap of $Al_xGa_{1-x}N$ on alloy composition and pressure. J Appl Phys 85:8505–8507

70. Prelas MA (2016) Nuclear-pumped lasers: Springer International Publishing

71. Shonoya S, Yen WM (1999) Phosphor handbook. CRC Press, Boca Raton, FL

72. Xu Z-H, Tang X-B, Hong L, Liu Y-P, Chen D (2015) Structural effects of ZnS:Cu phosphor layers on beta radioluminescence nuclear battery. J Radioanal Nucl Chem 303:2313–2320

73. Hong L, Tang X-B, Xu Z-H, Liu Y-P, Chen D (2014) Parameter optimization and experiment verification for a beta radioluminescence nuclear battery. J Radioanal Nucl Chem 302: 701–707

74. Prelas MA (2013) Micro-scale power source, United States Patent 8552616, USA Patent

75. Angrist SW (1982) Direct energy conversion, 4th edn. Allyn and Bacon Inc, Boston

76. Nochetto H, Maddux JR, Taylor P (2013) High temperature thermoelectric materials for waste heat regeneration. Army Research Laboratory, Adelphi, MD, pp 20783–1197

77. NASA (2016) Radioisotope power systems. https://solarsystem.nasa.gov/rps/rtg.cfm

78. Ferrari C, Melino F (2014) Thermo—Photo—Voltaic generator development. Energy Procedia 45:150–159

79. Ferrari C, Melino F, Pinelli M, Spina PR (2014) Thermophotovoltaic energy conversion: Analytical aspects, prototypes and experiences. Appl Energy 113:1717–1730

80. Ferrari C, Melino F, Pinelli M, Spina PR, Venturini M (2014) Overview and status of thermophotovoltaic systems. Energy Procedia 45:160–169

81. Nam Y, Yeng XY, Lenert P, Bermel P, Celanovic I, Soljačić M et al (2014) Solar thermophotovoltaic energy conversion systems with two-dimensional tantalum photonic crystal absorbers and emitters. Sol Energy Mater Sol Cells 122:287–296

82. Bitnar B, Durisch W, Holzner R (2013) Thermophotovoltaics on the move to applications. Appl Energy 105:430–438

83. Teofilo VL, Choong P, Chang J, Tseng YL, Ermer S (2008) Thermophotovoltaic energy conversion for space. J Phys Chem C 112:7841–7845

84. Nelson RE (2003) A brief history of thermophotovoltaic development. Semicond Sci Technol 18:S141–S143

85. Robert EN (2003) A brief history of thermophotovoltaic development. Semicond Sci Technol 18:S141